_____

Design of self-nanostructured thin films for antibacterial applications

_____

DISSERTATION

zur Erlangung des Grades

des Doktors der Ingenieurwissenschaften

der Naturwissenschaftlich-Technischen Fakultät

der Universität des Saarlandes

UNIVERSITÄT DES SAARLANDES

Von

Quentin LIEBGOTT

Saarbrücken / Nancy - 2023

Tag des Kolloquiums: 26. Oktober 2023

Dekan: Prof. Dr. Ludger Santen

Berichterstatter: Prof. Dr.-Ing. Frank Mücklich
     Prof. Dr. Karen Lienkamp
     Prof. Dr.-Ing. David Horwat

Weitere Mitglieder: Dr. Raúl Gago
     Prof. Dr. Nicolas Martin
     Dr. Stéphanie Bruyere

Vorsitz: Dr. Mireille Richard-Plouet

Abstract

In this thesis, magnetron sputtering is used to sputter thin films at a chemical composition that is intermediate to those of pure amorphous and crystalline thin films. For some metallic alloys, especially Zr-X alloys (X = Cr, V, Mo, W) that will be studied in this work, this results in a competitive growth between the amorphous and crystalline phases. The crystalline regions have a peculiar geometry that allows tailoring the surface morphology of the film and thus its surface-related properties. We show that the deposition conditions (deposition pressure, deposition rate) have a significant impact on the films morphology. In particular, the deposition rate affects the nucleation and growth kinetics inside the crystalline regions, and varying the deposition pressure allows synthesizing films with novel microstructures. We then show that when coated with a thin copper layer, thin films deposited at a high pressure show a great potential as antibacterial surfaces, being more bactericidal than metallic copper, against Gram-negative bacteria as well as against Gram-positive bacteria. Finally, we focus on the close link that exists between the internal stress during film growth and the microstructure of these thin films, which allows us to gain precious insights on crystallization in these thin films.

Résumé

Dans cette thèse, nous utilisons la pulvérisation cathodique magnétron pour déposer des couches minces à une composition chimique intermédiaire aux compositions pour lesquelles la couche serait totalement amorphe ou totalement cristalline. Pour certains alliages métalliques, notamment les alliages Zr-X (X = Cr, V, Mo, W) qui sont étudiés dans cette thèse, cela résulte en une croissance compétitive entre les phases amorphe et cristalline. Les régions cristallines présentent une géométrie particulière qui permet de contrôler la morphologie de surface du film et donc ses propriétés de surface. Nous démontrons que les conditions de dépôt (pression, vitesse de dépôt) ont un impact significatif sur la morphologie des films synthétisés. En particulier, la vitesse de dépôt impacte les cinétiques de nucléation et de croissance au sein des régions cristallines, et une variation de pression permet l'obtention de films présentant de nouvelles microstructures. Nous démontrons ensuite que ces films, lorsque recouverts d'une fine couche de cuivre, présentent un intérêt pour des applications antibactériennes, étant plus bactéricides que du cuivre métallique, autant contre des bactéries Gram-négatives que Gram-positives. Finalement, nous nous concentrons sur le lien étroit qui existe entre les contraintes dans le film lors du dépôt et la microstructure des couches minces, nous permettant d'obtenir de précieuses informations sur la cristallisation dans ces films.

Zusammenfassung

In dieser Doktorarbeit wird Magnetronsputtern verwendet, um Dünnschichten mit einer chemischen Zusammensetzung zu sputtern, die zwischen den von rein amorphen und kristallinen Dünnschichten liegt. Bei einigen metallischen Legierungen, insbesondere Zr-X Legierungen (X = Cr, V, Mo, W), die in dieser Arbeit untersucht werden, führt dies zu einem wettbewerbsfähigen Wachstum zwischen amorphen und kristallinen Phasen. Die kristallinen Bereiche weisen eine besondere Geometrie auf, die es ermöglicht, die Oberflächenmorphologie des Films und damit seine oberflächenbezogenen Eigenschaften zu kontrollieren. Wir zeigen, dass die Abscheidebedingungen (Abscheidedruck, Abscheiderate) einen signifikanten Einfluss auf die Morphologie der Filme haben. Insbesondere beeinflusst die Abscheiderate die Keimbildungs- und Wachstumskinetik innerhalb der kristallinen Bereiche, und durch Variation des Abscheidedrucks lassen sich Filme mit neuen Mikrostrukturen herstellen. Anschließend zeigen wir, dass diese dünnen Filme, wenn sie mit einer dünnen Kupferschicht beschichtet werden, ein großes Potenzial als antibakterielle Oberflächen aufweisen und gegenüber gramnegativen und grampositiven Bakterien stärker bakterizid wirken als metallisches Kupfer. Schließlich konzentrieren wir uns auf die enge Verbindung zwischen den Mechanischen Spannungen im Film während der Ablagerung und der Mikrostruktur dieser dünnen Schichten, wodurch wir wertvolle Informationen über die Kristallisation in diesen Filmen gewinnen können.

Résumé détaillé

Lors du dépôt de certains alliages métalliques par pulvérisation cathodique magnétron, il est possible de contrôler les paramètres de dépôt afin d'obtenir des couches minces amorphes ou cristallines. En particulier, le choix de la composition est un paramètre majeur. Il a par exemple été rapporté que pour des films de Zr-Mo une transition d'amorphe à cristallin est observée à ~60 at.% Mo. Ainsi, lorsque le film est moins riche en molybdène, il tend à être amorphe, et il tend à être cristallin lorsque sa teneur en molybdène augmente au-delà de ce seuil. Ce comportement est semblable à certains autres alliages à base de zirconium, tels que Zr-W, Zr-Cr ou Zr-V. De plus, il a récemment été montré que déposer des couches minces de Zr-Mo ou de Zr-W à la composition de transition de phase amorphe-cristal permet l'élaboration de couches minces biphasées, comportant à la fois une phase amorphe et une phase cristalline. De façon intéressante, une croissance compétitive a lieu entre ces deux phases lors de la croissance du film ; le film est amorphe au début de la croissance puis, lorsqu'une épaisseur critique est atteinte, la nucléation de régions cristallines survient. Tandis que la matrice amorphe croît sous la forme de colonnes, les régions cristallines croissent sous la forme de cônes composés de nano-colonnes, avec un dôme sur leur surface. Cette géométrie particulière des régions cristallines permet un contrôle de la morphologie de surface du film et donc de ses propriétés de surface.

Outre les alliages à base zirconium, ce phénomène a été observé dans plusieurs systèmes par différentes techniques d'élaboration : Si:H, TiO_2, TiAl et $BaTiO_3$. Cependant, bien que ce phénomène ait été observé dans plusieurs systèmes, certaines interrogations subsistent. Il a été rapporté que son observation expérimentale pouvait être compliquée dû à sa dépendance à l'épaisseur, mais nous ne savons pas si ce phénomène peut être observé pour d'autres systèmes, ni ses conditions d'existence. Par ailleurs, il existe peu d'informations sur l'origine de la

nucléation de la phase cristalline après une certaine épaisseur critique, et les films à base de zirconium manquent d'applications potentielles pour confirmer leur utilité.

Cette thèse s'intéresse tant aux phénomènes qui surviennent pendant le dépôt, tels que la nucléation de la phase cristalline et les cinétiques de nucléation et de croissance des nano-colonnes qui la composent, qu'à la potentielle utilité de ces films en tant que surfaces antibactériennes.

Tout d'abord, nous montrons que la croissance compétitive observée pour Zr-Mo et Zr-W existe aussi pour les alliages Zr-Cr et Zr-V. Les nano-colonnes des régions cristallines de Zr-Cr sont similaires à celles observées pour Zr-Mo et Zr-W, tandis que pour Zr-V elles sont plus larges et facettées à leur surface. Les natures respectivement amorphe et cristalline des colonnes et des cônes ont été confirmées par diffraction électronique en microscopie électronique en transmission. Nous nous intéressons particulièrement aux changements de géométrie des régions cristallines en fonction de la vitesse de dépôt. Pour cela, des films de Zr-Cr ont été déposés avec des vitesses de dépôt variant entre 5 et 63 nm/min. La croissance compétitive a été observée dans toute la gamme de vitesses de dépôt étudiée, ce qui indique la résilience de ce phénomène lors de changement de paramètres de dépôt. De plus, la gamme de composition dans laquelle survient la croissance compétitive ne semble pas diminuer lorsque la vitesse de dépôt augmente. En revanche, à mesure que la vitesse de dépôt augmente, l'angle des cônes cristallins diminue, passant de 32° à 21°. Nous proposons que l'angle des cônes dépend du diamètre et de la densité de nucléation des nano-colonnes dans les cônes. En effet, lorsque la vitesse de dépôt augmente de 5 à 30 nm/min, le diamètre des nano-colonnes diminue tandis que le nombre de cristallites par cône est constant ; lorsque la vitesse de dépôt dépasse ce seuil, la densité de nucléation est saturée, mais le diamètre des nano-colonnes reste constant.

Les résultats obtenues pour l'alliage Zr-Cr sont ensuite comparés avec ceux obtenus pour les alliages Zr-V, Zr-Mo et Zr-W pour essayer de comprendre l'origine des différences de

morphologie entre ces alliages. Un modèle basé sur la diffusion est présenté, mais ne suffit pas à expliquer les différences de morphologie des phases cristallines entre les alliages. Nous proposons donc que la diffusion n'est pas le paramètre déterminant la croissance latérale des nano-colonnes, mais plutôt leur densité de nucléation. Les nano-colonnes étant en compétition avec leurs voisines, leur croissance latérale serait limitée et leur diamètre serait essentiellement dépendant de la densité de nucléation des colonnes. De plus, l'angle des cônes étant constant avec l'épaisseur, aucune transformation amorphe-cristalline ne se produit en périphérie des zones cristallines, les nano-colonnes sont donc aussi restreintes par la matrice amorphe entourant les cônes.

Comme évoqué précédemment, nous souhaitons également démontrer le potentiel applicatif de ces films. Pour ce faire, nous avons étudié l'efficacité antibactérienne de films de Zr-V contre deux bactéries : Escherichia Coli, représentante des bactéries Gram-négatives, et Bacillus Subtilis, représentante des bactéries Gram-positives. Deux études ont été menées, l'une sur ces films de Zr-V, l'autre sur des films de Zr-V recouverts d'une fine couche de cuivre. Il a en effet été démontré que, grâce au relargage d'ions cuivre, les surfaces de cuivre avaient un caractère bactéricide, et recouvrir les films d'une couche de cuivre est susceptible de leur conférer cette propriété. Deux hypothèses ont motivé le choix des films de Zr-V plutôt qu'un autre alliage pour cette étude : les dômes au-dessus des cônes cristallins sont plus grands que pour les autres systèmes, et leur surface est couverte de tétraèdres qui génèrent un relief plus prononcé que pour les autres morphologies. De plus grand dômes en surface résultent en une plus grande surface exposée, ce qui permettrait de relâcher plus d'ions cuivre lors de l'exposition aux bactéries et donc d'obtenir une meilleur efficacité antibactérienne. Les tétraèdres en surface des dômes de Zr-V ressemblant à des surfaces pouvant rompre les cellules bactériennes, il était envisagé d'observer un effet bactéricide physique additionnel à l'effet chimique du cuivre, augmentant l'efficacité antibactérienne des films.

Pour les films de Zr-V sans cuivre, il est montré que leur efficacité antibactérienne est limitée, bien qu'ils pourraient provoquer la rupture mécanique des cellules bactériennes. Lorsque recouverts de cuivre, ces films sont bien plus efficaces qu'un coupon de cuivre pour réduire le nombre de bactérie E. Coli à leur surface. Contre B. Subtilis, l'efficacité antibactérienne de ces films n'est pas significativement meilleure que le cuivre métallique. Bien que la surface de cuivre exposée soit supérieure pour nos échantillons en comparaison à une surface de cuivre plane, il n'y a pas de corrélation entre la surface exposée et l'efficacité antibactérienne. Nous faisons le lien entre l'efficacité antibactérienne des films, leur morphologie de surface, leur capacité à relâcher des ions cuivre ainsi que l'adhésion des bactéries sur les surfaces.

Ensuite, nous cherchons à éclaircir le lien qui existe entre les contraintes internes mesurées in-situ lors de la croissance des films et leur microstructure, afin de mieux comprendre la cristallisation dans ces films. Une étude avait déjà été menée sur des films biphasés de Zr-Mo et Zr-W, mais les mesures de contraintes étaient réalisées ex-situ, après le dépôt. En mesurant les contraintes in-situ, pendant la croissance de films de Zr-Mo et Zr-V, les résultats obtenus divergent. Ainsi, nous proposons que cette différence provient de plusieurs phénomènes : la relaxation des contraintes après dépôt, l'oxydation des films après exposition à l'air, qui remplit une partie de vides des films ou encore l'adsorption d'humidité après dépôt. En reprenant les même conditions de croissance et en mesurant les contraintes in-situ, le phénomène de croissance compétitive était totalement masqué, la contrainte interne ne donnant aucune indication sur la dynamique de croissance. Pour dépasser ce problème, nous avons déposé des films de Zr-V à une pression inférieure, ce qui a permis l'observation d'une nouvelle microstructure pour ces films : le film est totalement amorphe au début de la croissance, puis au-delà d'une épaisseur critique survient la nucléation de nano-colonnes cristallines allongées qui se propagent latéralement. La géométrie des phases cristallines est nouvelle, et est

potentiellement accompagnée d'une cristallisation de la phase amorphe déjà déposée. Cette microstructure diffère de celle rapportée pour des films de Zr-Mo déposés à basse pression.

En observant la contrainte interne lors des dépôts, il est observé que les phases amorphe et cristalline ont des dynamiques de croissance différentes, générant respectivement des contraintes de compression et de tension lors de leur croissance. Pour un film présentant la croissance compétitive, on observe une contrainte compressive en début de dépôt, puis une composante de tension apparaît lors de la croissance de la phase cristalline. Ces observations sont corrélées avec des cartographies d'orientation ainsi que des analyses de microscopie électronique en transmission, nous permettant de proposer un modèle de croissance expliquant la microstructure particulière de ces films ainsi que la cristallisation de la phase amorphe.

Enfin, nous parcourons les origines potentielles de l'énergie nécessaire à la cristallisation dans ces films biphasés à base zirconium : la température, la composition chimique et les contraintes. La température ne semble pas être à l'origine de la cristallisation, ne variant que très peu lors du dépôt et étant de 35 °C en moyenne lors du dépôt. De même, la composition des phases amorphe et cristalline n'est pas significativement différente, et la composition ne variant pas avec l'épaisseur dans ces films, il est peu probable qu'un changement local de composition chimique soit à l'origine de la cristallisation. En revanche, le changement de microstructure des films avec l'épaisseur correspond bien avec les changements de contrainte dans le film, ce qui en fait l'hypothèse la plus probable pour expliquer l'origine de la cristallisation dans ces films.

Ainsi, pour des films d'alliages à base zirconium, nous démontrons que les conditions de dépôt, et en particulier la pression et la vitesse de dépôt ont un impact significatif sur la morphologie des films synthétisés, permettant l'élaboration de films présentant un large éventail de morphologies de surface, et donc de propriétés de surface. De plus, nous explorons les cinétiques de nucléation et de croissance de la phase cristalline, ainsi que les potentielles

origines de sa nucléation. Lorsque recouverts d'une fine couche de cuivre, ces films ont un potentiel en tant que surfaces antibactériennes, étant plus efficaces que le cuivre métallique massif.

Acknowledgements

It goes without saying that I have to thank you, Corentin, Lucie and Dorra, for the moments spent together with a coffee, talking about anything, and for always being here when it counts. I am grateful to count you as my friends.

Now I would like to thank my brother and my parents. Their support and love helped me go through life, and I hope that I can show them my gratitude by obtaining the title of doctor.

These last words are dedicated to Juliette, who has shared my life for nearly 10 years now. My life is brighter since you are part of it. I look back at everything we already lived together, and hope that what lies ahead is as beautiful and exciting. Thank you for your continuous support through these years and for trusting me more than I trust myself. This thesis is dedicated to you. After all, you're my wonderwall.

Table of contents

4 Improvement of surface antibacterial properties : the cases of dual-phase Zr-V thin films and Cu-coated Zr-V thin films............ 101

5 Link between evolution of film internal stress during growth and the microstructure of dual-phase Zr-based thin films............... 123

Introduction

The topic of new functional materials has been the focus of intense research during the last decades [1–3]. Indeed, materials can exhibit a wide variety of interesting surface-related properties: corrosion or wear protection [4–6], or antibacterial surfaces [7–9] to name a few. Along with the development of new materials, new techniques emerged to synthesize materials. One of these techniques is magnetron sputtering that allows a relatively cheap synthesis of thin films at low temperatures. Owing to the high quenching rate accessible with this technique, some materials can be synthesized as amorphous or crystalline, depending on the deposition conditions.

It has been reported that Zr-based thin films could be synthesized as amorphous or crystalline, and that chemical composition was the dominating factor for the amorphous-crystalline transition [10–12]. Recently, it was reported that in the composition range of this transition, it is possible to observe a competitive growth of both the amorphous and crystalline phases, with the amorphous phase growing as columns and the crystalline phase nucleating above a critical thickness and growing as cones with a spherical cap on their surface [13–15]. This one-step bottom-up process allows a fine tailoring of the surface morphology, making the thin films readily usable for surface-related properties; we are interested in their antibacterial efficiency.

However, many important information on these films are still lacking. There is a need to explore this competitive growth an find new systems where it could occur, and that could help us understand the mechanisms behind this peculiar growth mode. Moreover, not much is known about the reason for the nucleation of the crystalline regions after a critical thickness is reached, and the Zr-based thin films lack practical application to confirm their usefulness in the real world. These are the points that we will try to address in this thesis.

In **Chapter 1**, a bibliographic review on dual-phase amorphous-crystalline competitive growth in thin films is presented, both for the Zr-based thin films used in this work, but also for other systems such as Si:H, TiAl, TiO_2 or $BaTiO_3$ for instance. Then follows a part concerning the bacterial cells, their structure and how materials can be used as antibacterial with a focus on the bactericidal effect of copper.

Chapter 2 is dedicated to the presentation of the elaboration and characterization techniques used for our thin films. These techniques help us address the main points of this work:

What are the kinetics of the growth of the crystalline phase, and can we relate the geometrical features of the crystalline phase with the growth kinetics and thermodynamics?

Why do the crystalline regions nucleate in the first place? Why does it only happen after a critical thickness has been deposited?

Finally, are these thin films really useful for their surface properties? Will they show a better antibacterial efficiency than a readily available copper coupon?

In **Chapter 3**, we will begin by searching the competitive growth in 2 new systems, namely Zr-Cr and Zr-V. Then, using Zr-Cr, the relation between the deposition conditions and the geometrical features of the crystalline regions will be addressed. Moreover, the results will also be explained with the growth kinetics during deposition as well as thermodynamics.

Then, in **Chapter 4**, we will test the usefulness of these thin films for antibacterial applications. For this, Zr-V thin films with different surface topographies will be tested, along with Cu-coated Zr-V thin films, against reference samples that are stainless steel and copper. Thus we will address their antibacterial efficiency, and explain the differences between the samples in regards to their surface topography, the release of copper ions from the surface and the bacterial adhesion on the surface. The film will be tested with E. Coli, a Gram-negative bacterium, and B. Subtilis, a Gram-positive bacterium.

Finally, **Chapter 5** dives into the link between the stress in the films during growth and the microstructure, to gain insights regarding the possible nucleation mechanisms of the crystalline regions during growth. We present the different possibilities to overcome the nucleation energy barrier that can lead to the crystalline phase nucleation. To do so, an in-situ stress monitoring during a Zr-V thin film has been performed and is compared with TEM micrographs, x-ray diffractograms and orientation cartography to link the microstructure of the film with the internal stress during growth and propose a growth model for these films.

Chapter 1

Background on sputtering and thin films growth, competitively grown amorphous-crystalline dual-phase thin films, their peculiar microstructures, and antibacterial properties of surfaces

ABSTRACT: In this chapter, we present the state of the art necessary for the understanding of the whole picture of this research. First, the physics underlying the sputtering process is presented, along with the growth modes of the thin films. Then, an overview of the systems in which the competitive growth has been reported to occur is given. The peculiar microstructure observed in these thin films are also addressed, in different systems, with a focus on the Si:H system and the Zr-based systems. Finally, we get into the antibacterial properties of surfaces, and the approach we are going to pursue in order to tackle the problem of bacterial contamination.

Contents

1.1 Magnetron sputtering and thin films growth

1.1.1 Sputtering principle

Sputtering falls into the physical vapor deposition (PVD) category. PVD describes a large variety of vacuum deposition techniques used to synthesize coatings on the surface of a substrate. Their similarity lies in the fact that they all use the physical generation of a vapor from a source material (the target), and this vapor then condensates on a substrate as a coating. Different PVD methods exist, the difference between these being the method used to generate

the vapor. PVD coatings exist for a wide range of materials, metals, ceramics, glass and polymer alike.

Sputtering is one of the most used and studied PVD methods, also widely applied in the industry. It will be used in this study to sputter thin films on substrates. This method takes place in a vacuum chamber with a rarefied atmosphere of an inert gas, usually Ar, in which a negative potential is applied to the source material, called target, while the walls of the chamber are connected to the ground. This polarization results in an electrical discharge between the target and the walls of the chamber, partially ionizing the gas and creating a plasma. As the target is negatively polarized, the positively charged ions in the plasma, usually Ar^+, are accelerated towards to target. When the ions collide with the surface, their momentum and potential energy (charge) is then used for different mechanisms, including the ejection of target atoms, that will eventually condensate on the substrate to form a thin film. Sputtering principle as well as the different mechanisms occurring from the momentum transfer and potential energy of the Ar^+ ions are shown in Fig. 1.1 (a, b). The ejection of target atoms is the sought mechanism, but the impact of the ion on the surface can also lead to the implantation of the neutralized ion, the reflection of the neutralized impinging ion, while the transfer of momentum and potential energy can lead to the emission of secondary electrons (see Fig. 1.1 (b)). Within the considered range of kinetic energies used for sputtering, secondary electrons are mostly originated from potential emission.
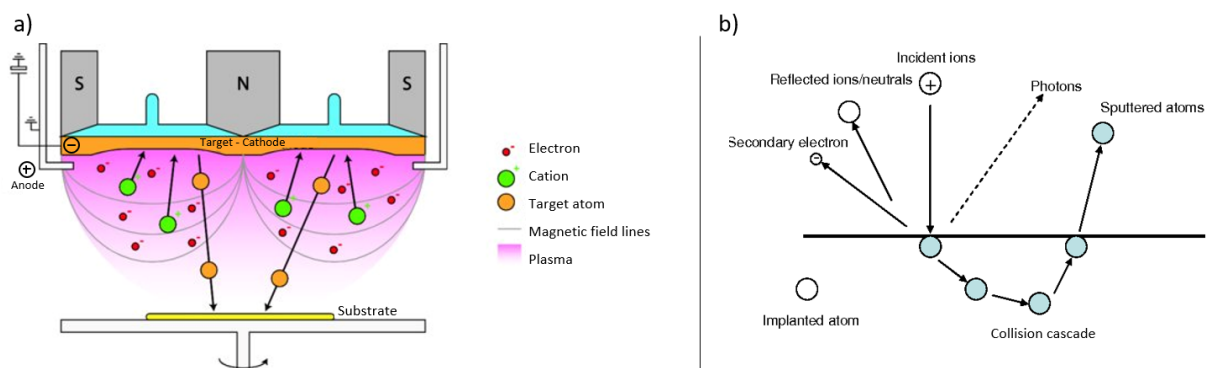
Fig. 1.1: Sputtering principle (a) [16], and the main mechanisms resulting from the collision of an Ar$^+$ atom on the target surface (b) [17].

Some conditions must be met in order for sputtering to be efficient. The ejected atoms must reach the surface of the substrate, meaning they must not be thermalized after colliding with too many gas atoms; the background gas pressure has to be low enough to avoid this. Also, the kinetic energy of the ions impinging the target has to overcome an energy threshold E_{th} in order to allow the ejection of target atoms, given by the following formula [18]:

$$\frac{E_{th}}{E_s} = \frac{(1+A)^2}{4A} \tag{1.1}$$

With E_s the surface binding energy of the target material, and A the ratio of target atom mass to projectile mass.

Both these prerequisites mean that a low pressure is required in sputtering, as it would prevent both the gas and target material atoms from colliding and losing kinetic energy.

Last but not least, one should account for the sputtering yield of the sputtered material Y, which is given by the Bohdansky equation [19]:

$$Y = Q s_n(\varepsilon)\left(1 - \left(\frac{E_{th}}{E_0}\right)^{2/3}\right)\left(1 - \frac{E_{th}}{E_0}\right)^2 \tag{1.2}$$

Where Q is a fit parameter, $s_n(\varepsilon)$ is the nuclear stopping power with the reduced energy ε, and E_0 is the projectile energy.

Each material has a different sputtering yield, i.e. a different number of ejected atoms per ion impinging the target. A different sputtering yield between materials will result in a different deposition rate with the same electrical parameters.

1.1.2 Magnetron sputtering

The aforementioned sputtering process suffers from one main drawback, which is a very low ionization of the background gas. Thus, fewer Ar^+ ions are generated, and the deposition rate is very low. To overcome this drawback, researchers have developed a process called magnetron sputtering. It differs by the addition of a magnetron device, a device consisting in two concentric magnets of opposed polarities that is placed behind the target to constrain the electron motion in the vicinity of the target. As shown in Fig. 1.2 (a), the magnets create magnetic lines that are parallel to the cathode surface and perpendicular to the electric field, which results in an increases in electron density close to the target. Thus, the probability of a gas atom colliding an electron and getting ionized increases, and so does the ion density in the plasma [20]. This makes for a denser plasma in the vicinity of the target, effectively increasing the ion bombardment on the target and therefore the deposition rate on the substrate.

Magnetrons exist in two subtypes: balanced and unbalanced magnetrons. They are schematically shown in Fig. 1.2 (b-d). The confinement of the magnetic lines differs between them; the magnetic lines are closed between the inner and outer poles in balanced magnetron, while some magnetic lines are directed towards the substrate in unbalanced magnetron type II, owing to the difference in relative magnet intensity. With unbalanced type II magnetron, electrons are also found in the vicinity of the substrate, ionizing the gas which then impacts the substrate surface and increasing the quality of the film. However, it also results in higher substrate heating and potential structural defects. Unbalanced type I magnetron also exists, but is not commonly used because of the low plasma density in the substrate region [21].
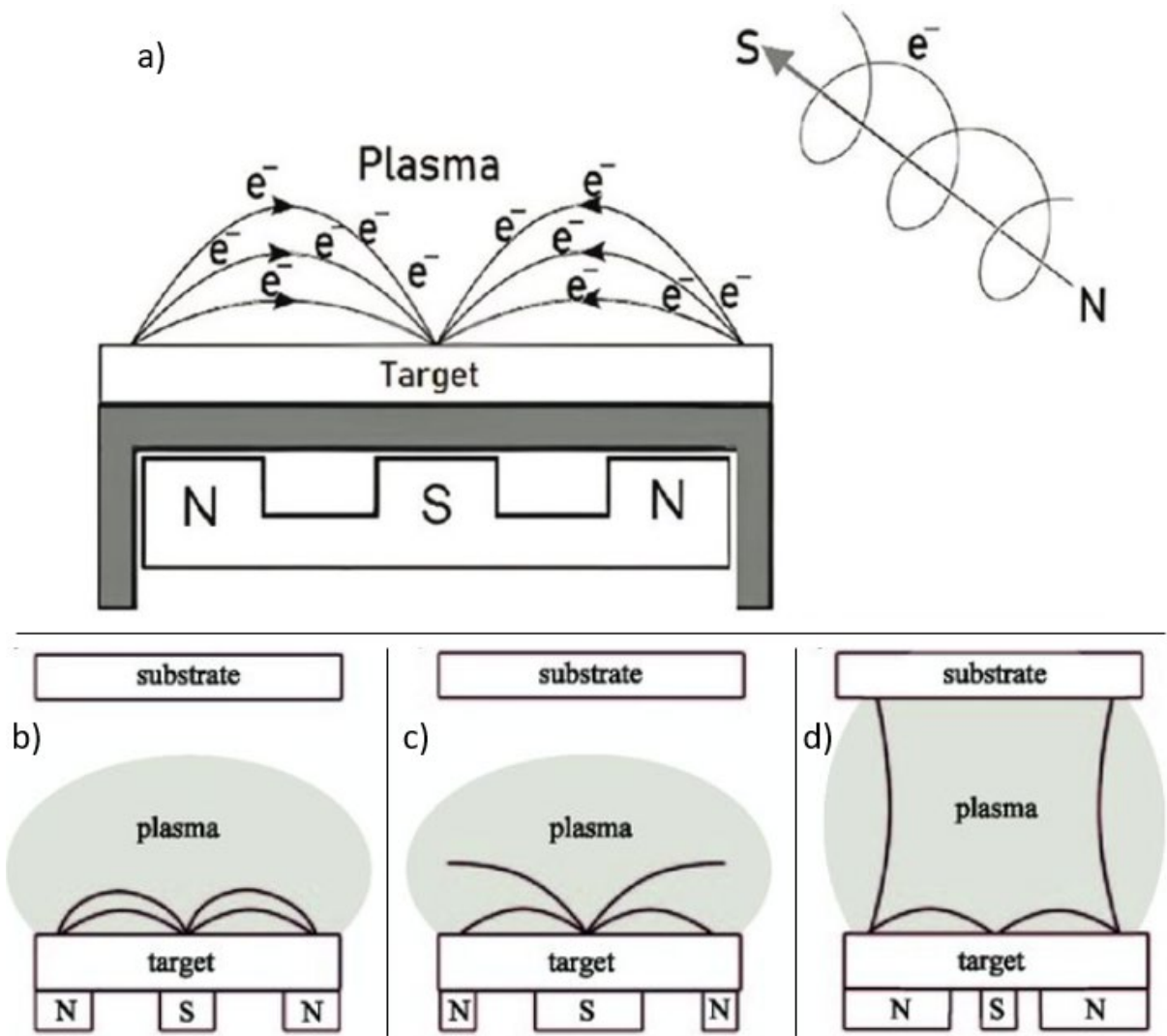
Fig. 1.2: Representation of the magnetic field near the target and the movement of the electrons around the magnetic lines (a), from Ref [20]. Schematic representations of a balanced magnetron (b), and unbalanced type I (c) and type II (d) magnetrons.

In this study, the magnetrons in the vacuum chamber were balanced.

1.1.3 Thin films growth modes

Schematically represented in Fig. 1.3 are the three basic growth modes of thin film growth. The growth mode for a thin film depends on the interaction strength between the adatoms and the surface of the substrate. In Volmer-Weber mode, the adatom-adatom

interactions are stronger than the adatom-surface interactions, leading to the growth of adatom clusters as 3D islands. This will cause rough films to grow on the substrate. The second growth mode is the Frank-van der Merwe mode, where adatoms bond preferentially with the surface, leading smooth films to grow. The third growth mode is the Stranski-Krastanov mode, which is intermediate to the two others, and the transition from the smooth layer-by-layer to a 3D island growth mode occurs at a critical thickness that is material-dependent.
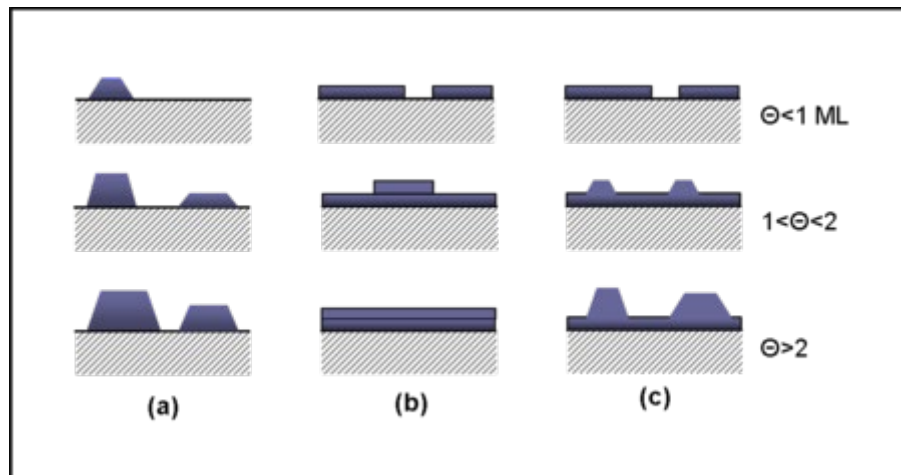
Fig. 1.3: Schematic representation of the 3 thin films growth modes, (a) Volmer-Weber mode, (b) Frank-van der Merwe mode and (c) Stranski-Krastanov mode.

1.1.4 Structure zone model

A structure zone model is a simplified way of illustrating the features of thin films on a diagram. They were first mentioned in 1969 by Movchan et al. [22] and were modified along with the new deposition techniques over time. These models aim to describe the film microstructure as a function of the deposition parameters. The first model in 1969 took into account the homologous temperature Th (which is the ratio between the deposition temperature and the target material melting temperature). Then Thorntorn extended it in 1974 to include the effect of the deposition pressure [23]. More recently, other versions of this model have been

proposed, as the one shown in Fig. 1.4 (a) from Mahieu et al. for instance, showing the effect of the adatom diffusion [24].

Anders proposed a new structure zone model, shown in Fig. 1.4 (b), that takes into account the effect of the ion flux in the growth of the film, by using the generalized temperature T* which is the sum of the homologous temperature and the effect of the potential energy of the atoms arriving at the substrate surface. Instead of the pressure, he used the normalized energy flux E* that accounts for the influence of kinetic energy of the particles. He also added the thickness of the film on a third axis to account for the densification and sputter etching [25].
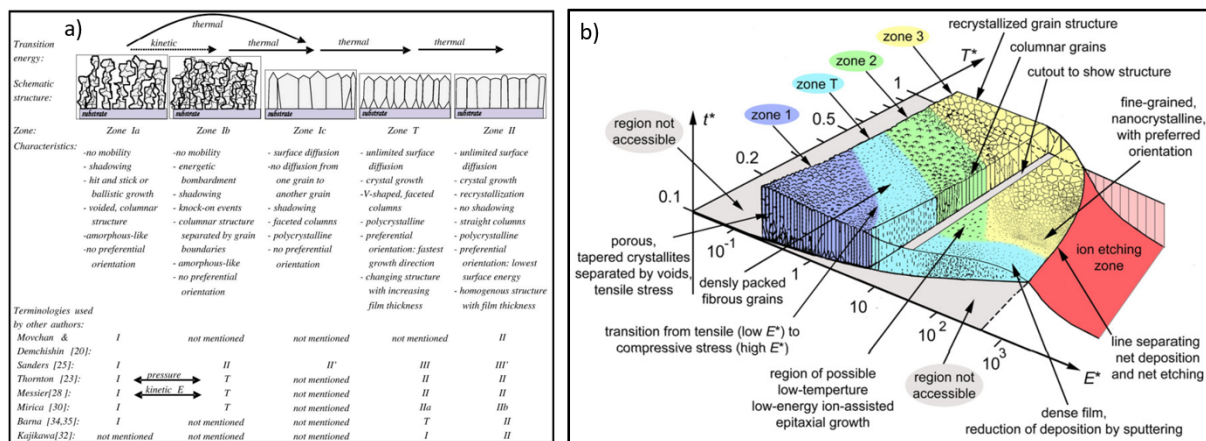
Fig. 1.4: Schematic representations of the structure zone models from Mahieu et al. (a) and Anders (b), respectively from Ref. [24] and Ref. [25]. T* is the generalized temperature, E* the normalized energy flux and t* the thickness of the film.

In zone 1, the adatom mobility is low leading to a constant nucleation of grains, and the final microstructure consists of fine and fibrous grains, and is highly porous. In zone T, surface diffusion is possible but diffusion between surfaces of adjacent growing grains is limited, which leads to competitive grain growth and an inhomogeneous microstructure throughout the film. Zone 2 is defined by a higher diffusion of the adatoms, leading to more uniform columnar grains. On the surface of the columns are found faceted surfaces. In zone 3, bulk diffusion becomes possible and the recrystallization of the film leads to large and dense grains.

1.2 Amorphous-crystalline competitive growth

This thesis focuses on amorphous-crystalline dual-phase thin films, resulting from a competitive growth between the amorphous and crystalline phases during growth, as well as their surface-related properties. This section presents the current knowledge on these peculiar thin films, from the conditions for the competitive growth to be observed experimentally to the currently thought crystalline phase nucleation mechanisms.

1.2.1 Si:H system

Historically, the first mention of the competitive growth between amorphous and crystalline phases during growth in the literature concerned the Si:H system and was reported by Koh et al. in 1998 [26]. More insights on this peculiar film growth were provided by Collins et al. in 2003 [27]. These films were grown with plasma-enhanced chemical vapor deposition (PECVD), which is a deposition process used to grow thin films from a gas state; for the deposition of Si:H thin films, a H_2/SiH_4 gas mixture is used.

Deposited thin films, qualified as protocrystalline, consist of two distinct phases, an amorphous phase that grows from the interface with the substrate onwards, and crystalline regions that grow as cones. However, the nucleation of the crystalline phase only occurs after a critical thickness has been reached, depending on the composition of the precursors gas mixture, as shown in Fig. 1.5 (a). This growth model consists in 3 zones: (a) an amorphous (a-Si:H) zone, (b) a so-called protocrystalline zone where both amorphous and microcrystalline (μc-Si:H) exist and grow competitively, and (c) a zone where only μc-Si:H grows.
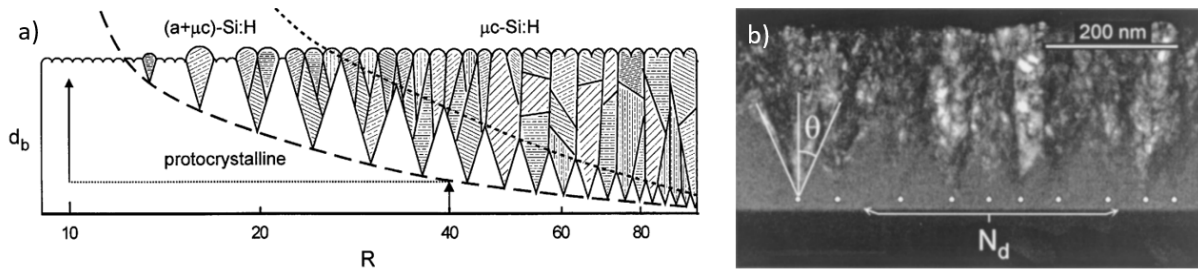
Fig 1.5: (a) Schematic representation of the microstructure of PECVD-grown Si-H thin films. The vertical axis represents the thickness of the film, while the horizontal axis represents the precursors gas mixture ratio: $R = [H_2]/[SiH_4]$. The dashed and dotted lines represent the $a \rightarrow (a+\mu c)$ and $(a+\mu c) \rightarrow \mu c$ transitions, respectively. (b) Cross-section TEM micrograph of a $(a+\mu c)$ Si:H thin film deposited at $R = 20$. From Ref. [27].

During this protocrystalline growth, the thin film initially grows as totally amorphous but when a critical thickness is reached, crystallites nucleate and grow along with the amorphous matrix. The thin film then grows as dual-phase amorphous and crystalline, until the crystalline phase overgrows the amorphous phase and remains the only one to continue growing.

To have a better control over the surface of the thin films, Collins et al proposed a phase diagram showing the surface state depending on the deposition conditions. It is shown in Fig. 1.6. It can be seen that the dual-phase $(a+\mu c)$ Si:H can be obtained from $R \approx 15$ up to $R = 40$.
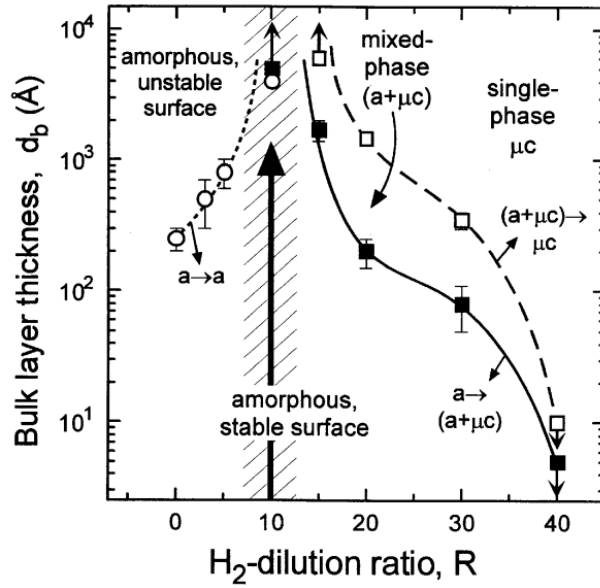
Fig 1.6: Phase diagram of the surface state of the Si:H thin film, depending on the thickness of the film and the gas mixture, from Ref. [27].

The interesting thing to note in these thin films is their peculiar structure; amorphous columns and conical crystalline regions grow simultaneously. According to the cone kinetics model, 3 conditions must be met for cone formation to occur: (1) the deposition must be isotropic, (2) the crystalline phase must nucleate on the surface of the growing film with a low nucleation density, and (3) this second phase must have a higher growth rate than the matrix [28,29]. These conditions force the phase with the higher growth rate to grow as cones with a spherical cap, which center is aligned with the cone apex. It has to be noted that, according to more recent studies, this third condition if true for the lateral growth rate but not for the vertical growth rate, as an increased lateral growth rate (relative to vertical growth rate) can lead to higher adatom diffusion towards the periphery of the nanocrystallites [14,30]. According to the authors, the a-Si:H phase grows faster than the μc-Si:H phase for low H dilution, meaning that if crystallites nucleate, they will be overgrown by the amorphous phase and eventually result in embedded crystallites. For high H dilution however, the μc-Si:H growth rate increases relatively to a-Si:H and nucleation will lead to conical growth of μc-Si:H [28].

The reason for the crystalline phase growth has been given, but the reason for the nucleation remains unhandled. Using a conventional furnace, the crystallization of an a-Si:H film requires temperatures as high as 600°C. The deposition of the thin film not making the substrate reach this temperature, another mechanism must govern for the crystalline phase nucleation during growth [31]. To this date, different nucleation mechanisms have been proposed. In this work the focus will partly be on the stress-induced nucleation mechanism, as it will be the focus on a following chapter in this thesis.

Amongst these nucleation mechanisms, it has been proposed that internal stress in the film could induce nucleation. Fujiwara et al. found that the intrinsic stress in the film increases with R and observed µc-Si:H nucleation only when the intrinsic stress exceeded 750 MPa, regardless of the deposition temperature [32]. When R is increased even more, the stress decreases due to the increase in volume fraction of the µc-Si:H phase, which could originate from the higher density of the µc-Si:H phase leading to stress relaxation in the film [32]. These results are presented in Fig. 1.7 (a).
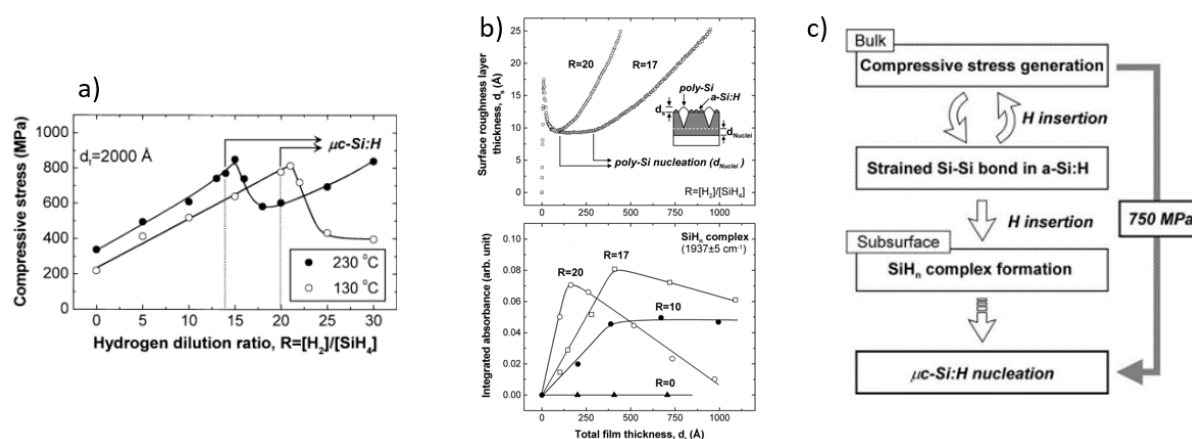
Fig 1.7: (a) Internal stress in films grown with different R at a 2000 Å thickness [32], (b) surface roughness and SiH_n complex integrated absorbance in function of total film thickness [33], and (c) proposed stress-induced nucleation mechanism [34].

To explain these results, a stress-induced nucleation mechanism has been proposed, and is shown in Fig. 1.7 (c) [32]. In this model, H atoms are inserted from the gas phase into the Si-Si bonds, straining them and generating compressive stress in the film. This continues occurring with increasing film thickness, leading to higher compressive stress and a higher number of strained Si-Si bonds. Then, following H insertion, Si-Si bonds are broken and SiH_n (n = 1, 2) complexes are formed. When the SiH_n complex density reaches a threshold, nucleation of the μc-Si:H phase happens (see Fig. 1.7 (b)). These complexes provide structural flexibility and enable an ordered $Si-SiH_3$ structure to be formed (SiH_3 being the film precursor). This acts as a pre-nucleation site on the surface [35].

Another nucleation mechanism is the surface diffusion model, in which the surface is fully covered by H atoms, and the hydrogen exchange reactions being highly exothermic, the surface locally heats. As a consequence, the SiH_3 molecules on the surface can diffuse to more favorable sites, leading to the formation of an ordered structure and epitaxial growth [36,37].

Currently, there is no consensus on the nucleation mechanism of the μc-Si:H phase from the amorphous matrix.

1.2.2 Zr-based systems

Even though they were not studied as thoroughly as the Si:H system, the Zr-based systems have only recently been first reported, in 2019, and induce a growing interest. In these systems, not only surface-related properties have been reported, but also insight on the nucleation and growth kinetics of the crystalline phase during film growth. Regarding the Zr-based systems, much of the knowledge is owed to Borroto et al. within our research group at IJL [13–15], but another group has also reported results concerning them [38].

Dual-phase Zr-Mo thin films have been synthesized by sputtering thin films with a chemical composition that is intermediate between the amorphous and crystalline chemical

compositions. To do so, they synthesized 3 different thin films at a 2 Pa working pressure with compositions 48, 60 and 67 at% Mo, and characterized their structure. Their results are shown in Fig. 1.8, where one can see X-ray diffractograms as well as surface and cross-section SEM micrographs, a cross-section TEM micrograph, HRTEM images and their associated FFT [14].
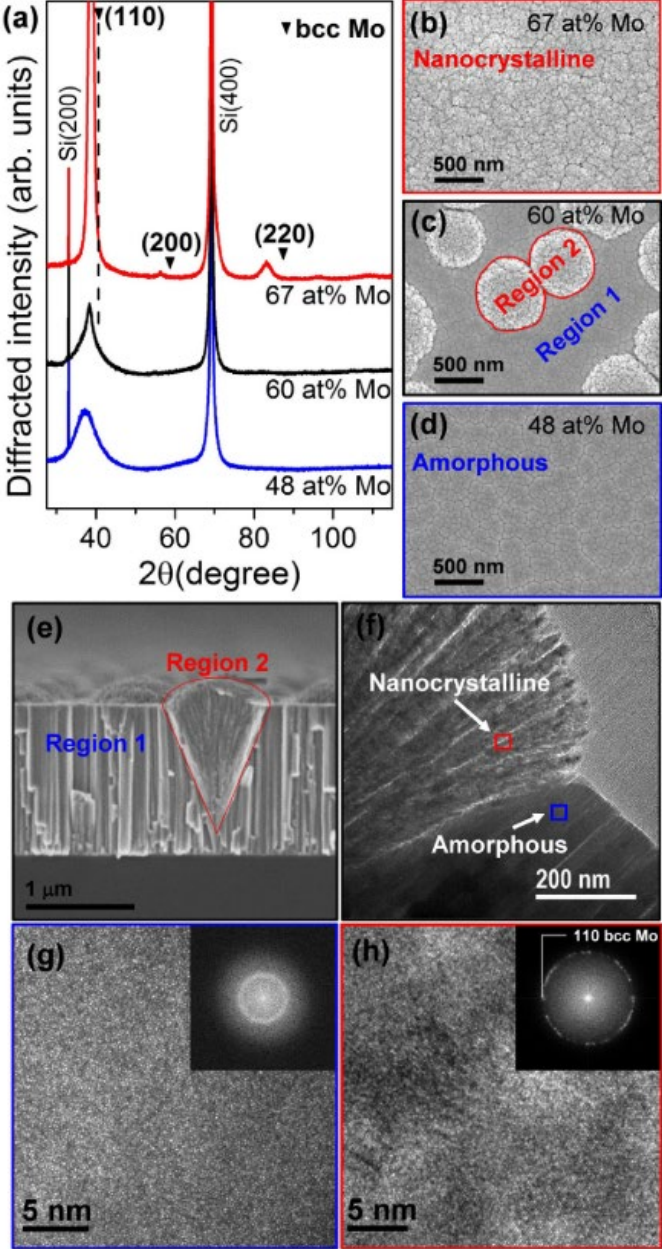
Fig 1.8: (a) X-ray diffractograms of the 3 synthesized thin films, (b-d) their surface SEM micrographs, (e) cross-section SEM micrograph of the dual-phase film, (f) cross-section TEM micrograph of the same film, (g) and (h) the HRTEM images and associated FFT of the amorphous and nanocrystalline phases, respectively. From Ref [14].

Similarly, the same group has reported that the same phenomenon was occurring in the Zr-W system, in which films exhibit the same morphology, and it is shown that the surface morphology can effectively be tailored via 2 levers: the chemical composition that governs the nucleation density of the crystalline regions, and the thickness that governs their growth and thus their apparent radius on the surface, as can be seen in Fig. 1.9 (a).
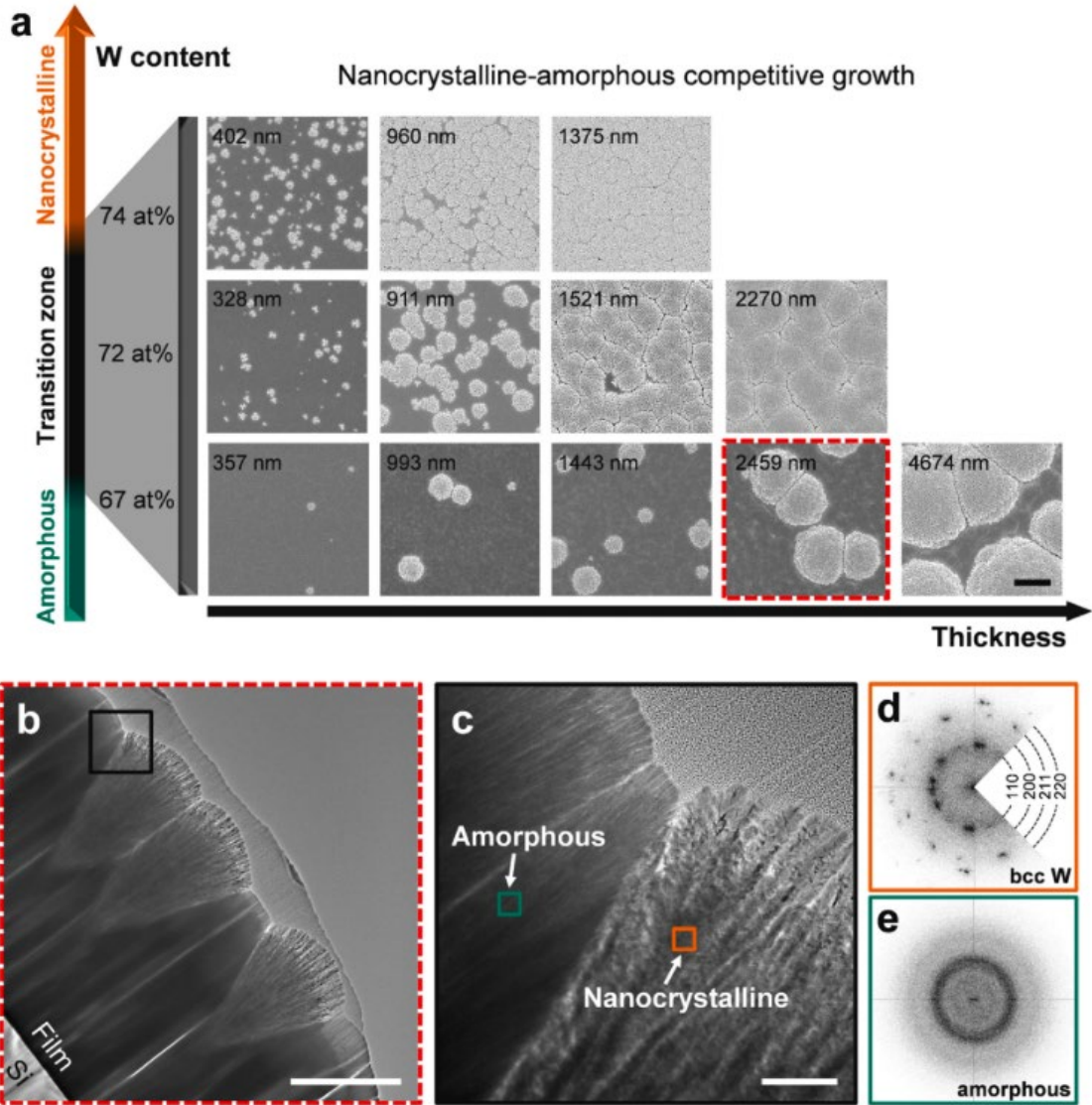
Fig. 1.9: (a) Different Zr-W thin films synthesized at different chemical compositions and thicknesses, resulting in different nucleation density, growth, and thus surface coverage by the crystalline phase, (b-c) cross-section TEM micrographs showing the interface between the two phases, (d) and (e) the FFT of the crystalline and amorphous phases, respectively. From Ref. [13].

Independently of these results, another group made the same observations with the Zr-W system, but with a lower working pressure of 0.53 Pa. They sputtered a thin film containing 72 at.% W, and it results in a dual-phase glassy-crystalline thin film, as is shown in Fig. 1.10 [38].
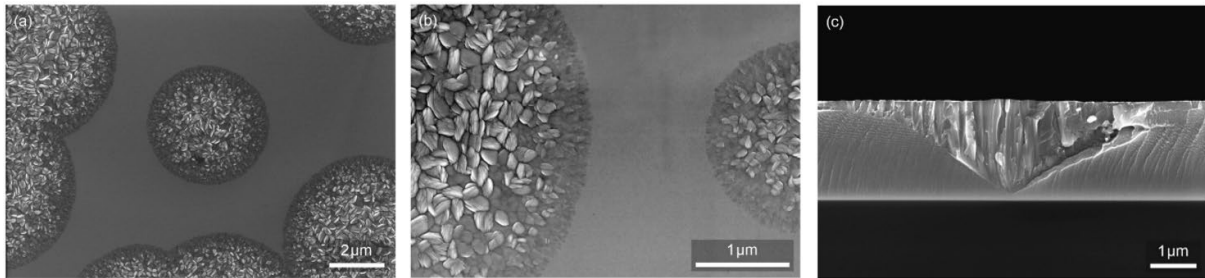
Fig. 1.10: Surface (a-b) and cross-section (c) SEM micrographs of the dual-phase Zr-W thin film grown at a 0.53 Pa working pressure. From Ref [38].

Here, the amorphous matrix is not columnar but rather a featureless metallic glass, and the top of the cones are not hemispherical. This suggests that the competitive growth phenomenon exists at different deposition pressures, but the geometrical shape of the crystalline phase may vary. In fact, the same observation has been made by Borroto et al. in the Zr-Mo system at a 0.5 Pa working pressure, and the resulting TEM images of the film are shown in Fig. 1.11. The authors explain this microstructural change by the increase of the kinetic energy of the atoms arriving to the surface of the film favoring their mobility in the in-plane direction, thus increasing the in-plane growth rate [14]. This hypothesis also explains the increased crystalline cone angle when the working pressure decreases.
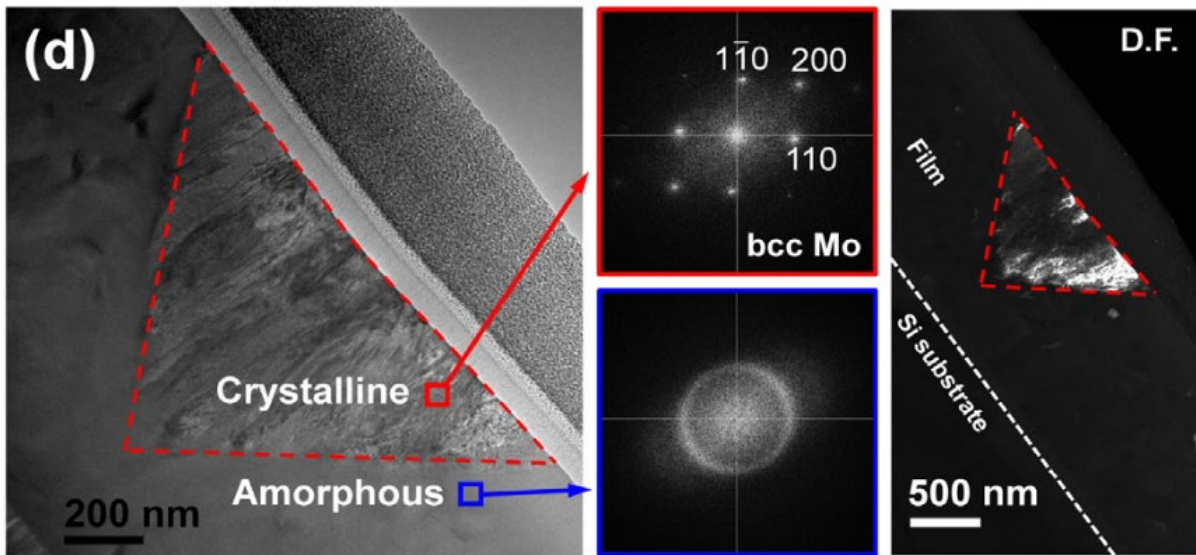
Fig. 1.11: Cross-section TEM image of a Zr-Mo film grown at low working pressure (left), FFT from the highlighted regions (middle), and dark-field image of the film (right). From Ref [14].

Borroto et al. also studied the evolution of the internal stress in the films after deposition for different thicknesses and different chemical compositions. As can be seen in Fig. 1.12 (a), in the first stage of deposition when only the amorphous phase grows, the internal stress is highly compressive. This is because atoms arriving on the surface pack closer than in the bulk state, which creates an increased atomic density. When the deposition continues and this layer is buried, its expansion is suppressed and this leads to a compressive stress in the film [15]. After that, nucleation arises and a tensile component appears, which is a stress relaxation due to the growth of the crystalline phase which is denser than the amorphous one, leading to a volume contraction of the film. As can be seen in Fig. 1.12 (a), the most relaxed stress state is reached at a lower thickness when the composition is closer to the crystalline phase (i.e. the W content increases) as a result of the lower thickness needed to start nucleation. The authors attributed the compressive stress that appears afterwards to the fact that the crystalline regions coalesce, suppressing to possibility for the crystallites to expand further, but new crystallites still nucleate, compete with each other and a compressive stress results from this.
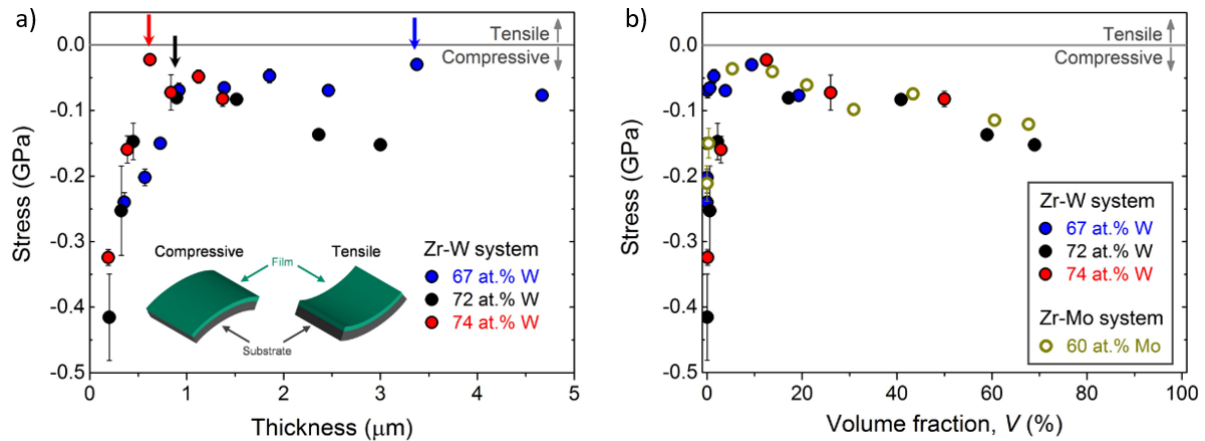
Fig 1.12: Evolution of the internal stress in the film depending on its thickness (a), and depending on the crystalline volume fraction (b). The arrows in (a) show the thickness of the most relaxed stress state in the film. From Ref [15].

One way of normalizing results from films with different chemical compositions is by comparing the internal stress not with the thickness of the film, but rather with the crystalline volume fraction. Moreover, it even exhibits similarity with the Zr-Mo system, as shown in Fig. 1.12 (b). This normalization is interesting and could potentially be expanded for a generalization of the competitive growth phenomenon to other Zr-based or even Zr-less systems.

While some articles have shown observations of this phenomenon, the nucleation mechanism of the crystalline phase still remains unclear. The substrate temperature does not exceed 45 °C during deposition, so crystallization from temperature increase is unlikely [14]. Nevertheless, the temperature of the extreme surface, which is not experimentally accessible, may be much higher than that due to the high kinetic energy of the atoms arriving to the surface of the film and allow enough adatom surface diffusion to trigger nucleation [39]. Regardless, other nucleation mechanisms must be sought.

A nucleation mechanism already mentioned is a local change in chemical composition. They observed a grain boundary nucleation, so it has been proposed that nucleation may

originate from different surface diffusion rates of Zr and Mo on the surface, leading to a segregation of Mo at the grain boundaries and a Mo-richer chemical composition that could nucleate [14].

Obviously, as the surface morphology is altered when the thickness or chemical composition varies, the surface can be tailored for specific applications. It has been shown that Zr-Mo dual-phase thin films turn from hydrophobic to hydrophilic when the thickness increases due to the coalescence of the crystalline regions [13]. Another tunable surface-related property is the reflectance. In fact, the diffuse and specular components of the reflectance strongly increases and decreases with the thickness, respectively; the total reflectance only decreases by 14 % in the meantime. Borroto et al. showed that the diffuse and spectral reflectance can almost be controlled at wish [13]. The tunability of the surface morphology allows the control of the surface-related properties of these thin films, which is the most interesting application field for such films.

1.2.3 Other systems

While the amorphous-crystalline competitive growth in the Si:H system is the most studied due to the time elapsed since its discovery and its usefulness in solar cells for its enhanced optoelectronic properties, and the Zr-based systems gaining attention in the last years, in some other systems has this competitive growth also been found.

Al-N thin films grown by radio frequency (RF) reactive magnetron sputtering have also shown competitive growth between amorphous and crystalline phases in 2007 already [40]. They used an Al target with a percentage $N_2 / (Ar + N_2)$ set to 75 %. A TEM dark-field micrograph of their sample is shown in Fig. 1.13 (a).

Using a compound Ti-Al target, Kolkovsky et al. Also observed this competitive growth in their sputtered thin film, as is shown in Fig. 1.13 (b). However, besides mentioning their discovery, the authors did not push further the studies on this thin film [41].

Another group observed the same phenomenon by synthesizing $BaTiO_3$ thin films from a $BaTiO_3$ target by pulsed laser deposition (PLD) onto a sapphire substrate [42]. Again, this result is mentioned but without additional results or studies. The bright-field TEM micrograph of this film is shown in Fig. 1.13 (c).

Finally, Gago et al. reported a competitive growth between amorphous TiO_2 and crystalline rutile phase by pulsed reactive magnetron sputtering [30]. The authors sputtered 3 thin films with a different O_2 concentration in the gas mixture, and showed that the nucleation and growth kinetics of the rutile phase depended with regard to the O_2 concentration. TEM micrographs and SAED patterns of their thin film sputtered with 50% O_2 concentration is shown in Fig. 1.13 (d, e). In these thin films, the conical regions do not show a hemispherical cap, and the authors attributed it to a higher lateral growth rate of the rutile phase with regards to the amorphous phase, but the opposite for the vertical growth rate.
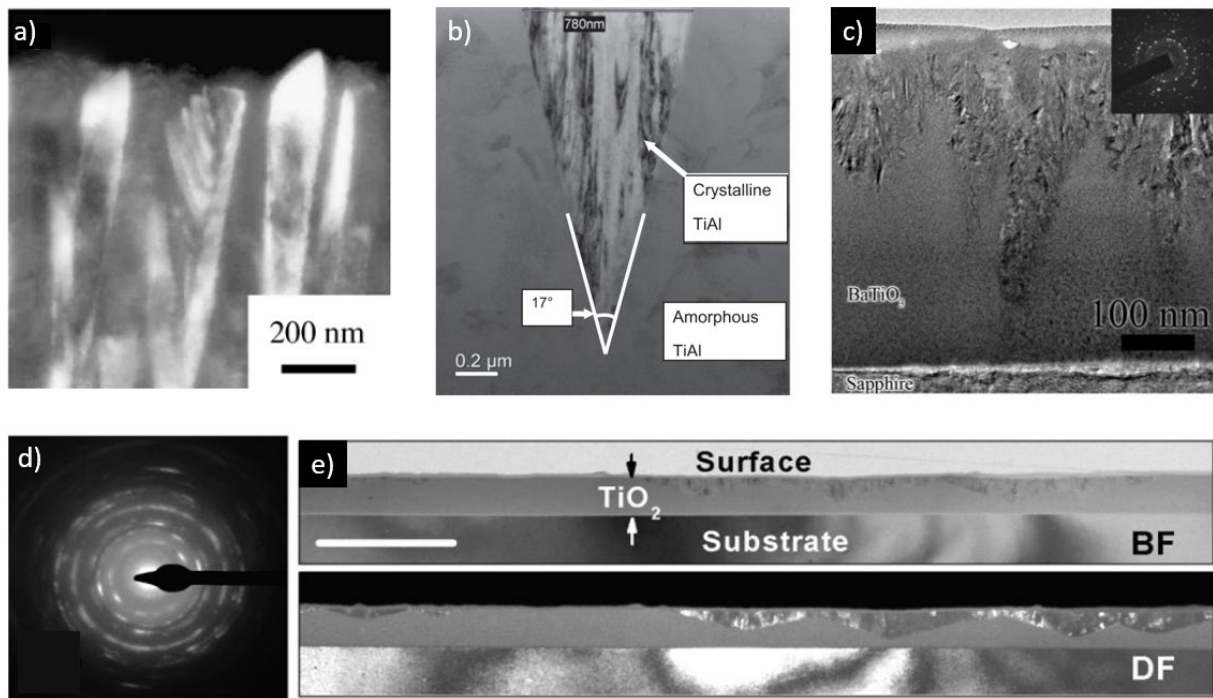
Fig. 1.13: Dark-field TEM micrograph of an Al-N thin film grown by RF reactive magnetron sputtering (a) [40], cross-section SEM micrograph of a Ti-Al thin film (b) [41], bright-field cross-sectional TEM micrograph of a PLD-deposited BaTiO$_3$ thin film (c) [42], and cross-section TEM micrographs showing bright-field (top), dark-field (bottom) and associated SAED pattern (left) of a TiO$_2$ thin film (d) [30].

As presented, these dual-phase thin films can be synthesized with a wide variety of materials, using different deposition techniques. Some have been thoroughly studied such as Si:H, while some other have only been mentioned in the literature. The applications for these thin films are often surface-related, as for instance the reflectance or wettability for the Zr-based thin films [13,14]. Naturally, the ability to tailor the surface properties is interesting, even though we only scratched the surface of what is possible with such films. Their high surface area combined with micro- and nano-structures makes them good candidates for different applications. In this work, another surface-related property of these films will be studied: the antibacterial property, that will be explained in the next chapter of this thesis.

1.3 Antibacterial properties of surfaces

Before diving into the antibacterial surfaces, some basic concepts of bacteria must be explained to have a better understanding on what they are, and how and why we fight them in the first place.

1.3.1 Context

All bacteria are not harmful for humans; some of them are even of paramount importance for our health [43]. Our intestinal microbiota is the perfect example of this, composed of more than 35 000 bacterial species, and playing a major role in our overall health [44]. However, some bacteria are harmful to humans or even to a civilization; take the example of the Black Death, when the bacteria Yersinia pestis has been responsible of between 75 and 200 million deaths in only 7 years during the 14th century in Western Eurasia and North Africa. In Europe, it is estimated that at least one third of their population at that time died from this plague [45]. It has also significantly reduced the global world population. These harmful bacteria are the ones that we seek to fight with many different strategies.

This is what "antibacterial" means, to reduce the harmful effect of bacteria. To do so, many different strategies exist, and each has different effects on the bacteria. Different approaches exist to have an antibacterial effect: heat, chemicals, antibiotic drugs, bacteriophage, bactericidal surfaces all exhibit antibacterial properties.

We use heat every day to kill bacteria without even thinking about it. The vast majority of the milk we buy has been pasteurized, which means that it spent a certain time at a high enough temperature to kill the bacteria to expand its shelf life [46]. In the same way, we have to cook poultry to at least 74°C to ensure that the Campylobacter, Salmonella and Clostridium perfringens bacteria, the most commonly found in poultry, are dead. Heat and time play hand to hand in this process, the aforementioned temperature stated to kill bacteria in poultry means

that the bacteria are instantaneously killed at this temperature, but maintaining a 63°C temperature for longer yields the same result.

Soap and hand sanitizer are also used daily to wash away the germs on our hands, after contact with potentially contaminated surfaces [47].

In 1910, the commercialization of the first antibiotics to kill bacteria was the greatest medical breakthrough in the 20th century for health, saving millions of lives and even extended the human lifespan of 23 years at this time [48]. Unfortunately, the excessive use and misuse of these drugs all around the world has led to a problem which is yet to be solved: the bacteria developed an antibiotic resistance [49]. To understand antibiotics resistance, we first need to understand how antibiotics work.

Antibiotics may have different uses depending on the type used: some kill the bacteria cells, and some other block their vital processes making them unable to function properly or to multiply and spread, helping the immune system deal with the infection. However, as some bacteria exhibit mutations, there is a possibility that a mutation helps the bacteria to resist against antibiotics. In some cases, this bacterium then spreads and can be transmitted, along with its newly acquired antibiotics resistance [50]. If nothing is done to stop excessive antibiotics use and find new treatments, we could be on our way to a post-antibiotic era, where we could die from bacterial infections again [51].

A promising candidate to kill bacteria is the bacteriophage therapy. Bacteriophages are viruses that infect and kill bacteria with a great efficiency and a high specificity, and they are present in all ecosystems that support bacteria growth, including the human body [52,53]. This is not a novel discovery, it has been first observed and reported in the 1910s [54]. The research on bacteriophages began just before the discovery of penicillin by Alexander Fleming; this event stopped the development of phage therapy, as penicillin could be mass produced with immediate results on global health [55].

Nowadays, an upsurge in bacteriophage therapy is observed, as bacteriophages have been shown to protect mice from a lethal level of E. Coli better than various antibiotics [56], and has even been tested with success to treat patients infected with antibiotic-resistant bacteria [57]. Phages are also more effective than antibiotics to infiltrate biofilms [58]. Their number is estimated at about 10^{31} bacteriophages on Earth, making them readily available [59]. The potential longevity of bacteriophage therapy is higher than for antibiotics, as it has been hypothesized that bacteriophages evolve alongside the bacteria, mutating to adapt and once again infect the resistant bacteria [59]. Moreover, bacteriophage resistance can in some cases be associated with a lower virulence due to surface modification of the bacteria [60].

The last antibacterial approach that will be mentioned here is antibacterial surfaces. They can be divided in two categories: antiadhesive surfaces and bactericidal surfaces. The first one prohibits or inhibits bacterial adhesion on a surface, avoiding further contamination from this surface [61], while the latter consists in a surface usually made of known antibacterial metals, such as copper or silver [62]. Such antibacterial surfaces are the focus of this work, and the mechanisms behind their antibacterial efficiency will be discussed in a further section.

1.3.2 Bacteria structure

To understand the mechanisms of bacterial spread, biofilm formation and bactericidal effect, one should know the structure of a bacterial cell.

Bacterial cells are prokaryotes, which is a single-cell organism without nucleus. The typical structure of a bacterial cell is presented in Fig. 1.14.
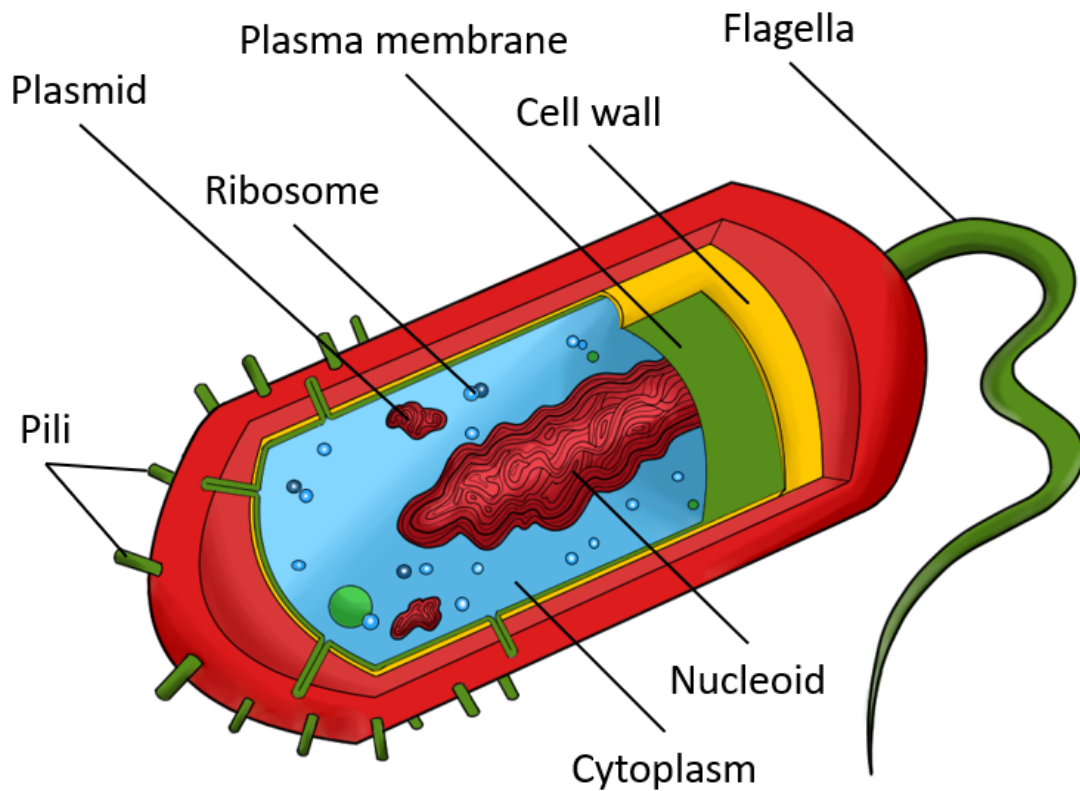
Fig. 1.14: Drawing of a prokaryote cell, which the bacteria belong to.

As can be seen in Fig. 1.14, a bacterial cell is surrounded by a cell wall that encloses the cells content and acts as a barrier to protect the bacterial cell from the outside, and to hold nutrients, proteins and cytoplasm inside the cell [63]. The genetic material of bacteria is typically a single circular bacterial chromosome of DNA; it is called the nucleoid, and is located in the cytoplasm. It contains the chromosome with its RNA and proteins, and is responsible for all the genetic information for living in normal conditions. The bacterial cell also contains ribosomes and plasmids. The ribosomes are used for the production of proteins, while the plasmids are small extrachromosomal DNA molecules that can replicate independently of the bacterial cell [64,65]. They often carry genes that benefit the bacteria survival under specific conditions, such as antibiotic resistance for instance, and can even be transmitted between different bacteria species [66].

As mentioned earlier, the bacterial cell is surrounded by a cell wall. Bacterial cells can be classified in two types according to their cell walls: Gram-positive bacteria and Gram-negative bacteria. These names originate from the test used to classify bacterial species, the Gram stain test. The difference between these two types of bacteria is their cell walls, as shown in Fig. 1.15.

Gram-negative bacteria (such as Escherichia Coli) are composed of 3 main layers, the first one being a plasma membrane, which is a phospholipid bilayer. In the case of E. Coli, the principal phospholipids found are phosphatidyl ethanolamine and phosphatidyl glycerol. We also find proteins in this membrane, which are useful for energy production, lipid biosynthesis protein secretion and transport [67]. It usually is less than 10 nm-thick. The next layer is the periplasm, which is an aqueous compartment densely packed with proteins. It sequesters potentially harmful enzymes and also contains proteins useful for transport. In this layer we also find the peptidoglycan, consisting of polysaccharide chains cross-linked by peptides containing D-amino acids [68]. The last layer is the outer membrane that contains phospholipids, some proteins and lipopolysaccharide. It differs from the plasma membrane as it lacks enzymatic activity and contains more lipopolysaccharide. Its main function is to act as a protective barrier for the bacterium.

Gram-positive bacteria (such as Bacillus Subtilis) differ from Gram-negative ones on their outermost layer. Their first layer is the same plasma membrane, but they lack the outer membrane that protects Gram-negative cells from their environment by excluding toxic threats. To counterbalance this absence of outer membrane, the Gram-positive bacteria are covered by a peptidoglycan layer many times thicker than their counterparts, threaded by long anionic polymers, namely teichoic acid covalently bonded to the peptidoglycan and lipoteichoic acid anchored to the cell membrane [69].
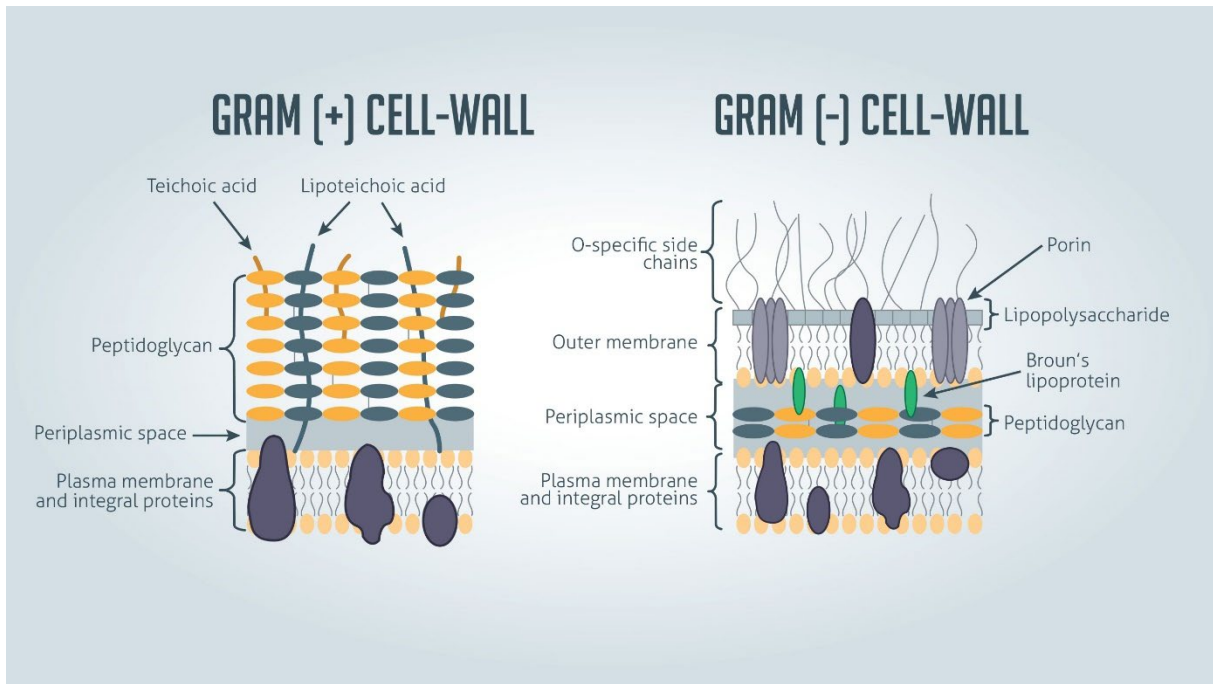
Fig. 1.15: Schematic drawing of Gram-positive and Gram-negative cell walls.

Outside of this cell wall are found the last components of the bacterial cell, which are different organelles, serving different purposes (see Fig. 1.14). The largest one is the flagellum, used by the bacterium for motility purposes, but in some cases can also be used as a sensory organelle [70]. Bacterial cells surface also presents pili, which possess adhesins, allowing the bacterial cell to attach a surface; they are also associated with higher virulence as this increases the replication rate and ability to interact with a host [71]. The last appendage is curli fibers, that are also used for adhesion to surfaces as well as quorum sensing.

1.3.3 Biofilm formation

A biofilm is an architectural colony of bacteria, within a matrix of extracellular polymeric substance (EPS) that they produce. This biofilm irreversibly adheres to a surface, and is pathogenic, meaning it can cause nosocomial infections, as it is associated to 65% of all microbial infections [72]. The schematic drawing of its formation is shown in Fig. 1.16. It begins with the initial attachment of a bacterium to the surface; bacteria adhere to the surface

through their surface appendages (pilli, flagella). Then, when the bacteria have adhered to the surface and interact together, the biofilm formation begins. At this point, the process of multiplication and division of cells starts, initiated through chemical signaling within the EPS matrix. The bacterial colony in a thin film may consist of many types of micro-organisms coordinated with one another [73]. When the required cell density it attained, quick multiplication and dispersion of bacteria is observed, releasing planktonic bacteria that spread to colonize new sites. This detachment aids in the spreading of infections [74]. The biofilms also exhibit increased resistance against antimicrobial agents, antibiotics and host defense [75–78].
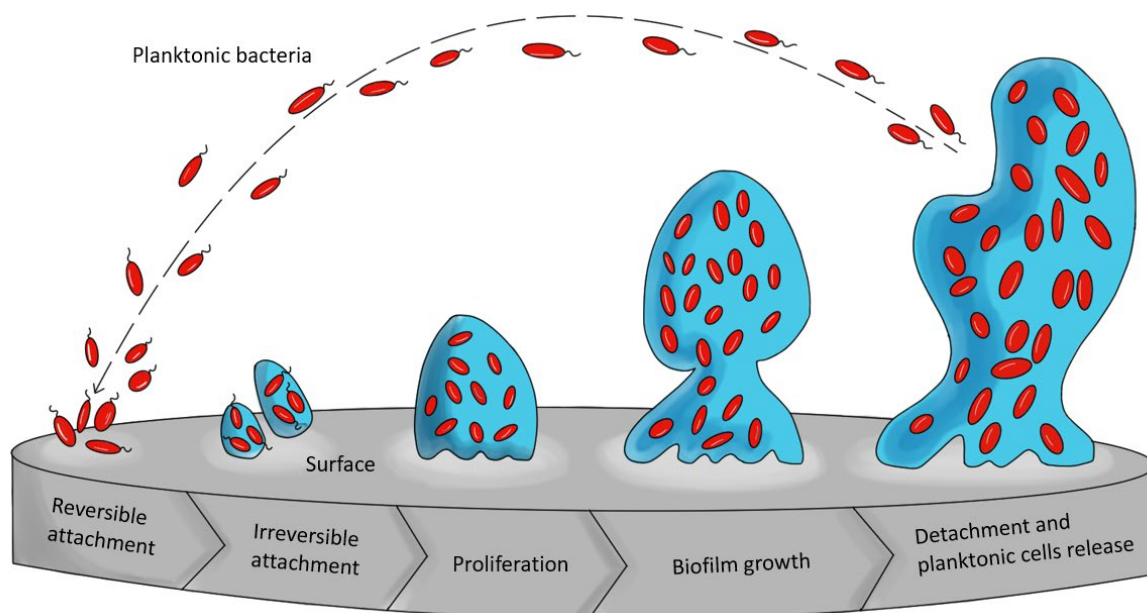
Fig. 1.16: Schematic drawing of the formation of a biofilm, from the attachment of a bacterium to the release of bacteria.

Thus, an interesting approach to inhibit the formation of bacterial biofilms and their associated infections would be the elaboration of surfaces that limit the bacterial adhesion.

1.3.4 Bacterial adhesion on surfaces

The first step of a biofilm being the adhesion of a bacteria to a surface, limiting this adhesion is a great way of avoiding the formation of harmful bacterial biofilms. To be more precise, this adhesion step usually is a two-step process, these steps being commonly called reversible and irreversible attachment stages. The first, reversible, attachment stage occurs in around 1 min, and is governed by hydrodynamics and physicochemical (electrostatic and Van der Waals) interactions between the cell and the surface [79,80]. Most bacteria have a negative surface charge, meaning that they would interact preferentially with positively-charged surfaces. However, this effect disappears when the bacteria are in a high ionic strength media, due to charge screening [81]. The second attachment step is irreversible and occurs in several hours, involving Van der Waals interactions between the outer cell wall and the surface [81]. These two steps are shown in Fig. 1.17 (b). Naturally, surface chemistry and topography will change the adhesion of bacteria to the surface [7,82]. As an example, it has been shown that an appropriate roughness on stainless steel could reduce the number of adhered bacteria by 10-fold [83].

Bacteria have different methods to ensure adhesion to a surface; they have a variety of organelles such as pili, flagella and curli fibers as depicted in Fig. 1.17 (a), and these organelles are frequently terminated with proteins that can bind to different surfaces [84,85]. The bacteria can also produce EPS to anchor themselves onto a surface [86,87].
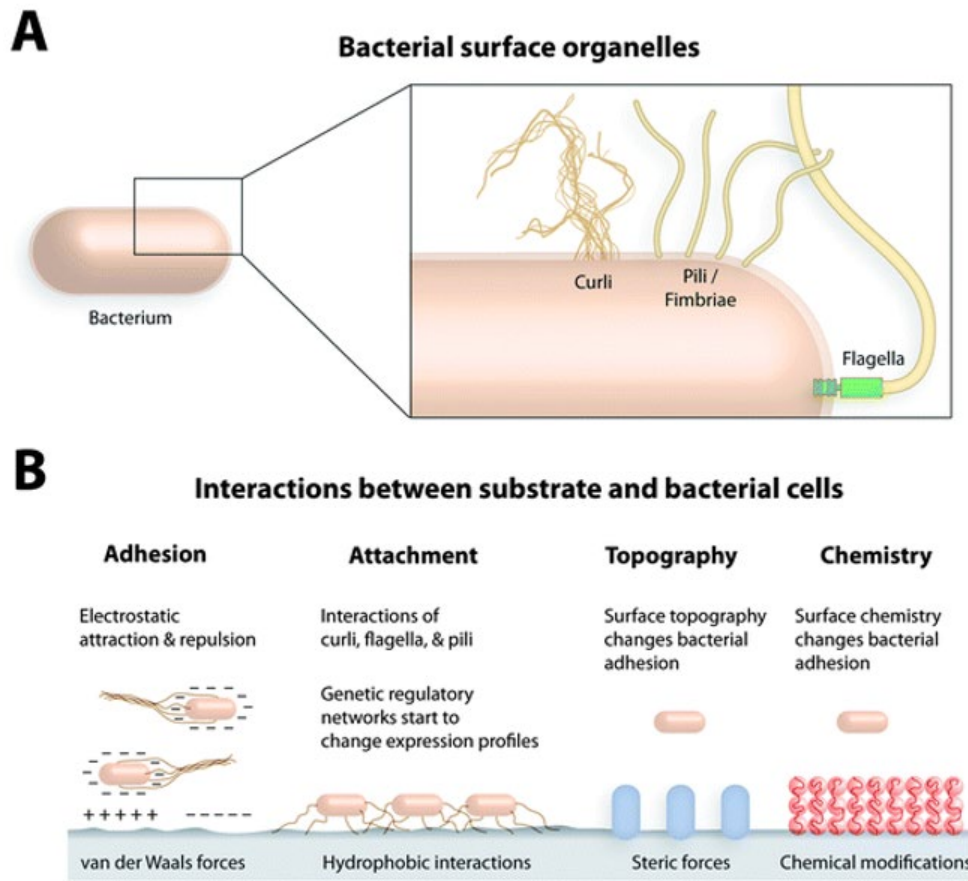
Fig. 1.17: The organelles that bacteria can use to move in a media and to adhere to a surface (a), and the different types of interaction that happen between a bacterial cell and a surface (b). From Ref. [88].

1.3.5 Bactericidal effect (contact-killing)

Another type of antibacterial surfaces exists: the bactericidal surfaces; these do not seek to avoid bacterial adhesion, as they behave as active antibiotic, disrupting the bacterial cells or inactivating their growth. Many ways to elaborate such surfaces exist, the most widespread being the use of intrinsically bactericidal materials, such as copper of silver, whose ionic forms have been shown to have a strong bactericidal effect [89]. It has been found that copper alloys with as low as a 60 at.% Cu composition are efficient in killing bacteria at contact [90]. Nowadays, with advanced coating techniques, it is possible to coat a surface with a wide range

of materials, to take advantage of all forms of materials and their properties. Thus, pure metals [91,92], metallic alloys [93,94], composites [95,96], oxides [97,98], nano-structured surfaces [99,100] have been deposited on surfaces to benefit from their bactericidal properties.

Currently, three mechanisms for bacterial death from contact with copper have been reported, which are shown in Fig. 1.18. The first one results from the physical interaction between the cell membrane and a copper nanoparticle, which can lead to the destruction of the membrane or infiltration of the nanoparticle, making the cell susceptible to damage from copper ions [89,101,102]. This effect has been shown to be enhanced by smaller nanoparticles (from 1 to 10 nm), as they can infiltrate the cell and release copper ions at the same time [103]. The second one is the formation of reactive oxygen species (ROS) inside the cell by a reduction of copper. The newly-formed ROS, being highly reactive, react with the vital parts of the cell and damage the proteins, enzymes and DNA of the cell [104–106]. The last mechanism is the release of copper ions (Cu^+ and Cu^{2+}) from a copper surface which can also damage the membrane, reach the cell and generate ROS which will in turn damage the cell, leading to its death [90,107,108]. Even though these three bactericidal mechanisms have been identified, it is still unknown to which extent they contribute to the actual bacterial death.
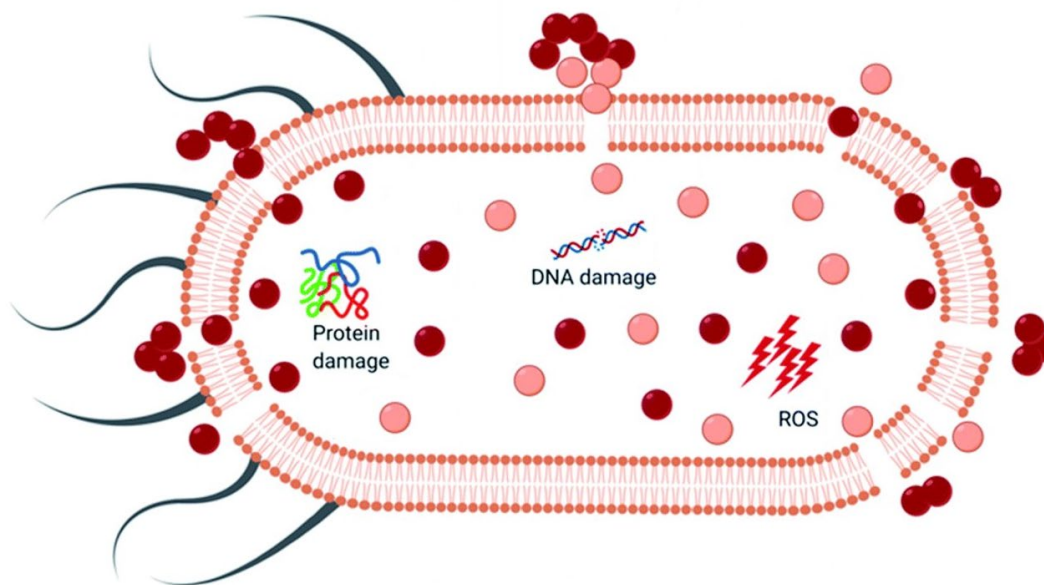
Fig. 1.18: Schematic drawing of the effect of copper ions and nanoparticles on bacteria, virus, fungi and yeast, adapted from [109].

Other bactericidal materials can be mentioned, such as some natural molecules that are chitosan [110] and antibacterial peptides [111]. Using these molecules on surfaces is also a way to protect a surface from bacteria.

Moreover, it has also recently been demonstrated that some surfaces can mechanically kill bacteria by rupturing the bacterial cells. Nature has given us a few examples of this strategy, as such surfaces can be found on cicada wings or dragonfly wings, owing to the nanopillars found on their surface. The results of this study are shown in Fig. 1.19 (a, b), where the researchers traced the downwards movement of a bacterial cell on the nanopillars found on a cicada wing. After 220 seconds, a sharp drop is observed, corresponding to the mechanical rupture of the cell wall [112]. The adhesion of the bacterial cells on the surface of the nanostructured wings mechanically stretches the membrane, and a high enough stretching leads to membrane rupture, effectively killing the bacterial cell after its contact with the surface [113].

Biomimicry leads us to try and replicate such surfaces, which has recently shown great results, with up to 99% of bacteria inactivated within 24 hours [113].
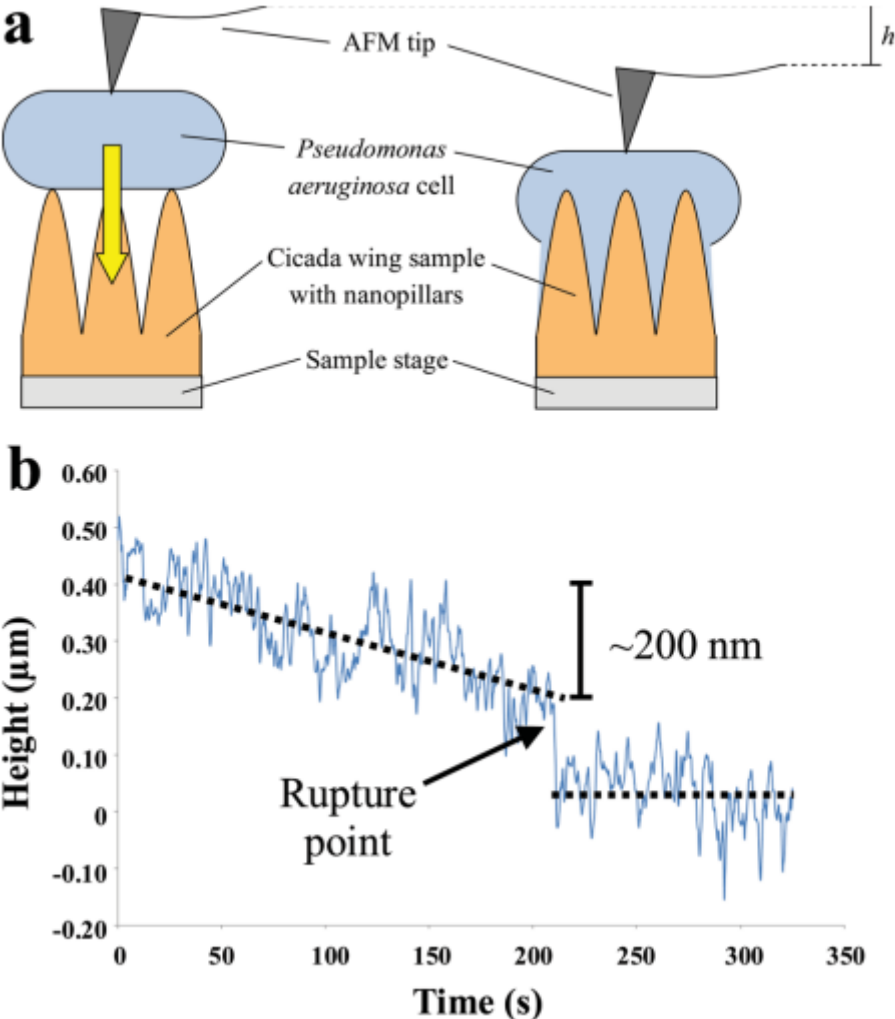
Fig 1.19: A Pseudomonas aeruginosa bacterial cell mechanically ruptured by the surface of a cicada wing (a), and the downwards movement of the bacterial cell over time (b). From Ref. [113].

Chapter 2

Thin films deposition and characterization methods

ABSTRACT: In this chapter are described the thin films sputtering methods as well as the characterizations used in this study. First, the details on the sputtering process are explained, then we dive into the characterization processes, whether it is for the material analysis or its antibacterial properties.

Contents

2.1 Thin films synthesis

2.1.1   Deposition chamber

The same deposition chamber has been used for the synthesis of all the thin films in this study. The deposition chamber is pumped down via a mechanical and a turbo-molecular pumps allowing a base pressure of 10^{-6} Pa. The magnetrons are balanced in this chamber, and the cathodes are mounted in a confocal configuration regarding the substrate holder. With substrate rotation, the thin films chemical composition is constant over the whole substrate holder surface, taking into account the uncertainty of the EDS measurement. A schematic representation of the deposition chamber is shown in Fig. 2.1. This work studies bi-phased alloys that were synthesized by co-sputtering, meaning that the Zr-Cr and Zr-V thin films were synthesized using a Zr target and a Cr target or a Zr and a V target, respectively. This chamber includes 4 cathodes, two of them are DC-powered while the others are RF-powered.
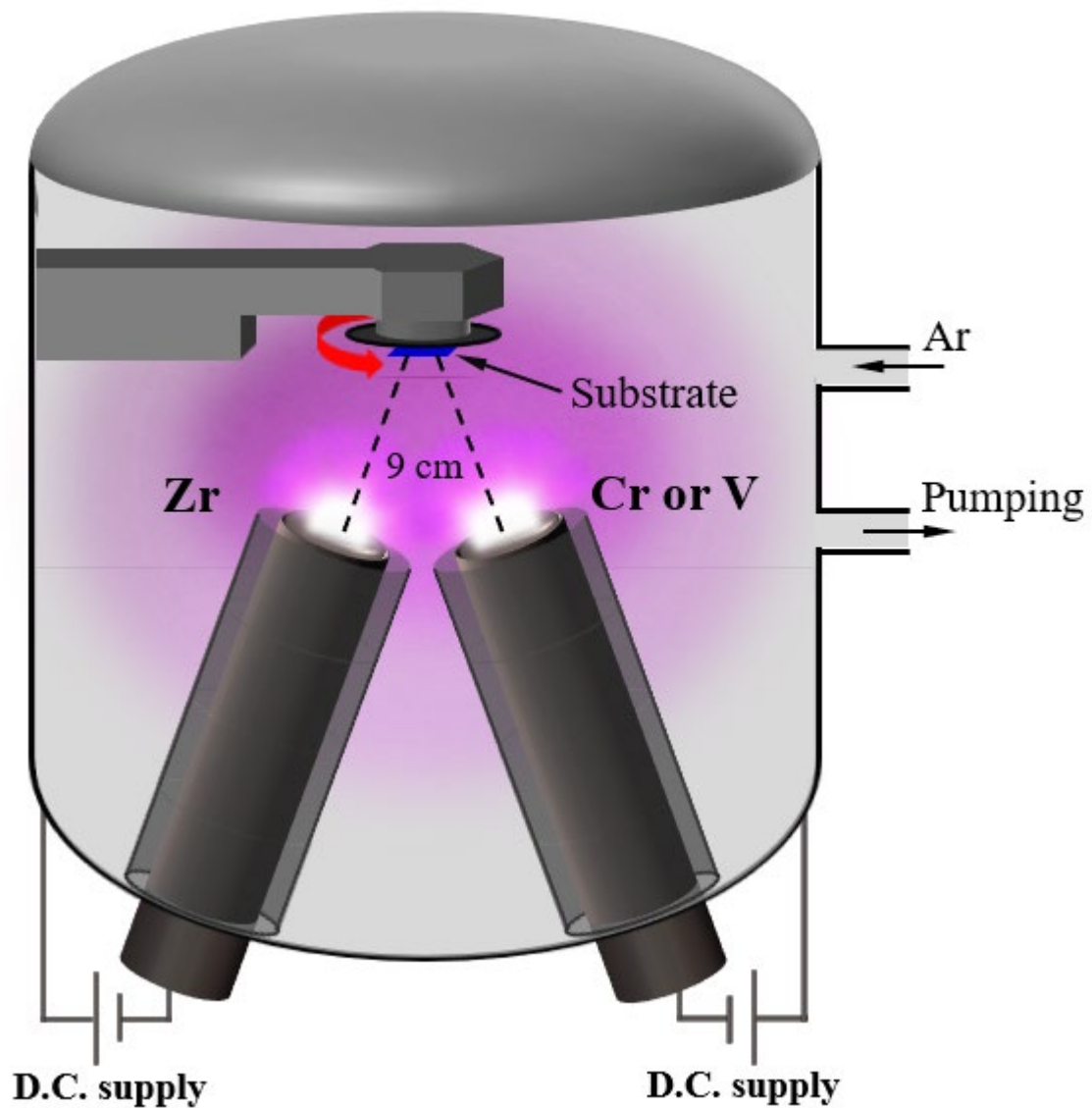
Fig. 2.1: Schematic representation of the deposition chamber used for the thin films synthesis with Zr and Cr targets as examples.

2.1.2 Zr-Cr thin films

The Zr-Cr thin films were deposited onto (100) monocrystalline Si substrates (15x15 mm²) using DC magnetron sputtering of Zr and Cr metallic targets (targets dimensions: 2 in. diameter, 3 mm thickness and purity higher than 99.9 %) in an argon atmosphere. The substrate-holder rotation was set at 15 rpm, the working argon pressure was 2 Pa and the targets to substrate distance was set to 9 cm for the two targets.

The study on the Zr-Cr thin films focuses on the morphology of the different phases in the thin films depending on the deposition rate. The deposition rate was controlled by the discharge current applied to the Zr target (0.04 A, 0.075 A, 0.15 A or 0.3 A). To each of these discharge current value corresponds one deposition rate reference (respectively 5, 11, 30 and 63 nm/min). For each deposition rate reference, the discharge current applied to the Cr target varied from 0.09 A to 0.72 A. This allowed controlling the chemical composition of the sputtered thin films, as the ratio of the atoms sputtered from each target was changed with only minor modification of the deposition rate around the reference rate. As can be seen in Fig. 2.2, the 4 different discharge currents applied to the Zr target result in 4 different deposition rate ranges. For each of these ranges, the discharge current on the Cr target varied to sputter thin films of different compositions. With this technique, a wide chemical composition range could be obtained without significant modification of the deposition rate.
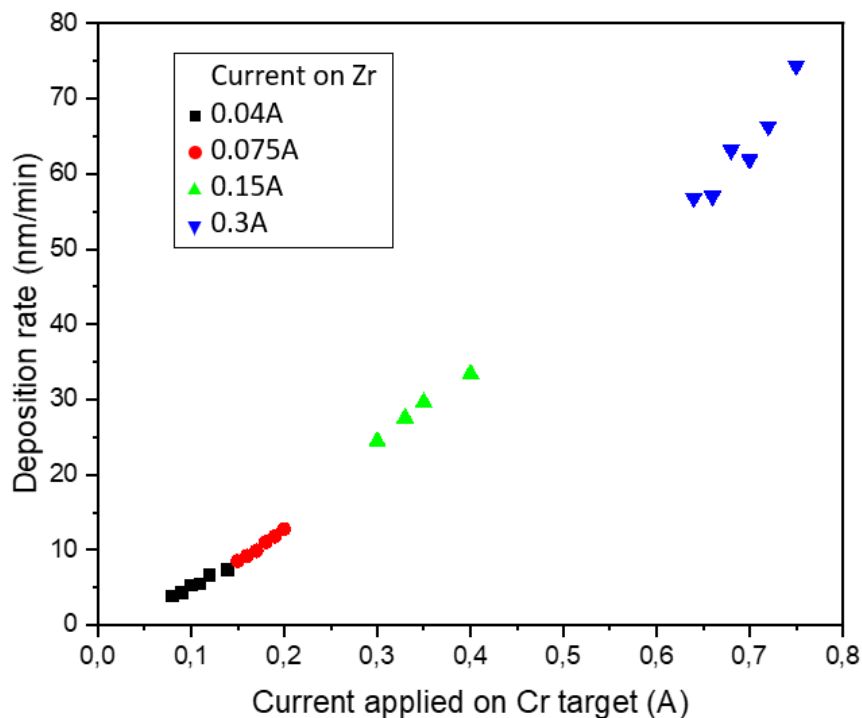
Fig. 2.2: Deposition rates of the Zr-Cr thin films studied. Each color corresponds to a given value of the discharge current applied to the Zr target.

This process allowed changing the composition between 82 and 88 at% Cr for deposition rates between 3.8 and 74 nm/min. The deposition time for these films varied from 20 to 240 min, the first being for the highest deposition rate and the latter for the lowest deposition rate. This ensured the synthesis of thin films with a thickness of 1–1.2 µm.

2.1.3   Zr-V thin films

For the Zr-V thin films, the same chamber parameters were used, and the targets were of the same geometry and purity. The substrate dimensions were 10 x 25 mm². The discharge current applied to the Zr and V targets was 0.1 A and 0.42 A, respectively. The deposition time varied between 15 and 120 min, resulting in 86 at% V thin films with a thickness varying between 230 nm and 2.3 µm. As will be further investigated, this vast deposition time range allows the control of the surface morphology thanks to the competitive growth between the amorphous and crystalline phases.

2.1.4   Cu-coated Zr-V thin films

The Cu-coated Zr-V thin films are the aforementioned Zr-V thin films, except they are covered by a 60 nm-thick Cu coating. Thus, the parameters for the Zr-V thin film deposition were the same. The Cu coating was deposited using a Cu metallic target on a third cathode right after the Zr-V deposition, without taking the sample out of the chamber. The Cu target was RF-powered, with an applied power of 150 W, and a deposition time of 90 s.

2.2 Thin films characterization

2.2.1   X-ray diffraction

X-ray diffraction (XRD) is a well-known characterization method in materials science that assesses the crystalline phases in a sample based on the interaction between monochromatic

X-rays and a crystalline sample. In this technique, a monochromatic X-ray beam is generated and sent towards the sample, where there will be an interaction between the X-rays and matter. When the matter is crystalline, X-rays are scattered by the atoms, and the resulting waves interfere, producing constructive or destructive interference. This process is repeated for a broad range of sample angles, and the result is called a diffractogram. The condition for an interference to be constructive is given by Bragg's law, illustrated on Fig. 2.3 (a):

$$2d_{hkl} \sin(\theta) = n\lambda \qquad (2.1)$$

Here, d_{hkl} is the interplanar spacing, θ is the scattering angle, λ is the wavelength of the incident X-ray and n is a positive integer that determines the order of reflection.

One of the most used geometrical configuration for XRD is the Bragg-Brentano configuration, where the X-ray source is fixed, and the sample and detector scan angular regions at $\dot{\theta}$ and $2\dot{\theta}$ rates, respectively. A schematic representation of the Bragg-Brentano configuration is given in Fig. 2.3 (a). In this configuration, the diffraction peaks correspond to crystallographic planes parallel to the surface. An example of X-ray diffractogram is shown on Fig. 2.3 (b), for a Zr-Cr thin film grown on a Si substrate.

A diffraction peak contains information on the structure and microstructure of the crystalline phase of the sample. The peak position gives the angle θ that can be used in Bragg's law to determine the interplanar spacing d_{hkl} and to identify the structure of the crystalline material. This will be used in the following chapters to identify the crystallographic orientation of the crystalline regions in our samples. The peak intensity gives information on the preferred crystallographic orientation, and the peak shape allows calculation of the crystallite size D (size of coherence domains) via Scherrer's formula [114]:

$$D = \frac{K\,\lambda}{\beta\,\cos(\theta)} \qquad (2.2)$$

With K Scherrer's constant, λ the radiation wavelength, β the full width at half maximum (FWHM) of the diffraction peak, and θ the Bragg's angle. These peak characteristics are shown on Fig. 2.3 (c).
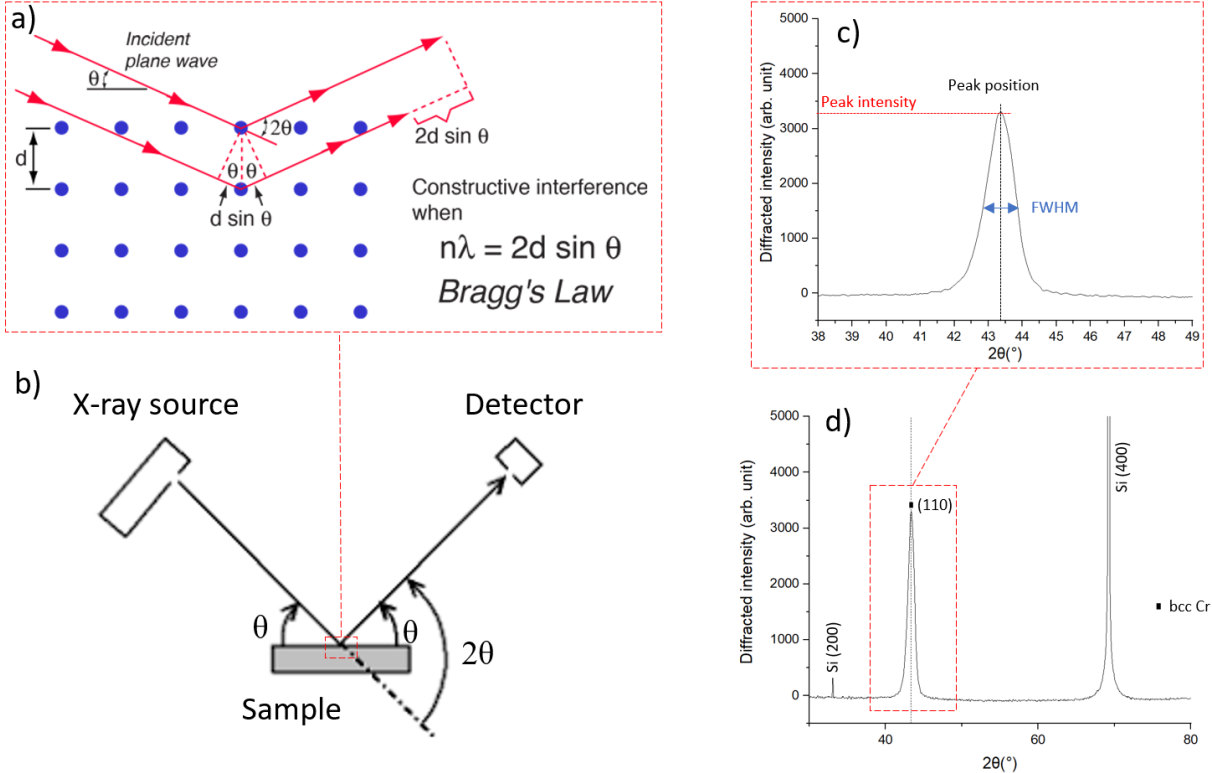
<u>Fig. 2.3</u>: Schematic representation of the Bragg's law (a) and the Bragg-Brentano configuration (b). Zoom on a bcc Cr peak showing the peak characteristics (c) and full range X-ray diffractogram of a Zr-Cr thin film (88 at.% Cr) grown on a Si substrate (d).

In this work, XRD measurements were conducted in Bragg-Brentano configuration using KαCu radiation (λ=1.5406 Å) in an AXS Bruker D8 Advance diffractometer.

2.2.2 Scanning electron microscopy and energy dispersive spectroscopy

Observation of a sample topography at high magnification is not possible with conventional optical microscopes, because spatial resolution and magnification are limited by the wavelength of the visible light. To obtain images of a sample at a higher magnification and

spatial resolution, we used scanning electron microscopy (SEM). In this technique, an electron beam accelerated by a few kV voltage scans the sample surface. The electron-matter interaction at the sample surface generates different signals originating from different interaction volumes below the surface and that can be detected with sensors: secondary electrons, element-specific X-rays or back-scattered electrons, among others. Secondary electrons are produced at a shallow depth from inelastic interactions between the electrons and the sample, making them useful for topographical examination of the surface. Backscattered electrons, on the other hand are produced in a broad region of the sample, and result from elastic collisions between the electrons and the sample's atoms; the number of backscattered electrons reaching the detector depends on the atomic number of the atom, the higher Z the higher the signal, resulting in a chemical contrast on the image. A schematic representation of an electron beam on a surface and the aforementioned interactions are presented in Fig. 2.4.

Electron beam

Auger electrons
~1 nm depth
Surface chemical composition

Backscattered electrons
~500 nm depth
Z and phase differences

Secondary electrons
~5-50 nm depth
Topographical information

Characteristic X-rays
~1-3 μm depth
Chemical composition
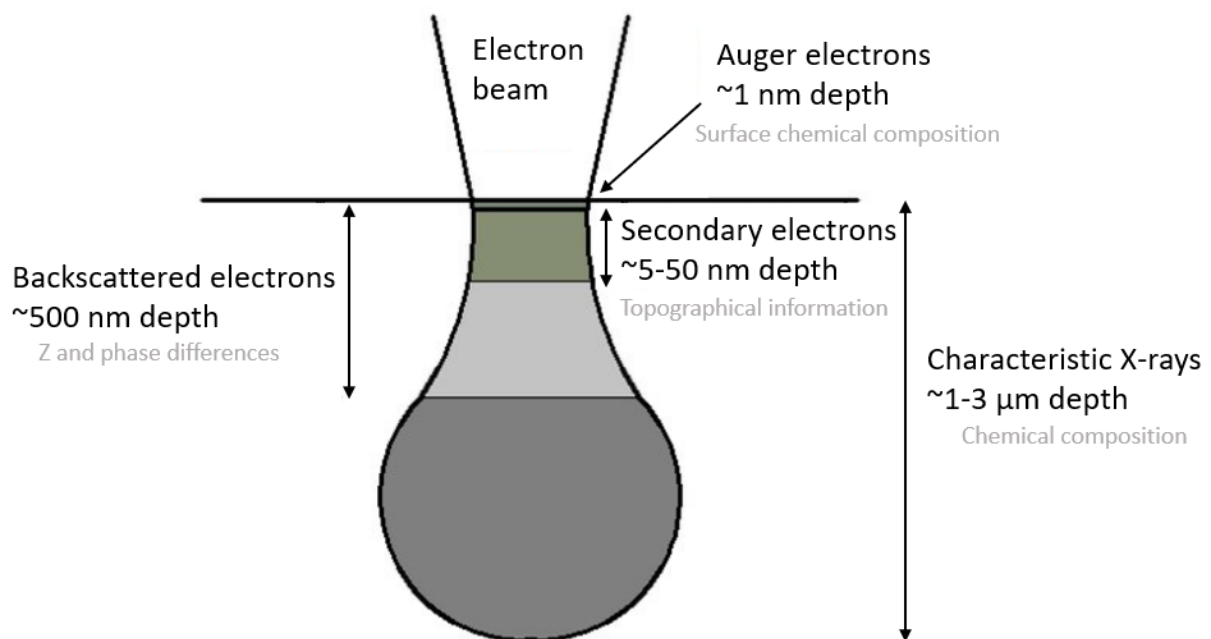
Fig. 2.4: Schematic representation of an electron beam interacting with a sample surface, and some of the signals generated by this interactions.

To acquire a high-resolution micrograph of a sample surface with topographic contrast, the secondary electrons can be collected. This technique has been used in this work to acquire surface micrographs and cross-section micrographs of the thin films, as can be seen in Fig. 2.5 (a, b).
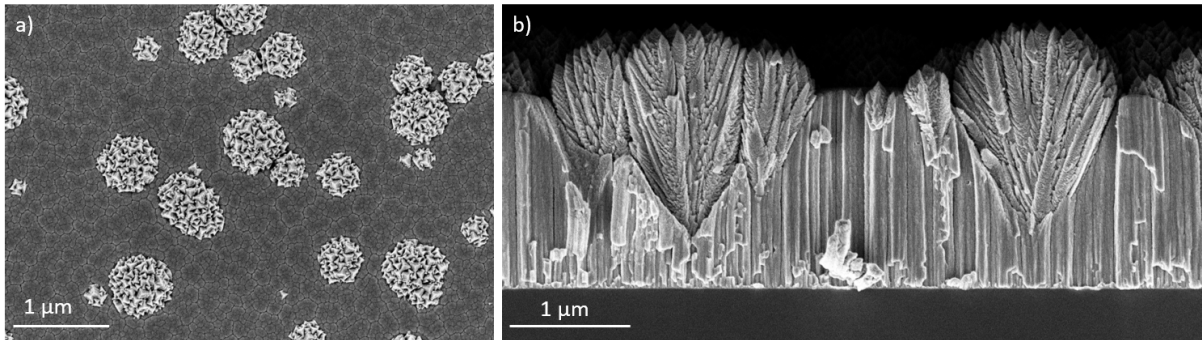
Fig. 2.5: (a) Surface SEM micrograph of the surface of a Zr-V thin film, and (b) cross-section SEM micrograph of a Zr-V thin film.

Moreover, most of the SEM nowadays are equipped with an energy dispersive spectroscopy (EDS) system, allowing the chemical analysis of the sample. For this analysis, the X-ray resulting from the beam-sample interaction is analyzed, and these X-rays are element-specific, meaning that their energy indicates the element that interacted with the electron beam. A typical EDS spectrum of a Zr-Cr film is presented in Fig. 2.6. For this film, we can observe the peaks corresponding to Zr, V and O from the film, and Si from the substrate. Oxygen is indeed present in the film, however EDS is known to overestimate the lightweight elements such as O, or C and N that are not even present in this film. This comes from the high background counts, an artefact due to the window in the detector and resulting in an artificial peak at low energies, thus rendering difficult the quantification of low-Z elements; in this work, the oxygen content in the films is neglected in the calculations of the chemical composition. Hence, for a Zr-V thin film, the calculation for the V content is $\frac{V}{Zr+V}$, as oxygen is neglected.
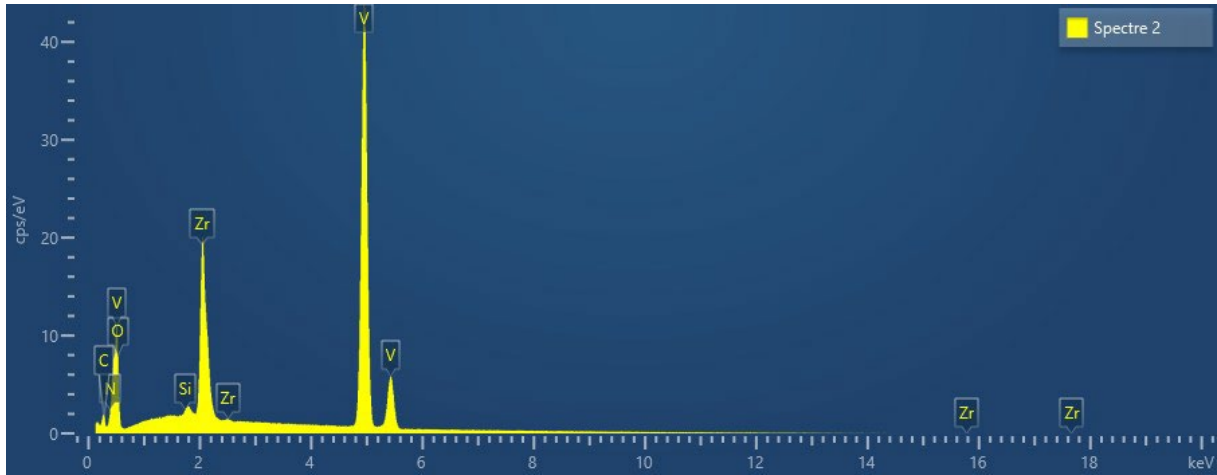
Fig. 2.6: EDS spectrum of a Zr-V thin film deposited on a Si substrate.

In this work, a Zeiss GeminiSEM 500 scanning electron microscope was used to analyze the morphology of the samples and to acquire the EDS spectra. For SEM cross-section analysis, the samples were cleaved with a diamond tip.

2.2.3 Transmission electron microscopy

Transmission electron microscopy (TEM) is a characterization technique used on very thin samples (~100nm), and allows high magnification imaging as well as electron diffraction of the sample. In this technique, a high-voltage electron beam (~200kV) is accelerated towards the sample and the transmitted electrons are collected. These electrons are then used to form the image of the sample.

Two main lenses configurations exist and can be switched inside a TEM, allowing to obtain either electron diffraction or an image. These 2 modes are schematized in Fig. 2.7. When the TEM is used in diffraction mode, an electron diffraction pattern is obtained, and this provides insight about the crystalline structure of the sample. On the other hand, when using the imaging mode, an image of the sample is obtained. In this mode, there are different image types that can be acquired, and they are reported in Fig. 2.8.
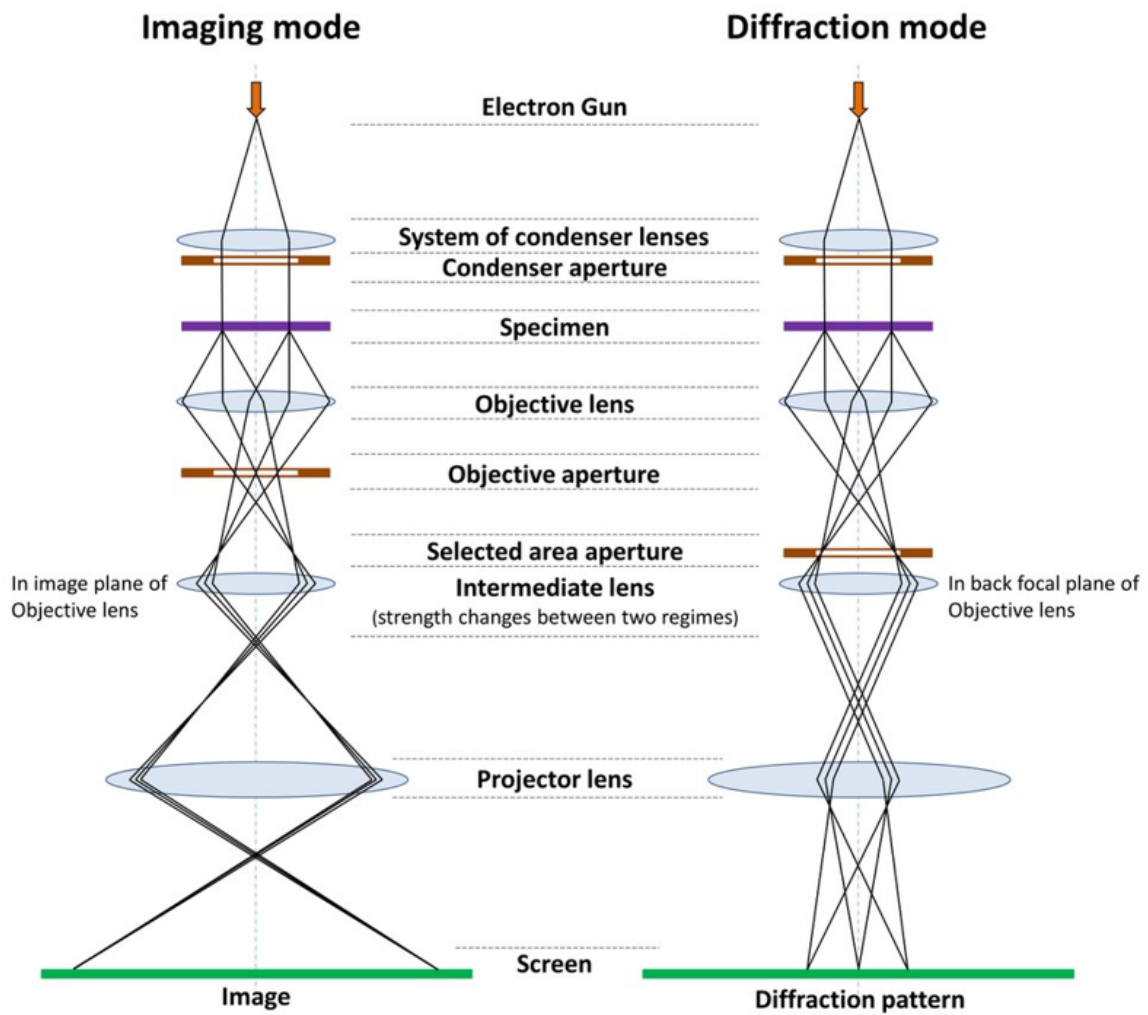
Fig. 2.7: Schematic of the two basic operating modes in a TEM. In image mode (left) the image is projected onto the screen, while in diffraction mode (right) the diffraction pattern is projected onto the screen.
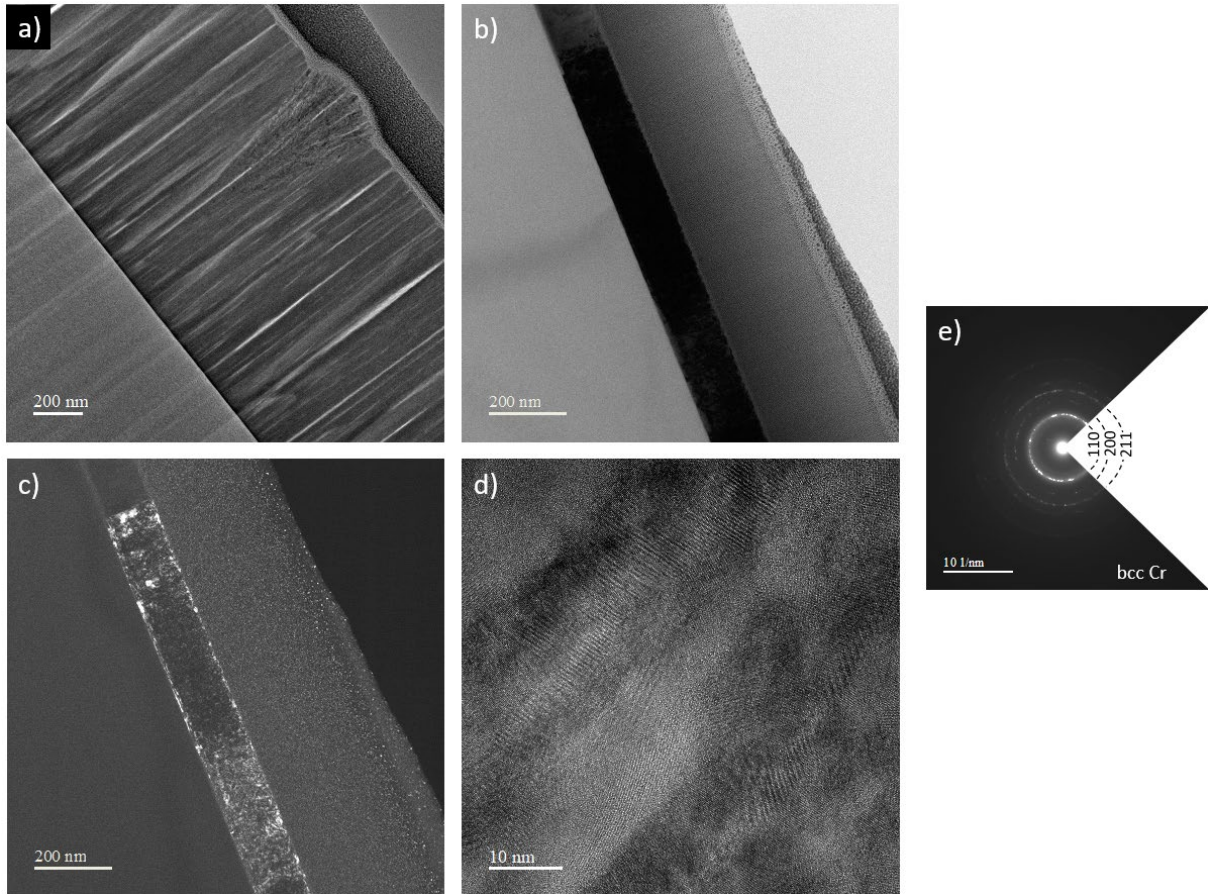
Fig. 2.8: Examples of images and patterns that can be acquired with a TEM. Image (a), bright-field image (b), dark-field image (c), high resolution image (d) and an electron diffraction pattern (e). Images (a, b) and electron diffraction pattern (e) come from a Zr-Cr thin film, while images (b, c) come from a Zr-V thin film.

A typical TEM image is shown in Fig. 2.8 (a), and in Fig. 2.8 (b, c) are shown a TEM bright-field (BF) and TEM dark-field (DF) image, respectively. To acquire a TEM BF image, the transmitted electron beam is selected with the aperture, while the scattered electrons are blocked. Thus, darker areas on these images are crystalline or denser materials. To obtain a TEM DF image, this time the transmitted beam is blocked and one scattered beam is selected, which makes the zones with no material appear darker, increasing the contrast with the material. High resolution TEM (HRTEM) images can also be obtained, and an example is shown in Fig. 2.8 (d). When operating in diffraction mode, an electron diffraction pattern of the analyzed

zone is obtained, and an example is shown in Fig. 2.8 (e). The obtained pattern depends on the material and its crystallinity. With this pattern, one would know if a sample is monocrystalline, polycrystalline or amorphous, and determine the crystalline lattice.

The TEM could also be operated in scanning-TEM (STEM) mode, in which the beam scans the whole sample as is done in SEM, except here the beam is transmitted. STEM mode was used to obtain the crystallographic orientation images in this work. To obtain these, the electron diffraction pattern in each point on the STEM image is recorded, and processed to extract the crystallographic orientation of each point in the sample.

For this study, the TEM analyzes were performed with a cold FEG JEOL ARM200 microscope with 2 Cs correctors. Before being put in the TEM, processing of thin lamellae of the samples was needed. This has been done using a focused ion beam (FIB) SEM dual beam system FEI HELIOS 600.

2.2.4   Atomic force microscopy (AFM)

AFM has been used in this work to quantify surface parameters. These include the root mean square roughness (RMS), the surface area of the samples and the height distribution of the film surface. In this technique, a sharp 10 nm tip scans the sample surface, and the interatomic forces between the tip and the sample surface induce the movement of a cantilever. This movement is proportional to the change of the surface morphology, thus allowing the obtention of high-resolution 3D images of the surface topography. The AFM principle is shown in Fig. 2.9 (a), and examples of images obtained via this technique are shown in Fig. 2.9 (b, c).
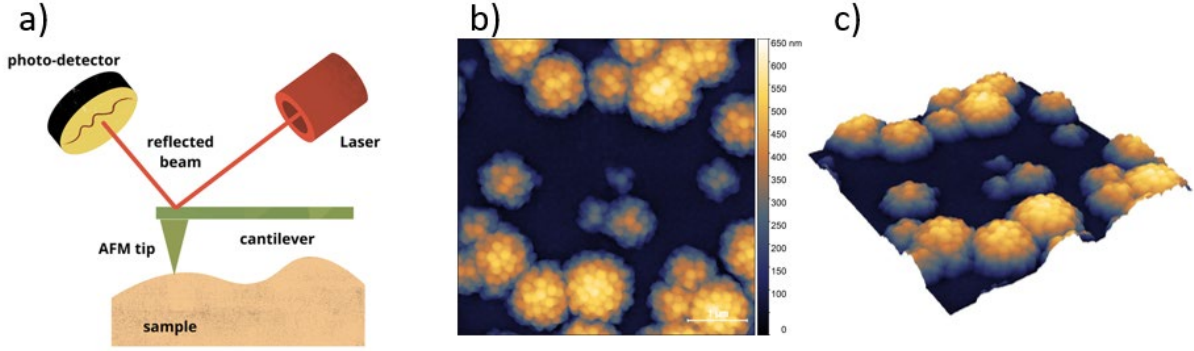
Fig. 2.9: AFM principle (a) and images of the surface topography of a Zr-V sample obtained with this technique (b), (c).

For this study, the topography of the films was examined using a NX10 Atomic Force Microscope developed by Park Systems and operating in non-contact mode.

2.2.5 In situ stress measurement

The method used for in situ stress measurement during deposition is the wafer curvature. Basically, the stress in the thin film induces a curvature of the substrate that is measured and related to the stress in the film. To do so, a multiple beam optical stress sensor is used. A laser beam is split into an array of parallel beams, and the curvature of the surface of the sample deflects the array of beams arriving to the detector. The curvature is then related to stress in the thin film with the Stoney equation that relates the measured curvature (κ) with the average stress in the film ($\bar{\sigma}$):

$$\kappa = \frac{6\bar{\sigma}h_f}{M_s h_s^2} \tag{2.3}$$

Where h_f and h_s are respectively the thicknesses of the film and the substrate, and M_s the biaxial modulus of the substrate. The product $\bar{\sigma}h_f$ is called the stress-thickness with units [N.m^{-1}] and it is usually this product that is plotted against the film thickness. The average stress here is assumed to be laterally uniform, thus ignoring any effect that could cause nonuniform

stress on the surface (grain boundaries, dual-phase films, surface texture, …). The schematic representation of this technique is shown in Fig. 2.10.
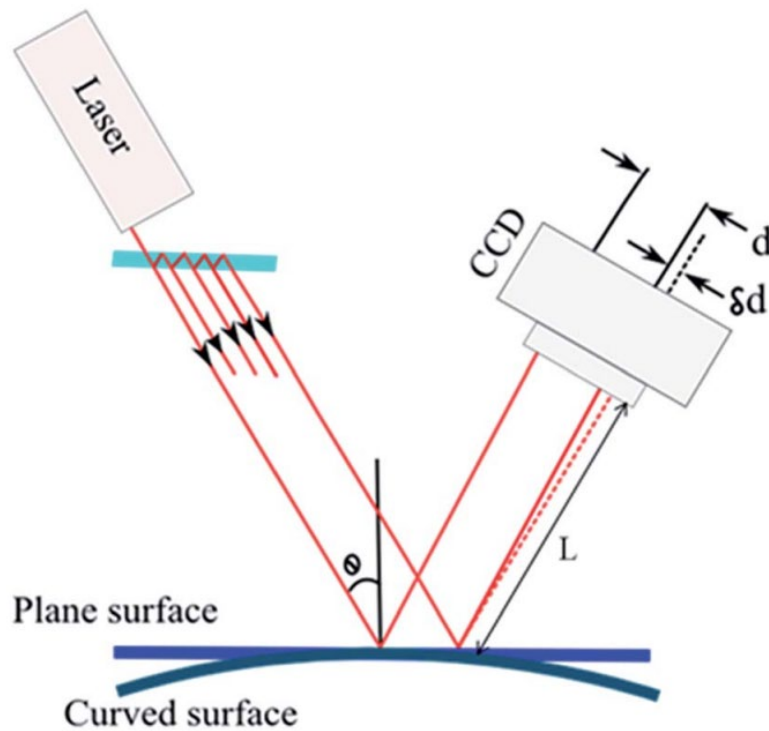
Fig. 2.10: Schematic representation of the in situ stress measurement during thin film growth using a multiple beam optical stress sensor (MOSS).

In this work, a MOSS developed by k-Space Associates has been used for the in situ substrate curvature measurements.

2.2.6 Image processing

Image processing is the use of an algorithm to process images. For this study, 2 different softwares have been used for this purpose. The first one is called ImageJ and has been used to determine the cone angle for all the samples, and the radius of the crystallites inside the crystalline cones. In Fig. 2.11 is shown the user interface of this software, along with the determination process for the angle of a crystalline cone.
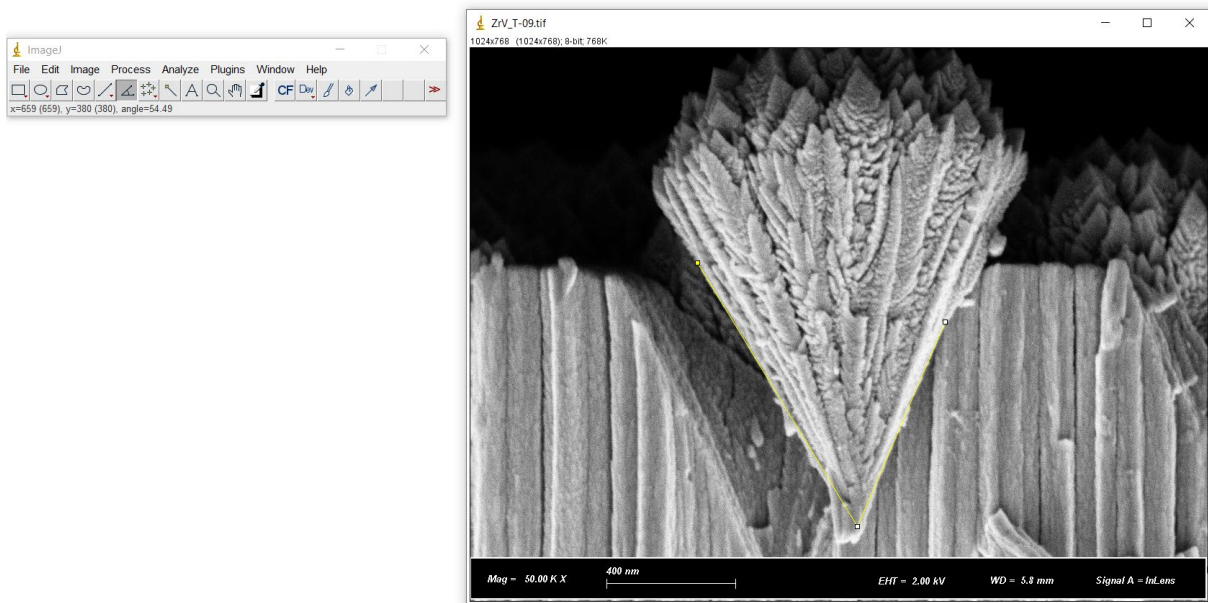
Fig. 2.11: User interface of the ImageJ software, and determination of the angle of a crystalline cone in a Zr-V thin film (yellow lines on the image).

The second software used for the purpose of image processing is MATLAB. The MATLAB software is a multi-paradigm programming language which allows use and visualization of data, and can be used to program an image analysis algorithm. For the purpose of this study, a MATLAB program has been programmed and it allows the extraction of various information from a SEM (surface or cross-section) micrograph or an AFM image; from each image type are extracted different data.

First and foremost, from a surface SEM micrograph can be extracted the surface coverage by the crystalline phase i.e. the percentage of the surface of the film covered by the crystalline phase. Also, the number and radii of the crystalline cones on the surface can be extracted, but this information should be taken with caution, as the accuracy will depend on the crystalline phase surface coverage, since the algorithm will have trouble dissociating the different cones from the image. In Fig. 2.12 is shown the result of an analysis when a Zr-V surface SEM micrograph (Fig. 2.12 (a)) is used as input. The algorithm cuts the caption, binarizes the image, gathers the white zones (which correspond to the crystalline cones). This

gathering is necessary as the white intensity of the pixels is not consistent on the surface of the cones, which could result in holes in all the cones. After this process, the image shown in Fig. 2.12 (b) is obtained. Then, the ratio of the number of white pixels divided by the total number of pixels gives the surface coverage by the crystalline phase. For the calculation of the number and radii of the cones, the algorithm knows the magnification of the SEM micrograph and is able to separate the cones with a watershed feature. The automated cone separation is shown in Fig. 2.12 (c), where each detected cone is circled in red. The information on each individual cone can be extracted, and it gives the number of the cones, as well as their radii on the surface, which can then be plotted as is seen in Fig. 2.12 (d).
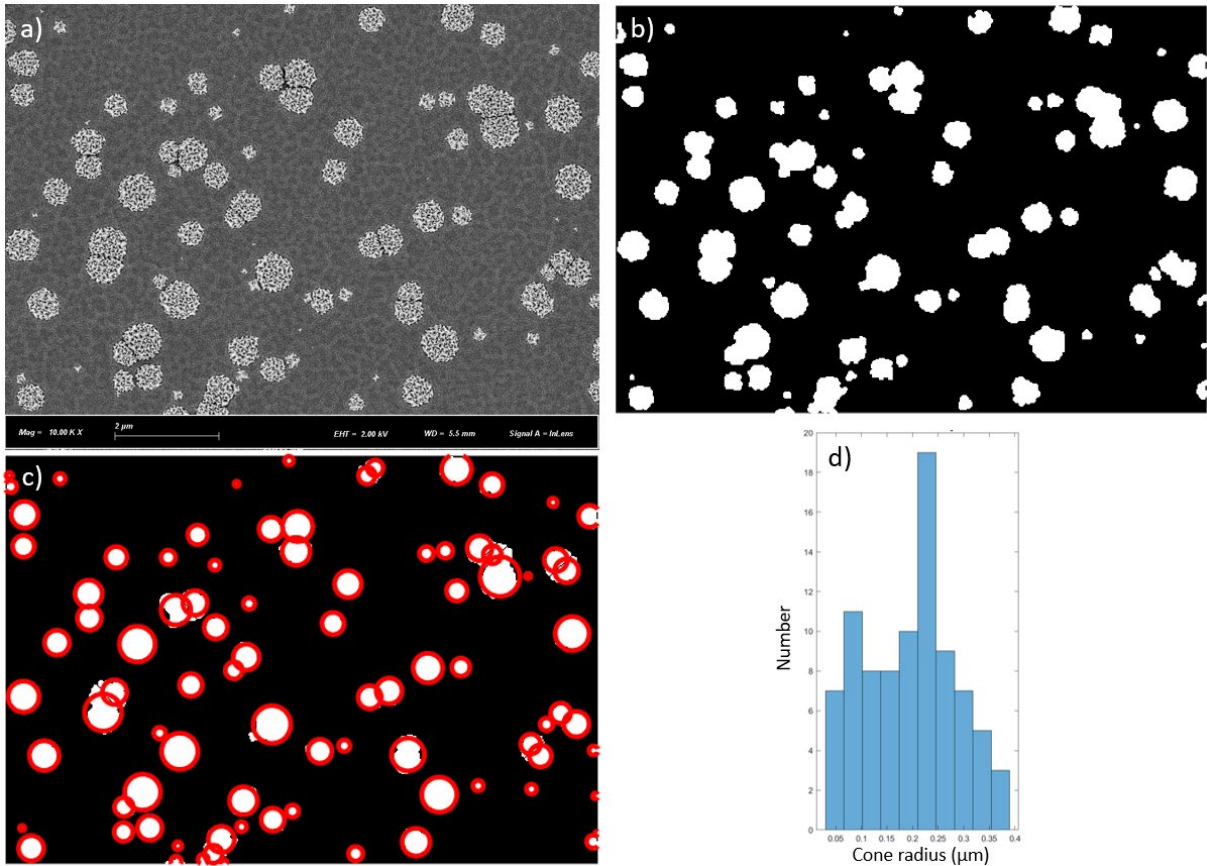
Fig. 2.12: Image treatment process for the quantitative result on the surface coverage with surface SEM micrographs. The input Zr-V surface SEM micrograph is shown on (a), and the binarized output is shown on (b). The detected cones are circled in red on (c), and the histogram of the cone radius distribution is shown on (d).

The main drawback of this analysis is that the results give indication for the thickness of the film, and not all films have the exact same thickness, which limits the comparison between them. To overcome this issue, cross-section SEM micrographs can be used as inputs. When doing so, the user defines the substrate-film interface and the crystalline zones, and the algorithm can separate the two phases. Then, as the algorithm knows the magnification of the micrograph, it is able to calculate the surface coverage by the crystalline phase by calculating the ratio of black pixels at the desired thickness divided by the horizontal number of pixels of the image. Fig. 2.13 shows the input (a) and the output of the analysis (b).
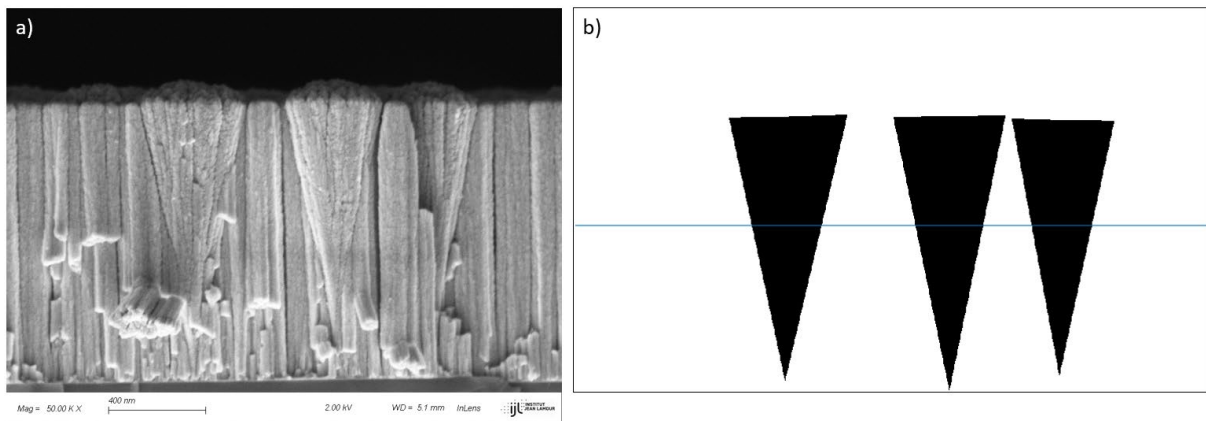
Fig. 2.13: Image treatment process for the quantitative result on the surface coverage at a given thickness with cross-section SEM micrographs. The input Zr-Cr cross-section SEM micrograph is shown on (a) and the output used for the surface coverage calculation is shown on (b).

With this cross-section analysis, as the results of the surface coverage by the crystalline phase for any desired thickness can be extracted, the comparison between samples is easier.

2.2.7 Antibacterial characterizations

The wet plating test was used to characterize the bactericidal properties of our samples surface. This test consists in the exposure of a surface to a solution containing bacteria and counting the surviving bacteria after a given exposure time.

Two different bacteria cultures have been used in this work, a Gram-negative and a Gram-positive. The Gram-negative bacteria culture was grown with the following protocol. E. Coli K12 WT (BW25113) was cultured by aerobic growth for 18h in a Lysogeny broth (LB) medium at 37°C with a shaking speed of 220rpm. 5mL culture medium was then centrifugated for 15min at 4300rpm, and the stationary cells were collected. Then, three washing steps with phosphate buffer solution (PBS) involving the same centrifugation parameters followed. The bacteria testing solution was obtained by resuspension in 5mL of PBS. The initial average cell count following this process averages at $1.37.10^9$ CFU.mL^{-1}. The bacteria were provided by the Helmholtz Center of Infection Research and stored at 4°C.

For the Gram-positive bacteria culture, B. Subtilis (DSM 10) was grown following the same protocol, but using Mueller Hinton Broth 2 (MHB2) medium. The initial average cell count averages at $5.43.10^8$ CFU.mL^{-1}. The bacteria were provided by the Helmholtz Institute for Pharmaceutical Research Saarland directly as the bacteria culture.

Following the wet plating method, three droplets of 40mL of bacteria testing solution were placed on the sample in a water saturated environment. After individual exposure times (30min, 60min, 120min), two doses of 5μL each were withdrawn. One of these is diluted in 495μL of PBS to achieve a 10^{-2} dilution (this step can be repeated with the new solution up to a 10^{-6} dilution), and the other is used for ICP-MS as detailed later. 100μL of the diluted solution are then plated on LB agar plates and incubated at 37°C and 80% moisture. Three days later, the remaining colony forming units (CFU) can be counted on the agar plate, as shown in Fig. 2.14. Both bacteria have been plated on LB agar plates. The dilution has to be chosen

carefully, if there is too much CFU on the plate it is not possible to count them, whereas if too diluted there can be no CFU on the plate. After counting, knowing the dilution before plating gives the number of bacteria that survived after the exposure time on the surface assuming that each of the bacteria has led to the growth of a CFU. Fig. 2.15 shows the wet plating test and the dilution steps for both plating and ICP-MS measurements.
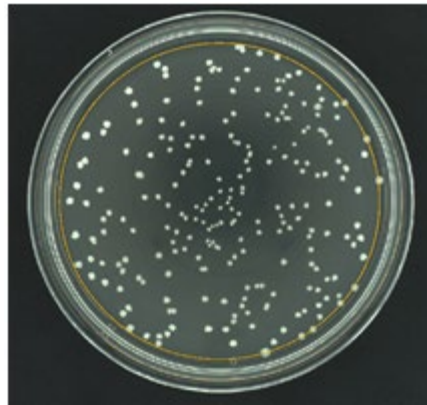
Fig. 2.14: A LB agar plate with the countable CFUs after a wet plating test. Each dot is a CFU that has grown during the incubation period.
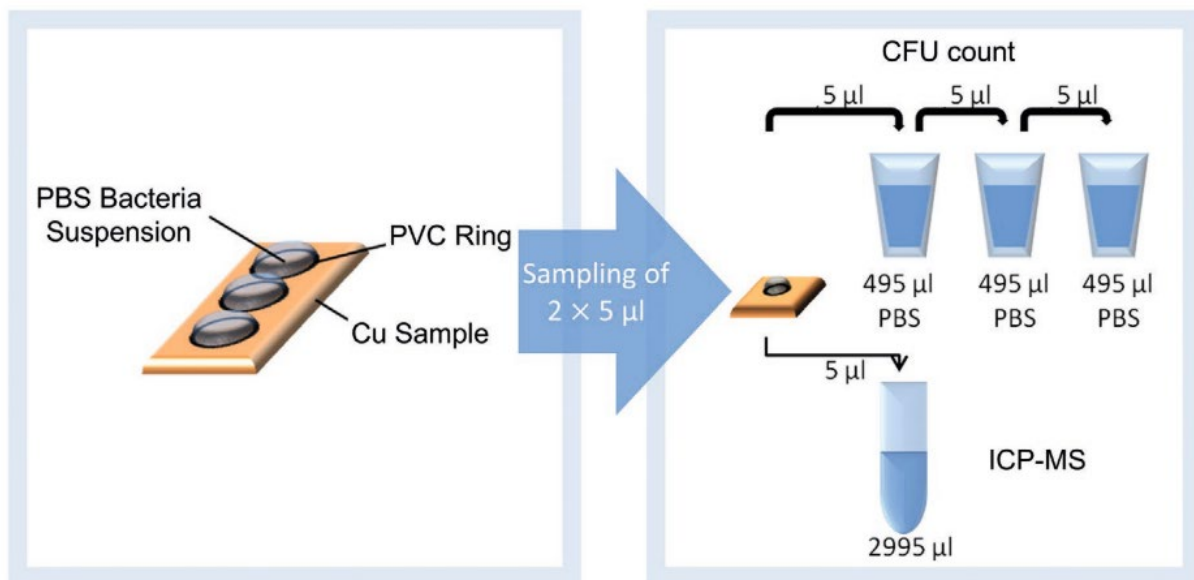
Fig. 2.15: Graphical abstract of the steps followed for the bacteria culture and the wet plating test.

When using this technique, two drawbacks have to be considered, as they lead this technique to count fewer bacteria than actual survivors. The first drawback is that only the cultivable bacteria can be counted, as the bacteria with a suppressed reproduction ability are not able to form a colony and thus, will not be countable [115]. The other drawback is that the bacteria that adhered irreversibly to the surface during the test (see Section 1.3.4 for bacterial adhesion) will not be counted. This happens because when an irreversible adhesion between a bacterium and a surface occurs, the repeated pipetting performed during this test does not provide enough force to detach them [116]. Thus, they will not be counted in the final plated solution.

To obtain the average values and the standard deviations that will be presented later, two independent experiments have been conducted.

The amount of copper ions released from each sample surface during wet plating was measured by inductively coupled plasma mass spectrometry (ICP-MS). In this technique, ICP is used to transform the substances from particles to positively charged ions. These ions are then transferred to a mass spectrometer, where the ions are separated depending on their mass-to-charge ratio.

As explained in the last part, 5 µL of the droplet after the set time is withdrawn and diluted in 2990 µL 1 wt.% nitric acid.

Before the ICP-MS measurements of the samples, standard solutions consisting of 10 mg/L scandium and cesium, and copper solutions with 0.1, 0.5, 1, 2.5, 5, 10, 25, 50, 100, 250, 500 and 800 µg/L were used for calibration.

This technique allows the calculation of the copper ions concentration in each solution, and the average values and standard deviations were obtained by doing two independent experiments.

For this thesis, an Agilent 7500CX ICP-MS has been used.

Chapter 3

Tailoring surface morphology of dual-phase thin films by controlling nucleation and growth of the crystalline regions

ABSTRACT: Dual-phase Zr-based thin films synthesized by magnetron co-sputtering and showing competitive growth between amorphous and crystalline phases have been reported recently. In such films, the amorphous phase grows as columns, while the crystalline phase grows as separated cone-shaped crystalline regions made of nanocolumns. In this chapter, we investigate this phenomenon and propose a model for the development of the crystalline regions during thin film growth. We evidence using X-ray diffraction (XRD), scanning electron microscopy (SEM) and transmission electron microscopy (TEM), that this competitive self-separation also exists in co-sputtered Zr-Cr thin films with Cr contents of ~84-86 at.%, corresponding to the transition between the amorphous and crystalline compositions, and in the Zr-V system with V contents of ~83-89 at.%. Then, to assess the sturdiness of this phenomenon, its existence and geometrical characteristics are evaluated when varying the film composition and the deposition rate. The variation of geometrical features, such as the crystalline cone angle, the diameter and density of nanocolumns, is discussed. Is it shown that a variation in the deposition rate changes the nucleation and growth kinetics of the nanocolumns. The surface coverage by the crystalline phase at a given thickness is also calculated for each deposition rate. Moreover, comparison is made between Zr-Cr, Zr-V, Zr-Mo and Zr-W dual-phase thin films to compare their nucleation and growth kinetics.

Contents

3 Tailoring surface morphology of dual-phase thin films by controlling nucleation and growth of the crystalline regions 79

3.1 Introduction

During the last decades, interest for new functional surfaces has continuously been growing [1–3]. This is because the functionalities of surface-modified materials are manifold: antibacterial surfaces [7–9], solar cells [117], wear or corrosion protection [4–6], to name a few. Many advances in the field of thin films have been made thanks to elaboration techniques such as magnetron sputtering, allowing to inexpensively synthesize thin films at low temperatures. Among these thin films, Zr-based thin film metallic glasses (TFMGs) have been intensively investigated due to their good mechanical properties such as hardness beyond 10 GPa, improvement of fatigue resistance of 316L stainless steel, and their corrosion resistance, for instance [118–120].

Recently, a new bottom-up one step process has been reported in the literature, allowing the growth of dual-phase crystalline and amorphous binary alloys by magnetron sputtering. This dual-phase morphology has already been observed in Zr-W [13,15,38] and Zr-Mo [14].

Moreover, similar morphologies have been reported in the literature for different systems (Ti-Al [41], Ti-O [30], Al-N [40]), where it has only been mentioned without much attention given to its development. These dual-phase thin films are the result of a competitive growth between the amorphous and crystalline phases during film growth, leading to unique surface morphologies [13,14].

Even if this dual-phase morphology has been observed in different binary systems, the underlying mechanisms governing the development of competitive growth of the two phases during sputtering deposition are currently not well understood. Also, the sturdiness of the phenomenon regarding the deposition conditions is still unknown, and it is unknown if this phenomenon is present regardless of the deposition conditions, such as deposition rate, or not. This is mainly due to the facts that this phenomenon has only been first observed recently, and the composition range in which it occurs is narrow, making it difficult to observe experimentally.

In this study, we show that this phenomenon can be extended to Zr-Cr and Zr-V co-sputtered thin films. The competitive growth is tested for Zr-Cr thin films by changing the deposition rate between 3.8 and 74 nm/min to test if it can exist over a wide range of deposition rates, if the composition range in which it occurs changes, and to compare the geometrical features of the obtained crystalline regions. Finally, nucleation and growth evolutions are explored in order to explain our results and generalize our understanding of the competitive growth process in Zr-based sputtered thin films. It is shown that the angle of crystalline cones decreases when increasing the deposition rate, and that it is due to a difference in nucleation and growth kinetics of the nanocolumns inside the cones. Then, these results are compared with dual-phase Zr-V, Zr-Mo and Zr-W thin films in regard to the geometrical features of the crystalline phase.

3.2 First observation and investigation of the competitive growth for Zr-Cr and Zr-V systems

When synthesizing Zr-Cr thin films by magnetron sputtering, a composition-driven transition from amorphous to crystalline Cr(Zr) solid solutions has been reported at ~89 at.% Cr [10]. This work aims to study what happens at the transition range, and aims to search for a competitive growth between an amorphous and crystalline phases, as has been seen for other Zr-based binary systems in magnetron sputtering [13–15,38]. For this purpose, different thin films at compositions around the transition between these two phases were deposited at a 11 nm/min deposition rate. X-ray diffractograms of three of these thin films are shown in Fig. 3.1 (a), with compositions ranging from 83 to 88 at.% Cr, close to the 89 at.% Cr reported in [10]. The film with 83 at.% Cr is totally X-Ray amorphous, and the film with 88 at.% Cr is totally crystalline. However, for a composition between these two (at 85 at.% Cr), we can see a mixture of the two XRD signals, showing that the two phases coexist in the same film. The shift in diffraction angle for the (110) bcc Cr plane is due to a change in the lattice parameter. Indeed, increasing the Zr content in the Cr(Zr) solid solution increases the lattice parameter as Zr has an atomic radius larger than that of Cr which are respectively 2.69 Å and 2.33 Å [121], thus making the peak to shift towards lower diffraction angles.

The same thin films have been characterized with SEM, and their surface micrographs are shown in Fig. 3.1 (b-d). As can be seen, the amorphous and crystalline films present different surface morphologies. At the composition of the transition, however, two different regions can be observed, an amorphous and a crystalline, separated by an interface. According to previous works [13–15,38], the crystalline region is in the form of disks on the surface, surrounded by an amorphous matrix. From this micrograph, it is also noticeable that, at some point during deposition, the crystalline regions coalesce. A cross-section SEM micrograph,

Fig. 3.1 (e), shows that the amorphous phase grows in a columnar microstructure, while the crystalline phase grows as cones, with a spherical cap on the surface. These cones do not nucleate from the beginning of deposition, but after a certain thickness, and the origin of each cone is not at the same thickness. This explains why the area of each cone emerging at the surface is different. Indeed, the surface of the crystalline region on the surface depends on the thickness where the cone nucleates, because the larger the cone, the larger its surface area. The obtained microstructure for Zr-Cr thin films is the same as what has been observed in the other Zr-based systems. Moreover, the cone angle is nearly the same whatever its nucleation thickness.
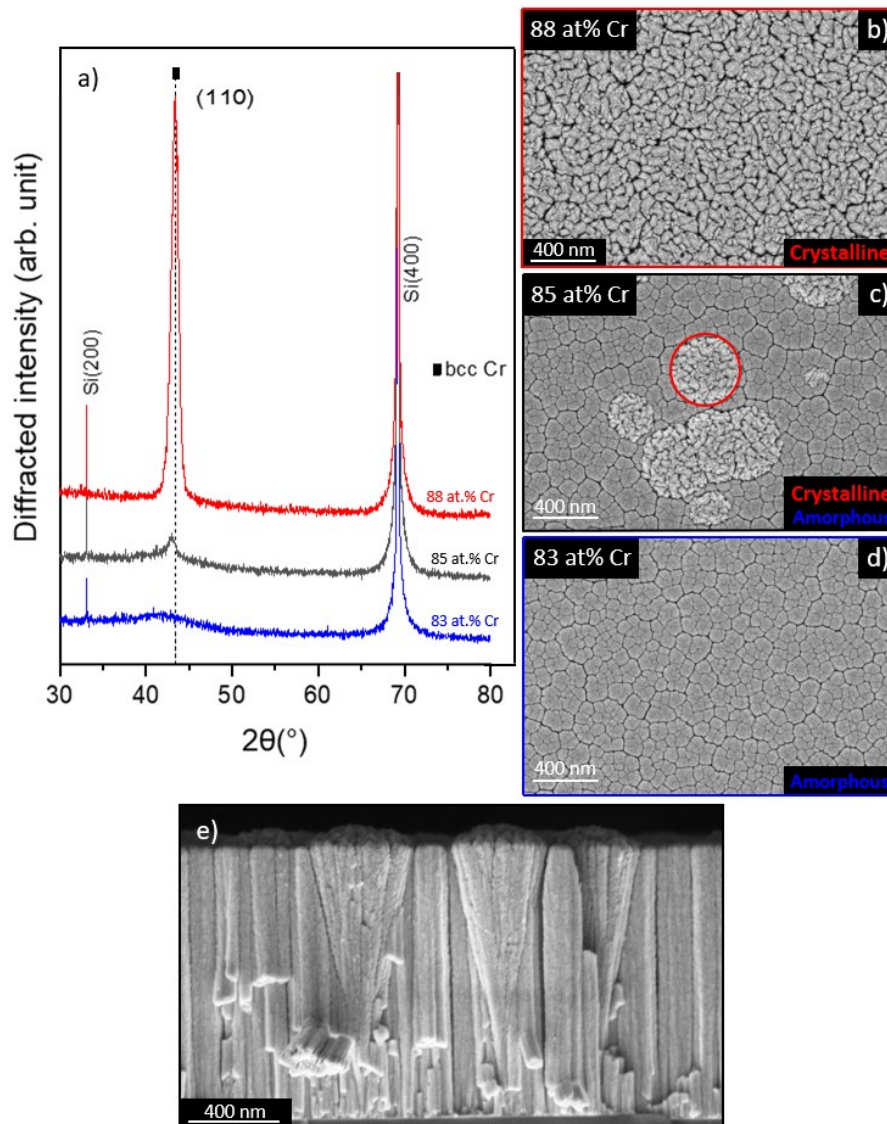
Fig. 3.1: (a) X-ray diffractograms of Zr-Cr thin films with 83 at.% Cr (blue), 85 at.% Cr (black), and 88 at.% Cr (red). (b-d) Surface SEM micrographs showing crystalline (b), dual-phase (c) and amorphous (d) surface morphologies, corresponding to the X-ray diffractograms on the left. (e) Cross-section SEM micrographs showing the dual-phase sample, with amorphous columns and crystalline cones terminated by a dome on the surface.

The same competitive growth between amorphous and crystalline phases has been observed in the Zr-V system, with a similar morphology for these two phases as what was observed for Zr-Cr thin films. Their surface and cross-section SEM micrographs are shown in

Fig. 3.2 (a-c). The amorphous phase shows the exact same morphology as in the other systems, as can be observed in Fig. 3.2 (a), where a 82 at.% V thin film is shown. For a totally crystalline Zr-V thin film at a 90 at.% V composition, shown in Fig. 3.2 (c), the film consists of crystalline columns, except this time the top of the columns show tetrahedral facets, originating from the crystalline orientation of the columns. For a thin film sputtered at a chemical composition intermediate to these two, take for example a 86 at.% V thin film such as the one shown in Fig. 3.2 (b), this thin film shows amorphous columns and crystalline cones. The main difference between these crystalline cones and the ones seen in Zr-Cr films is the nanocolumn diameter, as can be seen by comparing the cross-section SEM micrographs; Zr-V nanocolumns are larger than Zr-Cr ones. The facets on their surface and the higher nanocolumn diameter could indicate a higher adatom surface mobility [24].
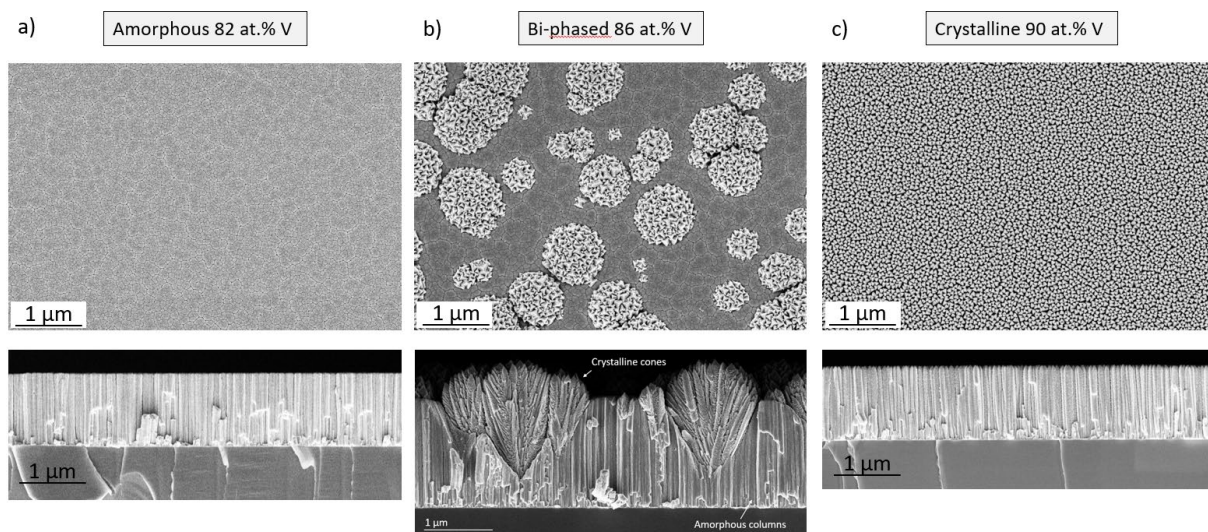
Fig. 3.2: SEM surface and cross-section micrographs of Zr-V thin films at different chemical compositions: 82 at.% V (a), 86 at.% V (b), and 90 at.% V (c).

Interestingly, the surface morphology can be tailored by changing the film thickness. Indeed, as thickness increases, the surface coverage by the crystalline phase increases, until it

eventually covers the whole surface. Moreover, changing the composition inside the transition zone can also be used to control the surface morphology [13], as the nucleation density of the crystalline cones increases with an increasing Cr content. Therefore, combining thickness and composition can help tailoring the surface of the deposited thin films. Nonetheless, the range of this competitive growth is quite narrow: less than 5 at.% Cr for Zr-Cr thin films and around 6 at.% V for Zr-V thin films, thus very careful investigations are required to observe what happens during growth and create models.

Since this is the first report of the observation of the competitive growth in the Zr-Cr and Zr-V systems, some additional characterizations have to be done. To ensure that the columns and cones are two different phases, HRTEM and electron diffraction have been conducted on the sample presented in Fig. 3.1 (c). Two HRTEM micrograph of a cone and its interface with the amorphous matrix is shown in Fig. 3.3 (a, d), and the selected area diffraction (SAED) patterns of the two phases are shown in Fig. 3.3 (b, c). These diffraction patterns confirm the crystallinity of the cones in the thin film, while the columns only present short range ordering, associated with an amorphous phase, as also observed in the HRTEM micrographs of these zones in Fig. 3.3 (e, f). The lattice fringes seen in the cone in Fig. 3.3 (e) further confirm the fact that the cones are crystalline, and the micrograph in Fig. 3.3 (f) confirms the amorphous nature of the columns. The amorphous halo of Fig. 3.3 (c) presents a radius that is in agreement with that of (110) bcc Cr shown in Fig. 3.3 (b). Therefore, we can argue that the local bcc Cr order present in the amorphous columns is the precursor of the nucleation of crystalline regions.
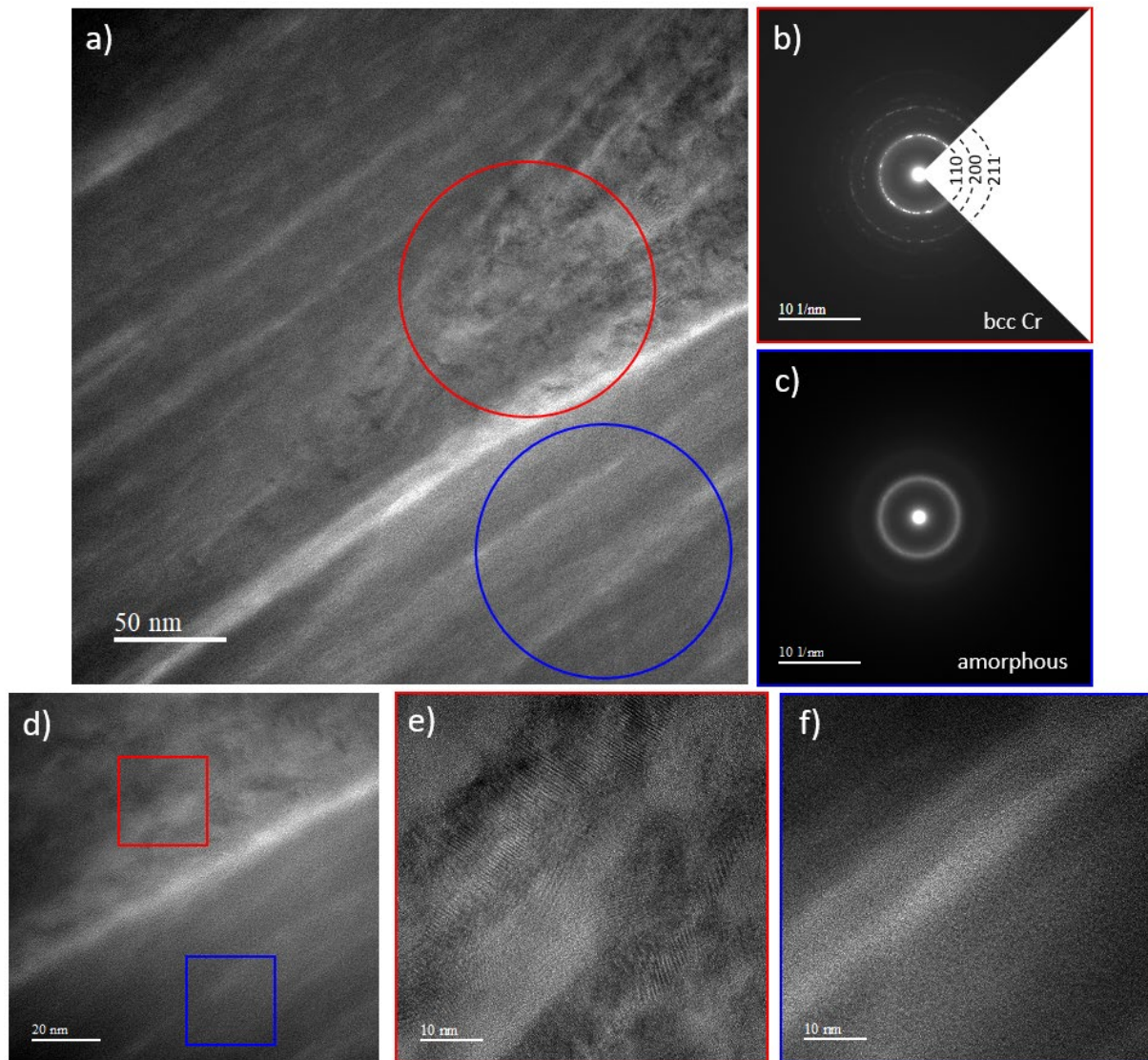
Fig. 3.3: HRTEM micrograph of a 86 at.% V (a) showing the interface between a cone (in the middle) and a column (surrounding the cone), and (b) and (c) the selected area diffraction (SAED) patterns of the zones highlighted in (a). HRTEM micrographs of the same interface (d), the cone (e) and the columns (f).

The synthesized Zr-V thin films have undergone the same characterizations, and the results of the TEM characterizations are shown in Fig. 3.4. As can be seen from Fig. 3.4 (c, d), the cones are also crystalline as confirmed by the lattice fringes on the HRTEM micrograph and the electron diffraction patterns and X-ray diffractograms (not shown). The crystalline

phase in these films is bcc V. The cones are also embedded in an amorphous matrix, only this time are observed a few nanocrystalline domains in the amorphous matrix, which did not grow as cones but were finally overgrown by the amorphous phase. This can be observed on Fig. 3.4 (a), where these regions diffract inside the amorphous matrix. The observation of nanocrystallites embedded in the amorphous matrix has already been reported for Si:H [122] and TiO$_2$ thin films [123], where the density of embedded crystalline domains is proportional to the density of columns. The authors state that some crystalline domains are covered by amorphous matter or other grains and thus do not grow as cones [123].
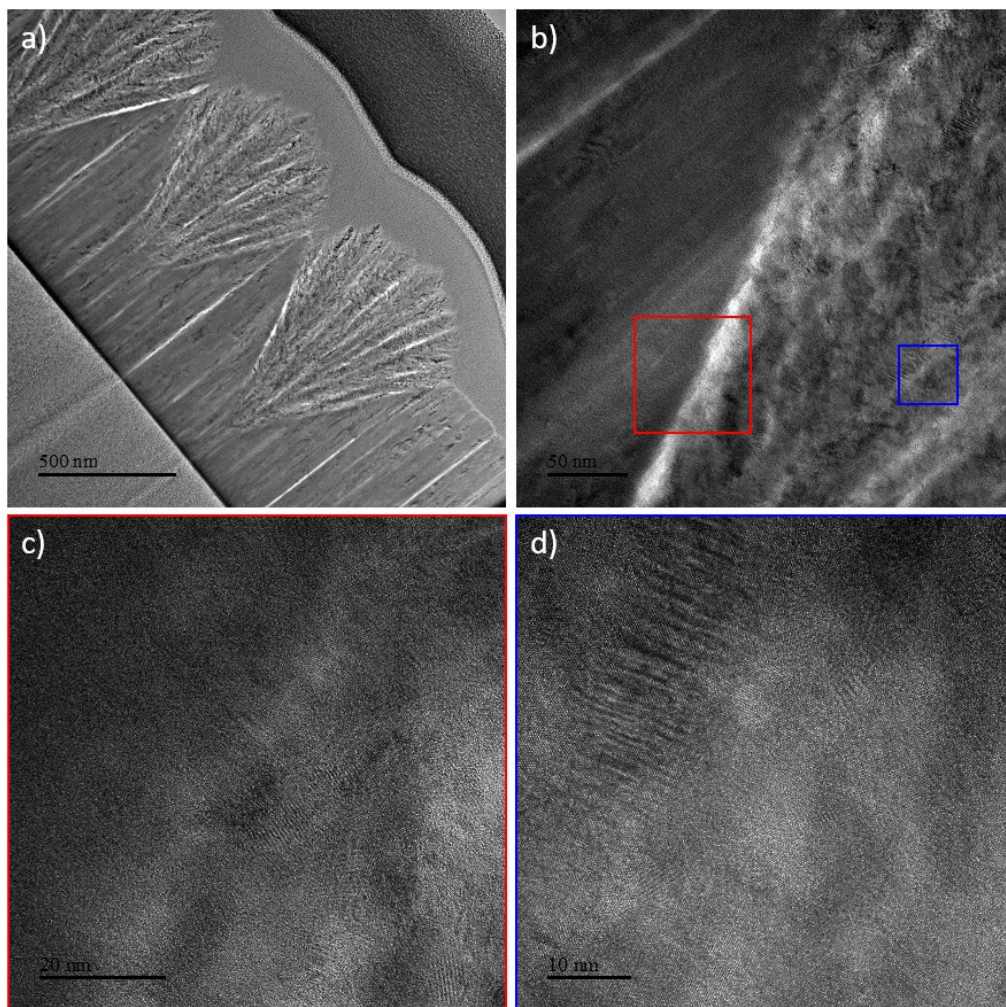
Fig. 3.4: TEM micrograph of a synthesized 86 at.% V Zr-V thin film (a). HRTEM micrographs of the interface between a crystalline cone and the amorphous matrix (b, c) and of a crystalline cone (d).

To further understand how the competitive growth develops and can be manipulated, the deposition rate of the Zr-Cr thin films has been varied in the range 5-63 nm/min reference deposition rates. Fig. 3.5 shows the surface coverage by the crystalline phase as a function of the film composition and for various deposition rates. The value is measured at a 750 nm thickness for all the films, to account for the fact that all deposited films do not have the exact same thickness. The values have been obtained thanks to our MatLab program that allows calculation of the surface coverage at a given thickness from cross-section SEM micrographs (for more information, see **Chapter 2**). Films with a 0% surface coverage are totally amorphous, while films with a 100 % surface coverage are totally crystalline at a 750 nm thickness, meaning they either are crystalline from the start of deposition or that crystalline cones overgrew the amorphous phase and covered the whole surface. The existence of the competitive growth is approximately in the range of 84 to 86 at.% Cr for all the deposited films. Yet, due to the narrow composition range to observe this competitive growth, it is difficult to conclude whether or not the deposition rate affects the transition composition range.
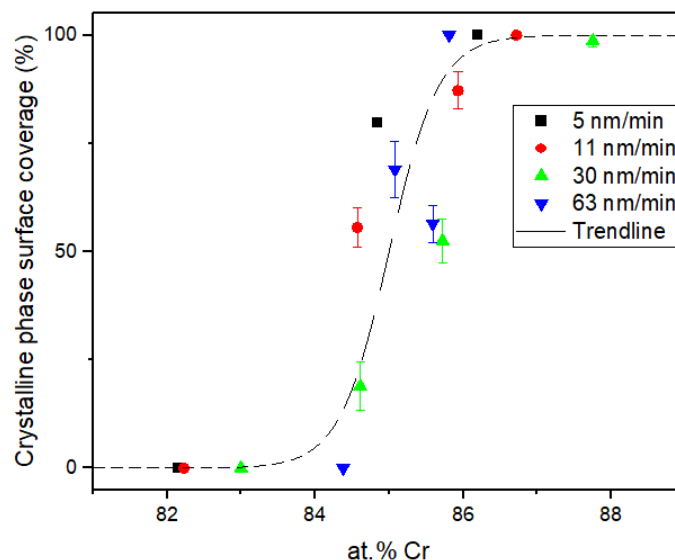
Fig. 3.5: Values of the surface coverage by the crystalline phase at 750 nm thickness, extrapolated from cross-section SEM micrographs, for each deposition rate range. Some error bars are too small to be seen.

However, it is important to note that in this wide range of reference deposition rates, from 5 to 63 nm/min, the competitive growth has always been observed, which indicates that it is a process resilient to changes in deposition conditions and is encouraging to find it in other systems. Yet, it is important to notice that the overall geometry of the structures is affected by the deposition rate, as shown in Fig. 3.6 (a-b). As can be seen, the crystalline cone angle in Zr-Cr thin films for low deposition rates, in Fig. 3.6 (a), is larger than for high deposition rates, in Fig. 3.6 (b). Hence, a reduction of the crystalline cone angle is observed when increasing the deposition rate. Furthermore, a difference is observed depending on the alloy deposited, as can be seen when comparing Zr-Cr thin films with Zr-V thin films in Fig. 3.6 (c): The crystalline cone angle is much larger for Zr-V thin films than for Zr-Cr thin films at the same deposition rate.
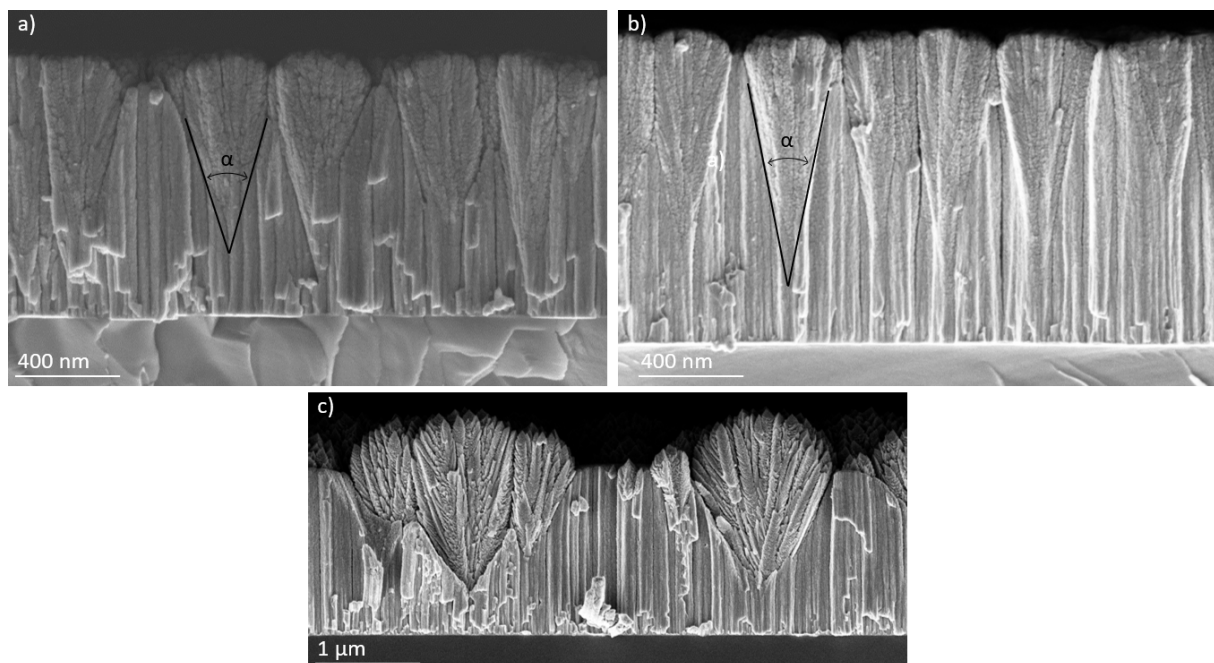
Fig. 3.6: SEM micrographs showing Zr-Cr thin films (~85 at.% Cr) deposited at 5nm/min (a), 63 nm/min (b), and a Zr-V thin film (86 at.% V) deposited at 18nm/min (c) for comparison.

3.3 Nucleation and growth of nanocolumns in the cones

For the Zr-Cr thin films, Fig. 3.7 (a) gives the crystalline cone angle as a function of deposition rate. When the deposition rate increases, the crystalline cone angle decreases from 32° to 21°. However, this decrease is quite small, given the fact that the deposition rate has been increased approximately 12-fold, from 5 nm/min up to 63 nm/min. The Zr-V thin films were deposited at a single deposition rate of 18 nm/min, resulting in the cones having an average angle of 48.4°, which is much larger than for Zr-Cr thin films. For comparison purposes, the results from the previous studies from our team on Zr-Mo and Zr-W thin films have been reported here. Zr-Mo thin film deposited at a 24 nm/min deposition rate resulted in a 39.9° cone angle, while the Zr-W thin film deposited at a 52 nm/min resulted in a 45.4° cone angle.
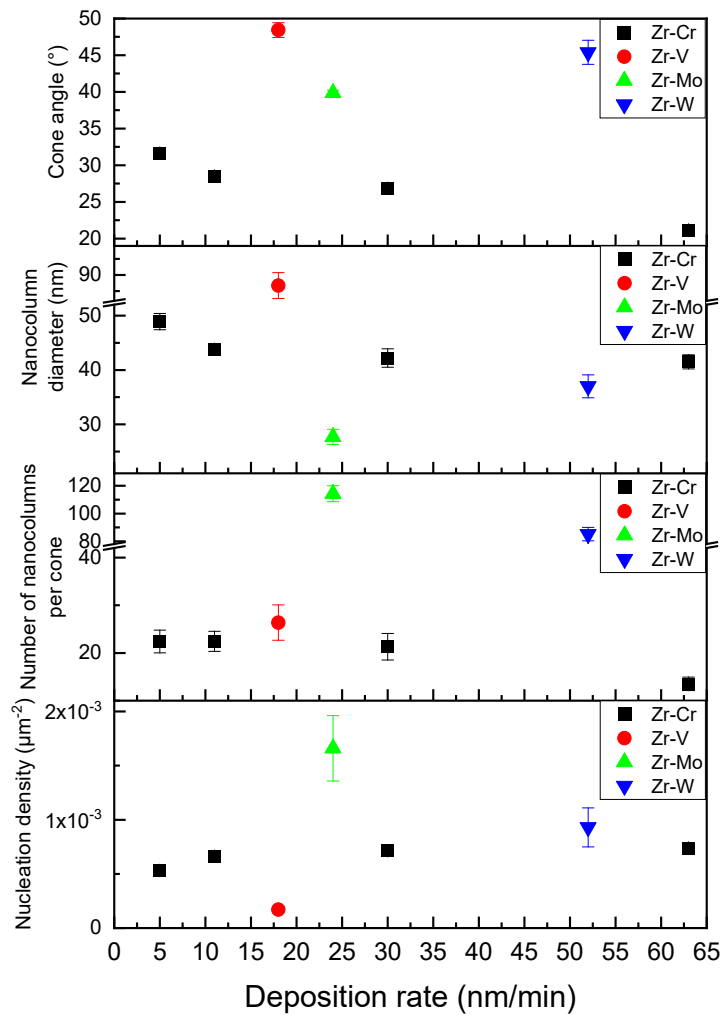
Fig. 3.7: Graphs showing the change in crystalline cone angle (a), in nanocolumn diameter (b), in number of nanocolumns per cone (c) and in nanocolumn nucleation density (d) for Zr-Cr, Zr-V, Zr-Mo and Zr-W thin films depending on the deposition rate of the thin films. Some error bars are too small to be seen.

To try to explain the difference found depending on the deposition rate, we propose a model of nucleation and growth of nanocolumns inside the crystalline cones, where there is only a small number of nanocolumns that nucleate at the apex of the cone, and the other nanocolumns nucleate at the interface between the growing nanocolumns and the amorphous

columns upon the development of the crystalline cones. The proposed model is shown in Fig. 3.8.
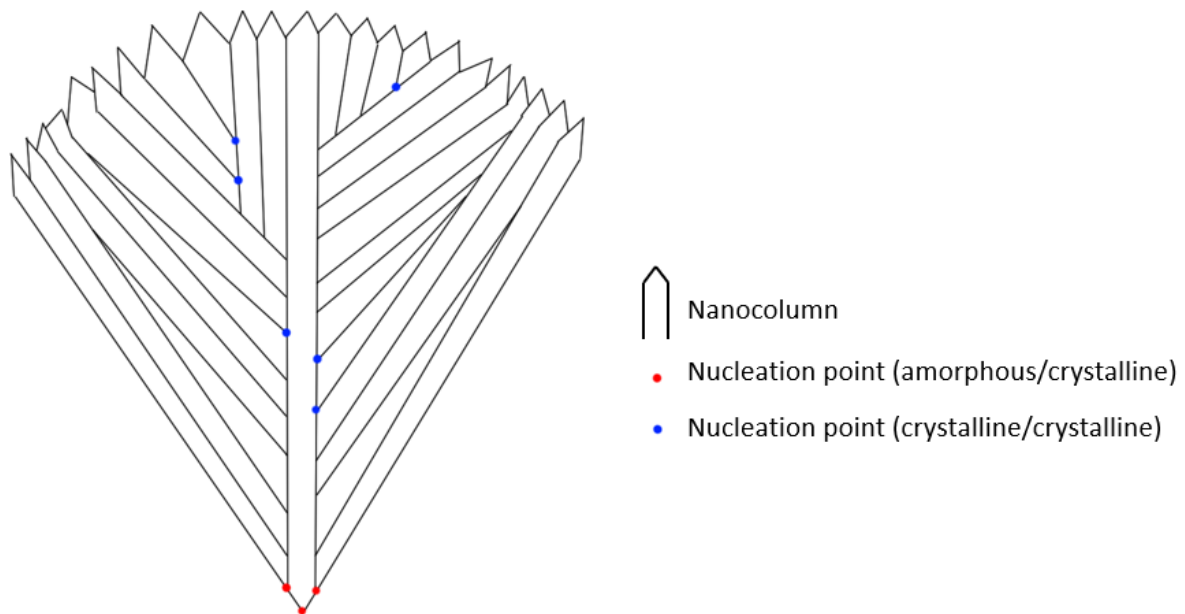
Fig. 3.8: Proposed nucleation and growth model for the crystalline cones in Zr-based thin films.

It can be seen on the SEM cross-section micrographs (Fig. 3.6) that some nanocolumns grow from the beginning of the cone, and some other nucleate at the interface between a nanocolumn and the amorphous matrix, or between nanocolumns. It is easier to observe on the Zr-V thin film, as the crystalline phase is less dense and the diameter of the nanocolumns is larger than for Zr-Cr. On Fig. 3.6 (c), on the cone on the right of the micrograph, vertical nanocolumns can be seen at the axis of the cone. In contrast, higher in the cones, some nanocolumns show a higher inclination angle indicating that they nucleated higher in the cone between different nanocolumns.

Using this model, the change in crystalline cone angle with deposition rate might find its origin either in a difference in nucleation rate of the nanocolumns inside the cones, a difference in their growth kinetics, or both.

The first explanation for the decrease of the crystalline cones angle with increasing deposition rate is the surface diffusion of adatoms. Indeed, an increased deposition rate means a reduced diffusion time for the adatoms before they get buried by the next layer of incoming atoms, and thus less in-plane growth of the crystalline cones, reducing the cone angle. Nevertheless, given the high increase in deposition rate, the in-plane growth rate would need to be 8 times higher if the diffusion was the only parameter affecting the cone angle, following the equation given by Borroto et al. [13]:

$$\frac{V_G}{V_0} = \tan\left(\frac{\alpha}{2}\right) \qquad (3.1)$$

With V_G the in-plane growth rate, V_0 the deposition rate, and α the crystalline cone angle, as shown in Fig. 3.6.

Hence, changing the deposition rate affects the in-plane growth of the nanocolumns. This is confirmed in Fig. 3.7 (b), where a ~15 % decrease in nanocolumn diameter is observed when increasing the deposition rate from 5 to 63nm/min, due to the fact that the adatoms have less time to diffuse on the surface of the film when the deposition rate is higher, and that means less in-plane growth for the nanocolumns.

However, this ~15 % decrease in nanocolumn diameter alone does not explain the ~30 % decrease in cone angle. According to our model, it means that there could be another phenomenon happening, such as a difference in nucleation rate of the nanocolumns inside the cones. Thus, if this model of nucleation and growth of the crystalline phase is correct, a decrease of the nucleation rate should be observed when increasing the deposition rate.

3.4 Possible origins of the differences between systems

To quantify the difference in nucleation inside the cones, the number of nanocolumns in a cone must be known. Yet, two problems arise when counting the number of nanocolumns per cone. The first is due to the density of the nanocolumns in the cones, making it difficult to count them. Some interfaces can be easily seen, and have been used to calculate the average nanocolumn diameter for each deposition rate range, but it is not the case for the vast majority of the nanocolumns, where it becomes difficult to see the separation. The second problem is that when observing a cross-section SEM micrograph, the cones are not always cut in their center, and it is of great difficulty to know exactly where a cone has been cut, which means counting the nanocolumns from SEM micrographs is misleading.

To overcome these issues, the average number of nanocolumns per cone will be calculated by dividing the average cone volume by the average nanocolumn volume. To calculate the first one, the volume is calculated by using the cone angle and setting their height to 500 nm, which means for cones that have not already coalesced. For the latter, the nanocolumn is assumed to be a cylinder, of radius half of the nanocolumn diameter shown in Fig. 3.7 (b), and of length half of the 500 nm height used for the cone, as all nanocolumns do not nucleate at the origin of the cone. Then, neglecting the influence of porosity, the average cone volume is divided by the average nanocolumn volume, giving the plot in Fig. 3.7 (c).

It should be noted that this calculation gives the same results no matter the length of the nanocolumns as compared to the cone height. As can be seen in Fig. 3.7, when increasing the deposition rate from 5 up to 30 nm/min, the decrease in crystalline cone angle is mostly due to the reduction of the nanocolumn diameter, and the nucleation density does not significantly change. Hence, at these deposition rates, the change in crystalline cone angle is mostly governed by the diffusion of the adatoms on the surface of the film during growth, whereas increasing

the deposition rate from 30 to 63 nm/min did not significantly change the nanocolumn diameter. Instead, the number of nanocolumns per cone decreased by nearly 40 % as compared to other deposition rates, which means that the decrease in crystalline cone angle for very high deposition rates is mostly due to a lower nucleation density of the nanocolumns in the cones.

As a comparison, for the Zr-V thin films, as can be seen in Fig. 3.7 (a), the crystalline cone angle is much higher than that of Zr-Cr thin films, being 48° and from 21° to 32°, respectively. Moreover, it can be seen in Fig. 3.7 (b) that the nanocolumn diameter is 87 nm, approximately 2 times higher than that of Zr-Cr films, and the number of nanocolumns per cone is nearly the same as for Zr-Cr thin films as Fig. 3.7 (c) shows. On the other hand, Zr-Mo and Zr-W with their respective 40° and 45° cone angles also show a higher cone angle than Zr-Cr ones, but for these the difference comes from a higher nucleation density of nanocolumns in the cones rather than larger nanocolumns, as can be seen in Fig 3.7 (c).

A first approach to explain the differences in nanocolumn diameter between the studied alloys is that the nanocolumn diameter depends on both the surface diffusion coefficient and the diffusion time. However, difficulties arise when pursuing this approach: the surface diffusion coefficient and the surface temperature are unknown, and so is the diffusion time. The model used here to estimate these parameters is presented in Fig. 3.9. In this model, the atoms from the metallic vapor condensates in a liquid-like layer, and that layer then solidifies and forms the film [124]. The surface temperature is supposed to be the boiling point of the alloy, and the temperature of the interface between the liquid-like layer and the growing film is the crystallization temperature of the alloy. With this model, an increase in the interval between these two temperatures would mean an increased diffusion time. The boiling point of the alloys has been obtained via a mixing law on the boiling points of the pure elements at atmospheric pressure; while lowering the pressure decreases the boiling point of metals, this effect is neglected here [125]. The crystallization temperature is not obtained through the phase

diagrams, as during sputtering the liquid-like layer and the solid film have the same composition. Instead, the crystallization temperature has been obtained using ThermoCalc, a stable equilibrium calculation software. This allows the calculation of the Gibbs free energy of the liquid and solid phases at the deposition pressure and alloy chemical composition. The crystallization temperature of the alloy is then extracted as the crossing point between the two Gibbs free energy curves.
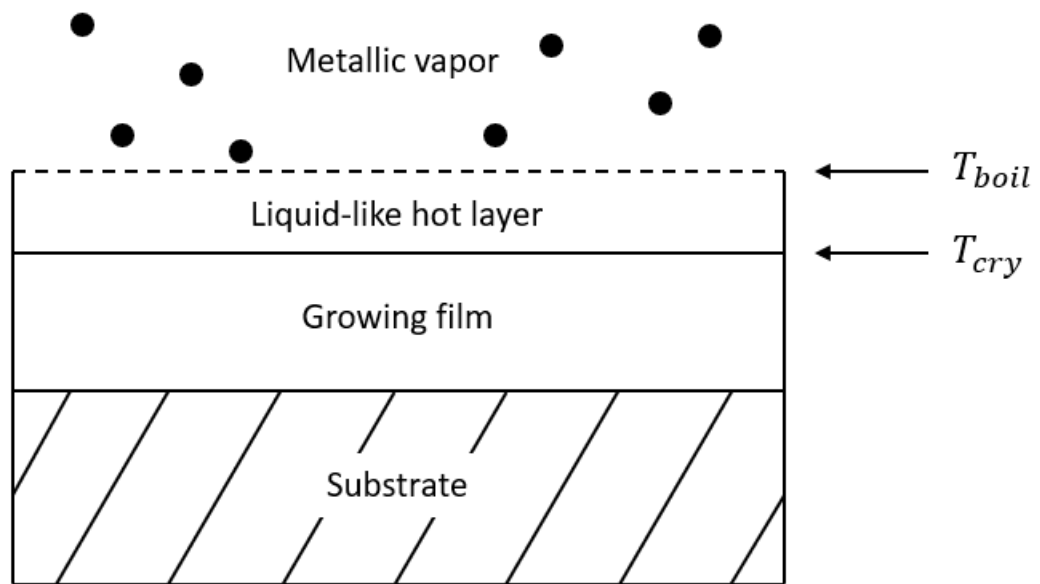
Fig. 3.9: Schematic of the formation of a growing film. The metallic vapor condensates in a liquid-like hot layer that then forms the film. Adapted from Ref. [124].

With these information, we can now calculate the temperature interval of the liquid-like layer for each alloy, and the results are shown in Table 3.1. As can be observed, there is no correlation between this interval and the nanocolumn diameter, thus invalidating this approach.

Table 3.1: Nanocolumn diameters of the studied alloys and the data used for the approximation of a constant proportional to the diffusion coefficient and diffusion time.

	Zr-Cr (85 at.% Cr)	Zr-V (86 at.% V)	Zr-Mo (60 at.% Mo)	Zr-W (72 at.% W)
Nanocolumn diameter (nm)	41 - 49	87	28	37
Boiling point (K)	3200	3816	4807	5768
Crystallization temperature (K)	1898	1805	1906	2691
Liquid-like interval (K)	1302	2011	2901	3077
$\alpha\, D_s * t_{diff}$	5.10^{-3}	9.10^{-3}	7.10^{-3}	2.10^{-3}

With this approach invalidated, we must find a new way of estimating the surface diffusion coefficient and time. During sputtering, what we learned from structure zone models is that the variation in the amplitude of the surface diffusion can be approached by the variations in the ratio between the deposition temperature and the melting temperature of the material [23]. Thus, we can estimate that:

$$D_s \; \alpha \; \frac{T_{deposition}}{T_{cry}} \tag{3.2}$$

With D_s the surface diffusion coefficient and T_{cry} the crystallization temperature mentioned above. The deposition temperature can be considered constant for each film and equal to ~300 K, because the temperature increase during deposition is negligible in our case. For the diffusion time, it can be estimated that the adatom diffusion stops when the next layer of atoms is deposited. Thus the diffusion time is dictated by the deposition rate, and the diffusion time can then be estimated as:

$$t_{diff} \; \alpha \; \frac{1}{V_{deposition}} \tag{3.3}$$

With $V_{deposition}$ the deposition rate. We now have an estimation for both the surface diffusion coefficient and the diffusion time, and the results are presented in Table 3.1. This time again, the adatom surface diffusion does not seem to explain the nanocolumn diameter. From

the inability of these hypotheses to explain the nanocolumn diameter, it leads us to believe that another limiting phenomenon occurs. For instance, the nucleation density of the nanocolumns in the cones could be the determining factor, as shown in Fig. 3.7 (d). Two reasons may explain this: (1) the nanocolumns are competing against their neighbors in terms of lateral growth, and (2) as no amorphous-crystalline phase transition occurs, the amorphous columns surrounding the cones also limit the nanocolumns lateral growth. If this is the case, then the nanocolumns would grow laterally as much as they can before being restricted by the other nanocolumns, and the nanocolumn diameter then depends of the nucleation density rather than adatom surface diffusion. It has to be noted here that the envelope of the cones constituting the crystalline/amorphous interface is straight, restraining the lateral expansion of the crystalline regions.

Otherwise, it should also be noted that the diffusion of each atom on the surface is not necessarily similar, for instance the terrace diffusion barrier of each element on the surface may differ between the elements used in this study [126]. It is also possible that the different films deposited exhibit different film structure with reference to a structure zone model, resulting in different diffusion dynamics between our alloys [23].

3.5 Chapter conclusions

To summarize, the competitive growth phenomenon that occurs between amorphous and crystalline phases that has been observed in the literature for sputtered Zr-Mo and Zr-W thin films has been also found in the Zr-Cr and Zr-V systems. This study shows that it exists in a wide range of deposition rate, indicating its resilience against changes of deposition conditions and giving promises for its experimental observation in other systems. Moreover, changing the deposition rate also changes the geometrical features of the crystalline phase such as the cone

angle, and can be used as a new parameter to control the growth of the film, together with the film composition and film thickness. The diameter and density of nanocolumns inside a cone also depend on the deposition rate and the material deposited. Furthermore, we proposed a model of nucleation and growth for the nanocolumns inside the crystalline cones to explain the development of this competitive growth, which is a step towards the understanding of the mechanisms underlying this process. As the diffusion model alone could not explain the nanocolumn diameter difference between the alloys, we proposed that the nanocolumn nucleation density could be the predominant parameter for the lateral growth of the nanocolumns.

Chapter 4

Improvement of surface antibacterial properties: the cases of dual-phase Zr-V thin films and Cu-coated dual-phase Zr-V thin films

ABSTRACT: In this chapter, the antibacterial efficiency of dual-phase Zr-V thin films and copper-coated dual-phase Zr-V thin films will be assessed. First, the reasons behind the choice of Zr-V for the antibacterial applications are explained, and the structure of these films and the copper coating are presented. Then, we show the results of the wet plating tests, that evaluate the survivability of bacteria on the surfaces of our thin films. Here, E. Coli and B. Subtilis have been used as bacteria representative from the Gram-negative and Gram-positive bacteria, respectively. The results are correlated with the surface morphology of the thin films and their copper ion release during the wet plating test.

Contents

4.1 Introduction

As a result of the decreasing effectiveness of the antibiotics against bacteria, new strategies have to be sought to ensure safety in hospitals and public spaces. Many approaches are currently tested and show promising results for the future, such as bacteriophage therapy [56], antibacterial peptides [111], mechanical bacterial cell rupture [112,113], antiadhesive surfaces or bactericidal surfaces [7,83]. Concerning the latter, Cu and Ag have been shown to significantly reduce the viability of bacteria on their surface, thus potentially avoiding the spread of infectious diseases from surfaces [89].

In **Chapter 3**, we showed that the competitive growth between the crystalline and amorphous phases that has been reported in Zr-Mo and Zr-W thin films also occurs in Zr-Cr and Zr-V thin films. The result is thin films with tailorable surface features and potentially high developed surface areas, which leads us to consider them to be promising for antibacterial applications. These thin films showing similar topography, the most promising of them will be chosen for the wet plating test, a test used to characterize bacterial viability on surfaces.

To do so, a copper coating will be sputtered on top of our thin films to benefit from its intrinsic bactericidal properties. These thin films have the potential to kill bacteria via copper ion release, by mechanical rupture of the cell walls thanks to the nanostructures on the surface, and potentially inhibit bacterial adhesion. A total of 12 thin films, both with and without copper coating are studied for their antibacterial efficiency, and the results are explained with their

topography and the release of copper ions from their surfaces. The thin films have been tested with both Gram-negative and Gram-positive bacteria, which representatives are E. Coli and B. Subtilis, respectively.

4.2 Choice of thin film material for antibacterial testing

At this point, with the recent addition of Zr-Cr and Zr-V to the list of Zr-based systems in which the competitive growth occurs, we now have 4 systems available for the antibacterial testing (the two others being Zr-Mo and Zr-W, as presented in **Chapter 1**). The antibacterial tests take time, and above all consume a lot of sterile resources that have to be disposed of after the tests. Moreover, the results for the antibacterial efficiency of all these films should not differ that much, given that they all show relatively similar surface morphologies. Thus, the antibacterial efficiency of only one system will be assessed here.

Between the 4 available systems, which SEM surface micrographs are shown in Fig. 4.1 (a-d), Zr-V has been chosen. The reasons behind this choice are multiple. First, as has been explained before, the bacteria are killed when they are exposed to copper ions. To do so, a thin copper coating will be sputtered on top of the film; the copper bactericidal effect being more efficient if the surface releases more copper ions, a higher surface area could be more bactericidal. Hence the better film will be the one presenting the highest surface roughness. The crystalline spherical caps on the Zr-V thin film are taller than for the other systems, which increases the developed surface area. The facets on top of the cones of Zr-V thin films are larger than those of Zr-Mo and Zr-W which might be hidden by the copper coating due to the tendency of copper to form round structures in sputtering, as can be seen in Fig. 4.1 (e) where the copper spherical structure have a diameter around 50-70 nm. Moreover, it has been shown that nanostructures somewhat similar to these tetrahedrons on top of the Zr-V films are efficient to

kill bacteria mechanically, potentially increasing the antibacterial efficiency. For these reasons, Zr-V thin films were considered as the best candidates for this application.
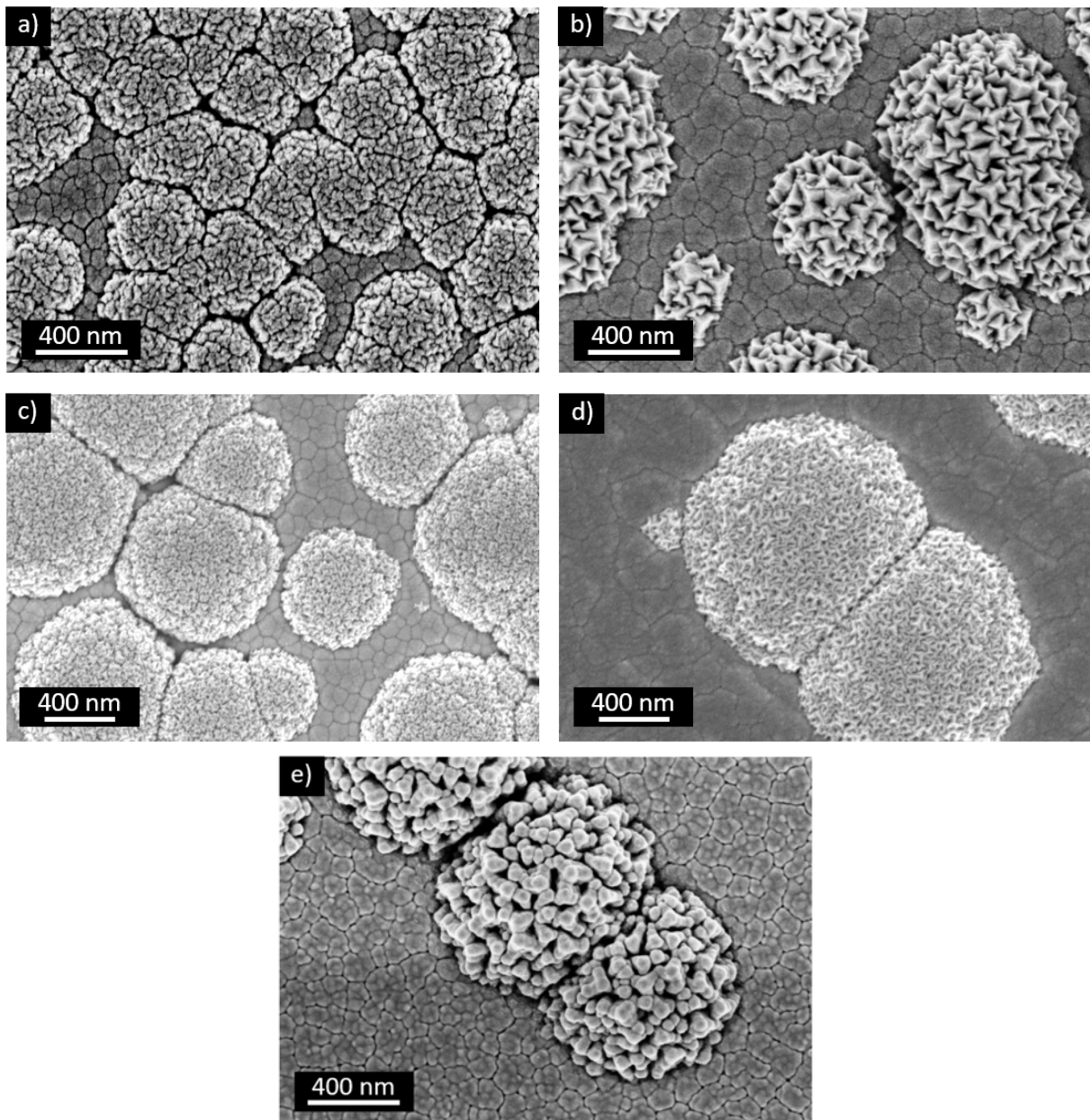
Fig. 4.1: SEM surface micrographs of Zr-Cr (a), Zr-V (b), Zr-Mo (c), Zr-W (d) and Cu-coated Zr-V (e) thin films.

4.3 The surface, the structure of the thin films and the copper coating

Assessing the antibacterial properties of a surface is great, but it would be better if this surface could exhibit an antibacterial chemical effect. However, neither Zr nor V are known for their intrinsic antibacterial properties. To overcome this and give chemical bactericidal properties to the films, one way is to coat the surface of the films with a thin copper coating, to take advantage of its intrinsic bactericidal efficiency. This is a practical way to give our surfaces antibacterial properties, as the copper coating can be deposited directly after Zr-V thin film deposition, in the same deposition chamber in less than 2 minutes. The Zr-V thin films before and after being covered by a thin copper coating are shown in Fig. 4.2 (a) and (b), respectively.
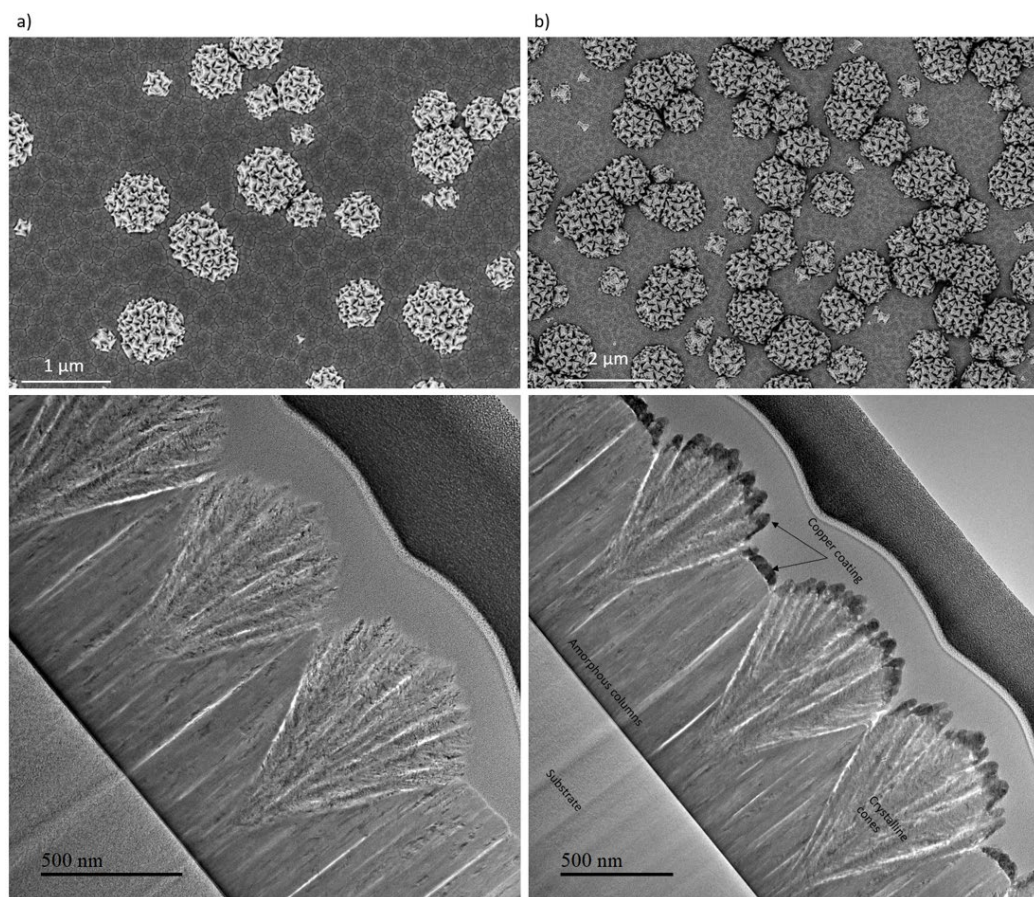
Fig. 4.2: SEM surface micrographs and TEM images of a Zr-V thin film before (a) and after (b) copper coating.

The copper coating on top of our films has a mean thickness of 67 nm and as can be seen in Fig. 4.2 (b), respects the surface features (spherical cap, tetrahedrons facets) without obstructing them. This means that the large developed surface area of the Zr-V films is preserved. Still, this technique of coating our surface with copper suffers from a drawback; as can be seen on the TEM image in Fig. 4.2 (b), the copper coating is discontinuous at the interfaces between the caps or between a cap and the columns. This is inherent to the technique used, as the sputtered atoms cannot reach these zones due to shadowing effects. A difference in copper thickness is also found between the amorphous columns and crystalline cones, 63 nm and 71 nm, respectively. Nevertheless, considering the size of the bacteria being in the micrometer range, the copper coating discontinuity will not affect the results of the antibacterial tests.

The surface of these thin films can be tailored nearly at wish by varying the film thickness. As a result, it is possible to synthesize thin films with a wide variety of surface morphologies. For this study, the antibacterial properties of 2 reference samples and 12 different thin films will be assessed. 6 of them will be as deposited Zr-V thin films, while the 6 others will be the same films with a copper coating. Each set of 6 films differs in regards to their surface coverage by the crystalline phase, hereafter named the coverage. As is shown in Fig. 4.3, the synthesized thin films result in 0 %, 20 %, 40 %, 60 %, 80% or 100 % coverage as assessed by image analysis. The Zr-V thin films are shown in Fig. 4.3 (a), while the Cu-coated Zr-V thin films are shown in Fig. 4.3 (b).
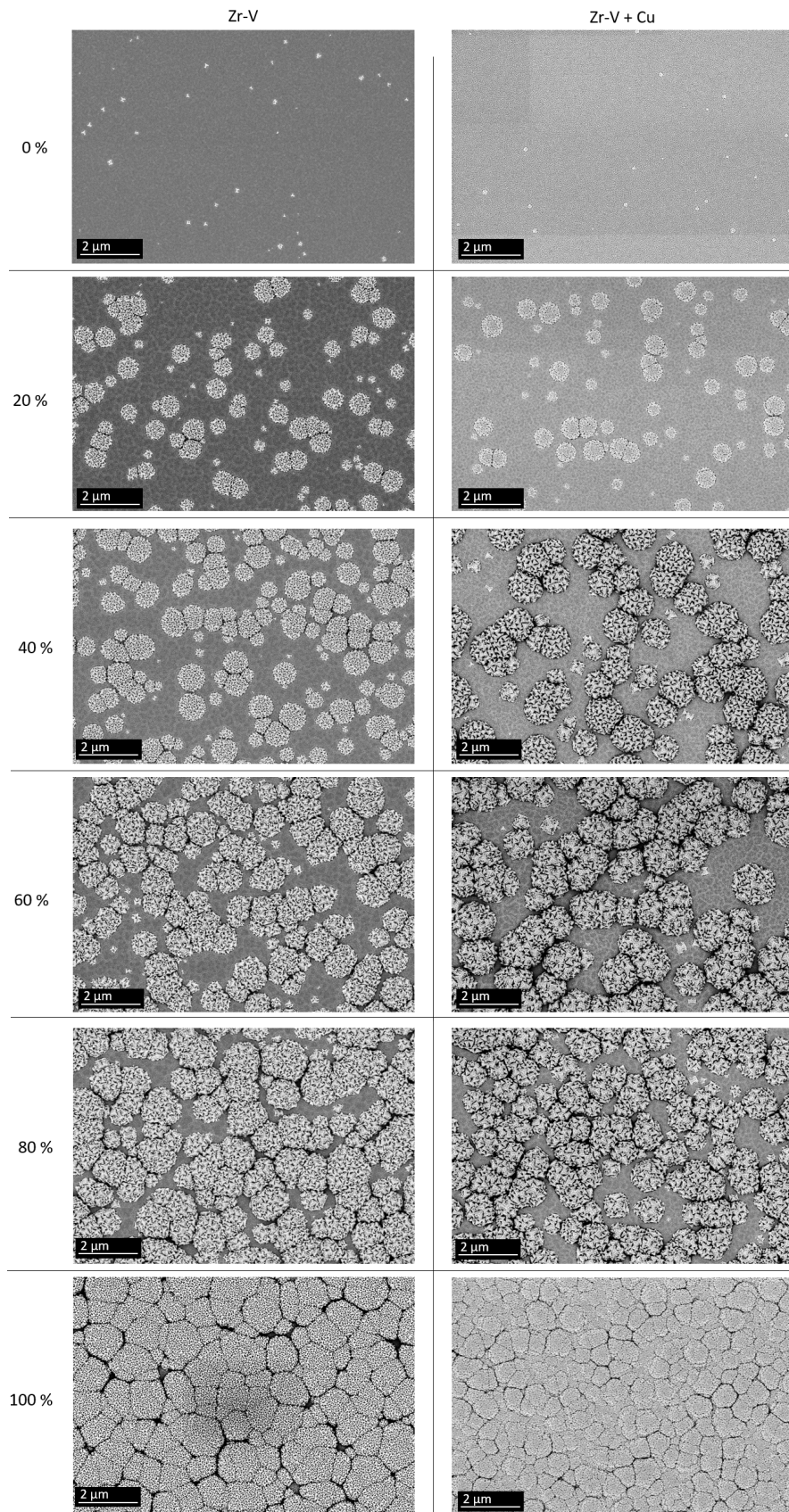
Fig. 4.3: SEM surface micrographs of the thin films used in this study; Zr-V thin films (a) and Cu-coated Zr-V thin films (b). The percentage written is the crystalline phase surface coverage.

As can be seen, varying the thickness leads to the synthesis of thin films with drastically different surfaces. The films showing 0 % of surface coverage by the crystalline phase are therefore totally amorphous and it results in a relatively flat surface, while the others are textured, with the spherical caps height becoming gradually higher and covering a higher percentage of the surface.

To further examine the surface of the films, AFM has been used to characterize their roughness. The results are shown in Fig 4.4, where the AFM images of the surfaces are presented along with their associated height distribution functions. The 0 % films show the lowest roughness values as the only roughness on these comes from the tops of the amorphous columns: the distribution function is monomodal. The roughness increases for the 20 % films with a first peak corresponding to the amorphous region of Zr-V (covered or uncovered by Cu) and the very shallow broad peak at higher heights correspond to Zr-V cone tops (covered or uncovered by Cu). Both films, before and after coverage by copper, show nearly identical roughness and height distribution functions, whose peaks are slightly shifted towards higher values. When reaching 40 % coverage, along with the main peak shift is also seen the development of the broad signal resulting from the top of the cones. This signal then intensifies with higher coverages until the whole surface is covered by the crystalline phase and, finally, the first peak disappears.
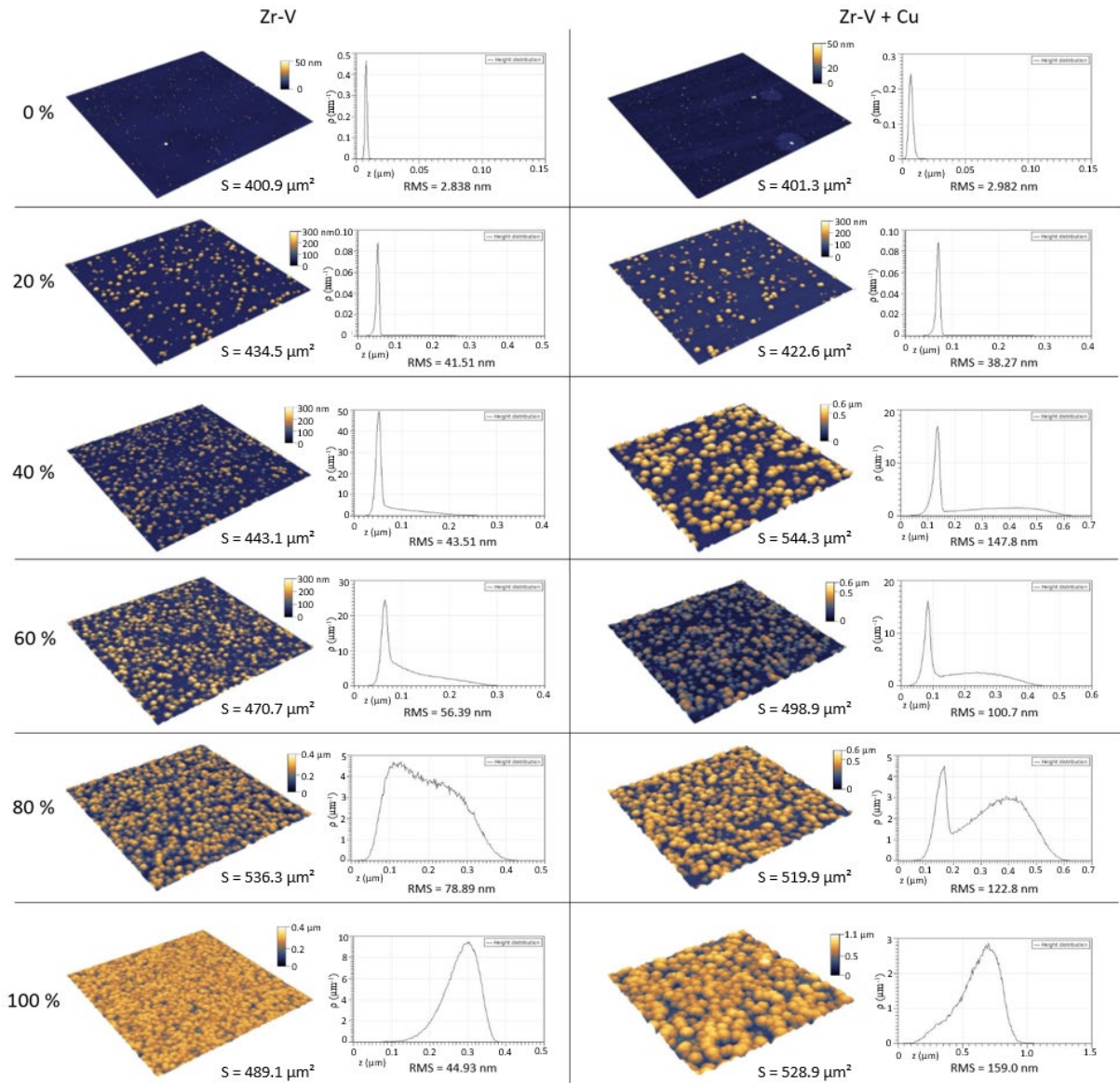
Fig. 4.4: AFM images (20 x 20 µm²) of the studied surfaces (Zr-V and Cu-coated Zr-V), their associated height distribution functions and RMS roughness. The percentage indicated for each sample is the surface coverage by the crystalline phase.

4.4 Antibacterial efficiency of these thin films

In this part will be presented the antibacterial tests results for the thin films as compared to reference copper and stainless steel samples, and we will try to interpret the differences between the films efficiency.

4.4.1 Antibacterial efficiency of the Zr-V thin films

The first samples to be tested are the Zr-V samples, along with the stainless steel reference. The results of this test are shown in Fig. 4.5. This graph represents the Colony Forming Units (CFU) that survived after the exposure to the surface during 30, 60 or 120 minutes. A colony forming unit is a bacterial cell that kept its capacity to multiply after the test. Thus, the CFU count decrease with exposure time can be attributed to 3 effects: the bacterium has been killed, the bacterial cell is still attached to the surface and will not be counted, or it has been damaged and lost its ability to multiply. A bacterium can be killed by the exposure to copper ions or by mechanical rupture, which means for these Zr-V films not coated by copper, only the second can happen. Bacteria can adhere irreversibly to the surface when given enough time, and the pipetting cannot detach them. When the bacterium is damaged, it can either lose its ability to multiply or be stressed and temporarily go dormant [127,128]. In this state, the bacteria are still viable but not cultivable; this is the result of a survival mechanism of the bacterial cells, slowing down their metabolism in harsh situations (like these antibacterial tests) until more favorable conditions are met. This is the reason why the agar plates were left to incubate for 3 days rather than overnight, to leave sufficient time for these dormant bacteria to resume growth.

As can be seen in Fig. 4.5, the E. Coli CFU reduction on these surfaces is quite low, most of the surfaces did not even significantly reduce the CFU. Each surface showed a higher reduction of the survival count than the stainless steel reference, but only the 100 % sample shows a significant reduction in CFU, indicating that one of the 3 aforementioned effects is present here. As the CFU reduction is low and no difference has been found between the CFU counts after 12 hours and 3 days, it is not likely that they went dormant. This leaves us with 2 hypotheses: either the bacteria were mechanically killed by the surface, or they irreversibly adhered to the surface. The fact that this surface is the one with the maximum density of

tetrahedrons tops, it hints towards the mechanical killing of the bacteria. However, without a quantitative bacterial adhesion assay and a bacterial viability test using a fluorescent staining kit, it is not possible to conclude between the mechanical killing or the irreversible adhesion. Either way, whether the CFU reduction is due to adhesion or mechanical rupture of the cells, this only affected at most around 40 % of the bacteria in the solution.

For the stainless steel sample, it has to be noted that the increase in CFU after exposure is not significant. Bacteria do not have nutrients to multiply during the test because the bacteria have been washed several times before testing, and thus are not able to multiply during the test.

Fig. 4.5: Results of the wet plating test with E. Coli for the Zr-V thin films and the stainless steel reference sample, counted after 3 days of incubation. The vertical scale is linear.

On one hand, hints of mechanical rupture have been observed, as shown in Fig. 4.6 (a, b). It can be seen that both bacteria are severely deformed by the surface below them. As it has been shown that bacterial cell deformation leads to rupture [113], the hypothesis of the mechanical rupture of the bacterial cells should not be ruled out. The time of the mechanical rupture test usually is close to 24 hours while our wet plating experiments lasts 2 hours, which may not be enough to rupture the bacterial cell [113]. As seen in Fig. 4.6 (b), the bacterial cell membrane seems heavily deformed due to its adhesion to both amorphous and crystalline surfaces. A careful observation of the distribution of C in the image shown in Fig. 4.6 (c) outlines the bacterial cell membrane, hinting that it is indeed deformed, and could potentially lead to the rupture of the bacterial cell membrane.
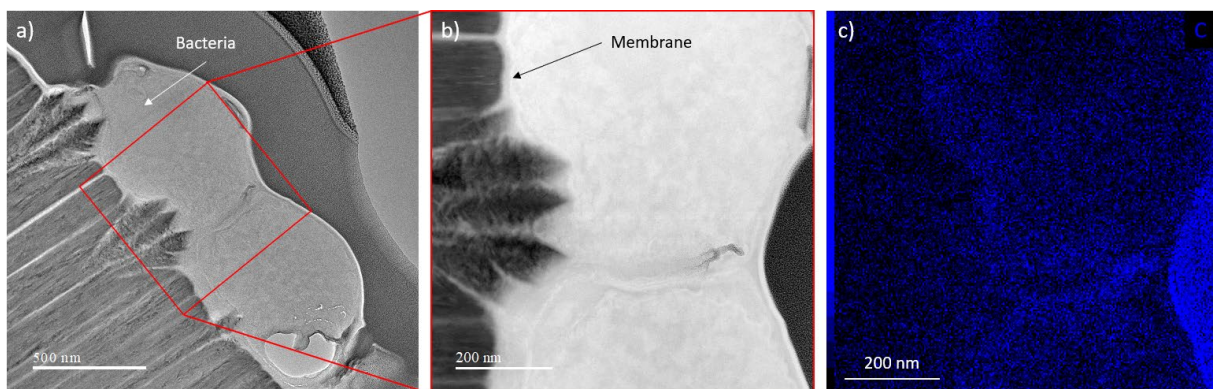
Fig. 4.6: TEM images showing bacteria on a dual-phase Zr-V thin film after wet plating (a, b) and EDS cartography showing the distribution of C in the studied region (c).

On the other hand, the B. Subtilis CFU reduction on these surfaces is much higher, up to 94 % of the bacteria in the testing solution as shown in Fig. 4.7. This time, all samples including the flat stainless steel reference show a significant reduction of the bacteria count after 60 min or more exposure time, and some even show a significant reduction after 30 min. For the same reasons as before, the hypothesis of the bacteria dormancy can be rejected.

However, unlike E. Coli, B. Subtilis cells have a high number of flagella on their surface that power swimming and swarming motility [129,130]. Swimming motility describes the cell movement in a liquid volume [131] while swarming motility is the two-dimensions movement of cell groups on a solid surface [132]. The B. Subtilis bacteria thus have a higher motility than E. Coli, and their ability to actively search for the surface is better [132]. This means that B. Subtilis should adhere to surfaces more easily than E. Coli, resulting in fewer bacteria count in the wet plating tests. This is coherent with the fact that a higher CFU reduction is found for B. Subtilis than for E. Coli, and can be attributed to the higher adhesion rate of B. Subtilis on the surface. The hypothesis of the mechanical rupture of the cells is here less likely, also knowing that mechanical rupture of bacterial cells has currently only been reported for Gram-negative bacteria [112,113]. Thus, the hypothesis coming from these results is that both bacteria more easily adhere to the 100 % coverage sample. For B. Subtilis, adhesion would also be facilitated on the flat steel surface and the 80 % coverage sample.
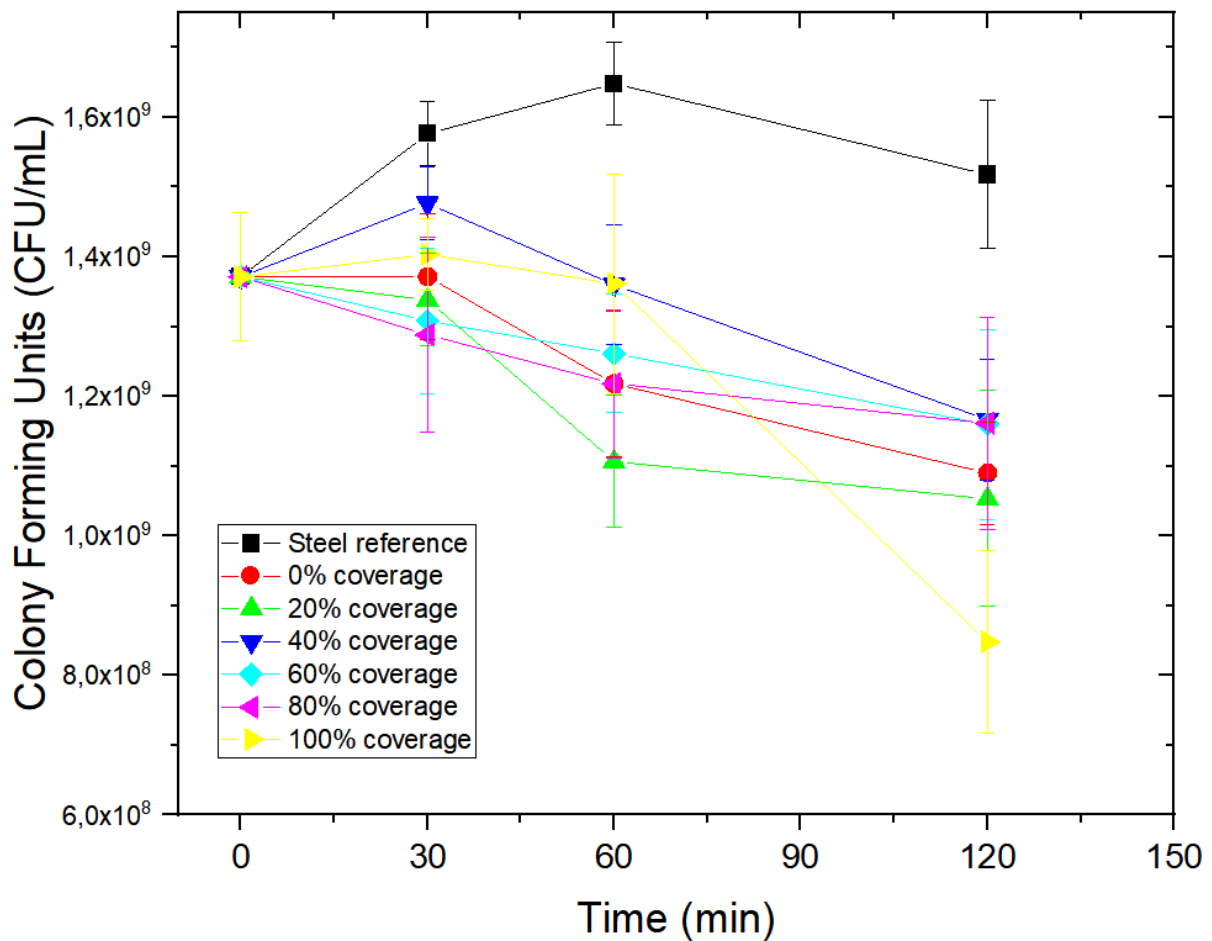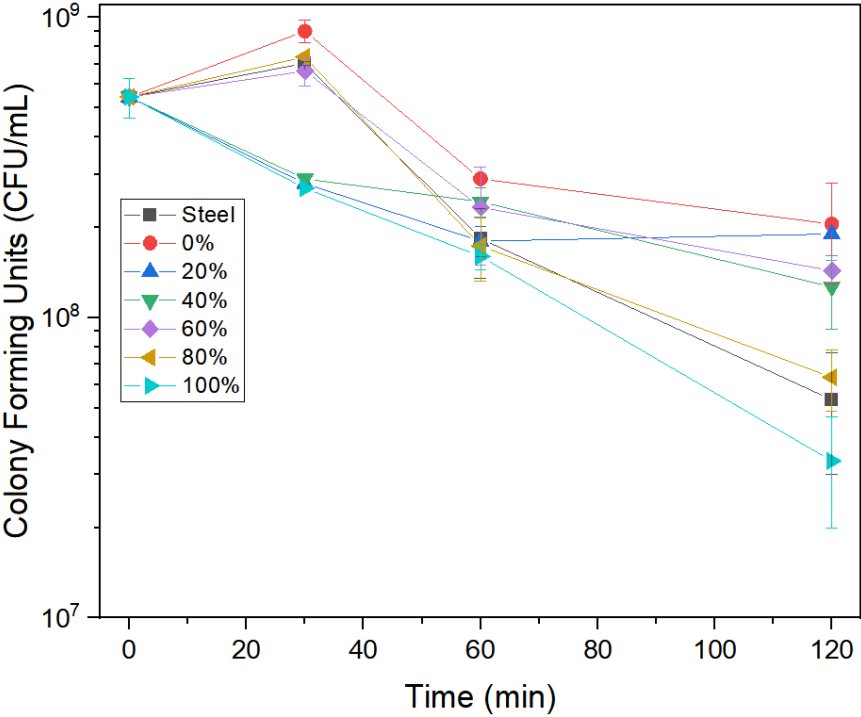

Fig. 4.7: Results of the wet plating test with B. Subtilis for the Zr-V thin films and the stainless steel reference sample, counted after 3 days of incubation. The vertical scale is linear.

4.4.2 Antibacterial efficiency of the Cu-coated Zr-V thin films

Then comes the test that will gauge the antibacterial efficiency of the Cu-coated Zr-V thin films, revealing the bactericidal nature of these surfaces. These films have also been tested along with the flat copper coupon (referred to as Cu reference below) against E. Coli and B. Subtilis. The results of the tests against E. Coli are shown in Fig. 4.8. The line and symbols represent the CFU survival count after exposure to the surface of the films, while the columns represent the CFU reduction rate, i.e. the rate at which the bacteria are killed by each surface. The higher the CFU reduction rate, the more bactericidal the surface. This above all gives a better readability to the results, as both express the same effect.
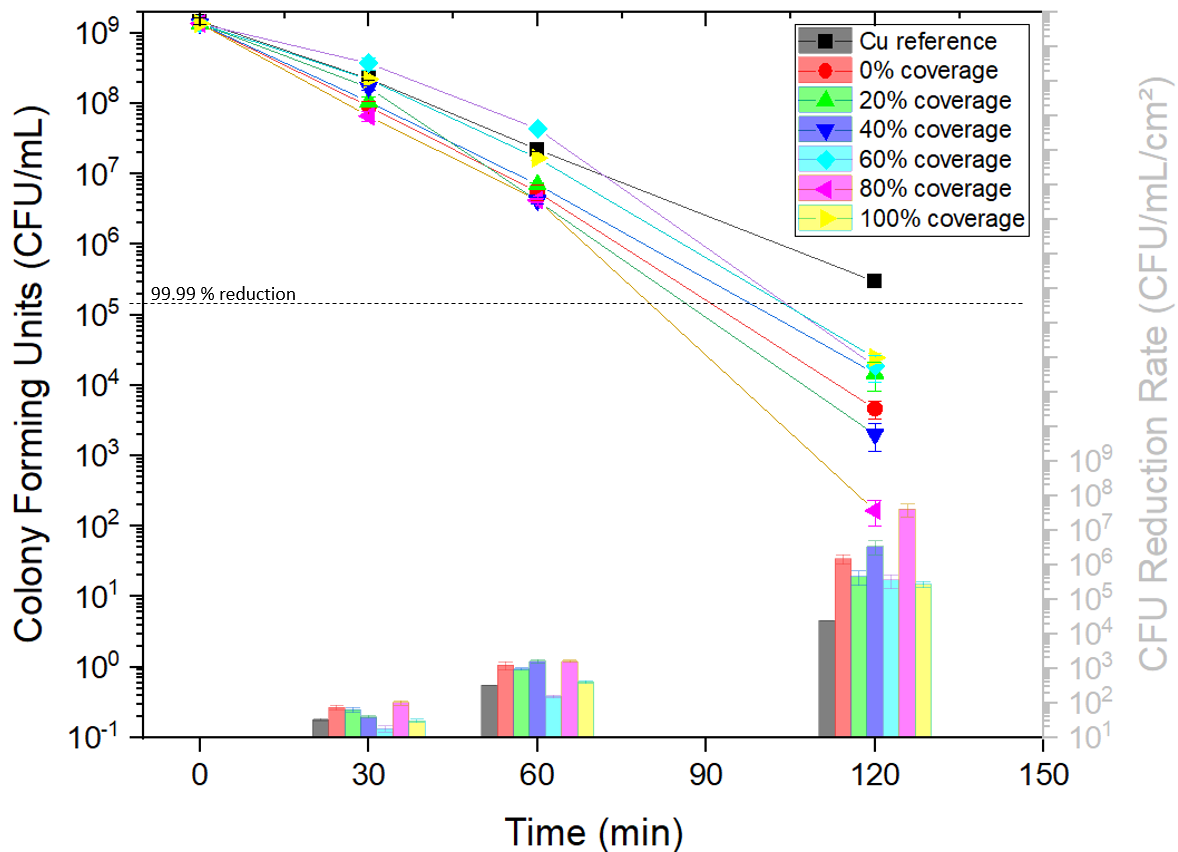
Fig. 4.8: Results of the wet plating test with E. Coli for the Cu-coated Zr-V thin films, along with the Cu reference after 3 days of incubation. The vertical scale is logarithmic, the plotted lines and symbols show the number of bacteria that survived after exposure to the surface, while the columns show the bacterial reduction rate.

During the wet plating test, the surfaces release copper ions, and their concentration has been evaluated using ICP-MS. The concentration of copper ions in the droplet for each surface and time is shown in Fig. 4.9 (a) along with their copper ion release rate. As can be seen, the copper ion concentration increases nearly linearly with increasing time. The copper ion concentration in the droplet is also shown in Fig. 4.9 (b), along with the developed surface area of the samples. When crossing with the developed surface area of each sample obtained via AFM, one can observe that in this study, the copper ion concentration is not correlated with the surface area. This shows that the copper ion release does not only depend on the developed copper surface area.
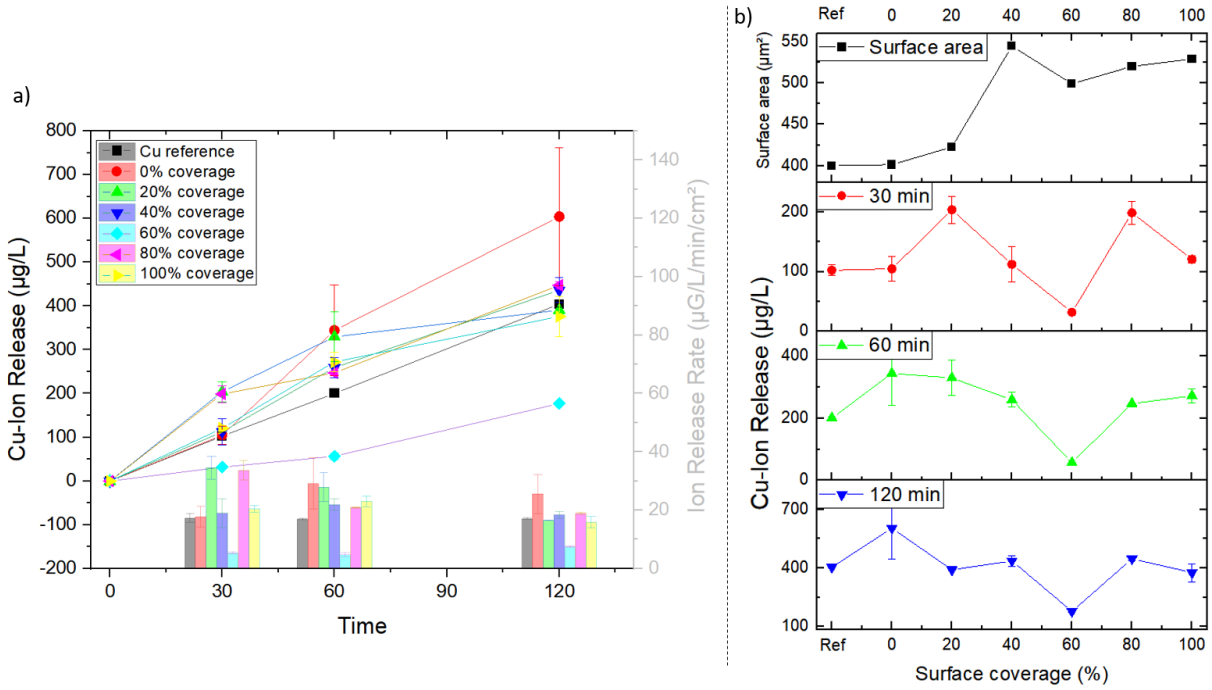
Fig. 4.9: Copper ion release and copper ion release rate in the droplet after exposure to the surface during the wet plating test (a), and developed surface area of each sample for a 20*20 μm² surface, and copper ion concentration in the droplet after a given exposure time of the E. Coli bacteria testing solution to the surface (b).

The simultaneous study of the bacterial survival and the copper ion concentration in the droplet gives rise to Fig. 4.10, that shows the CFU reduction rate depending on the measured copper ion concentration. As expected since copper ions are bactericidal, increasing the copper ion concentration increases the bacteria killing rate. All films show this tendency, with differences in efficiency; the 60 % coverage shows the best antibacterial efficiency for low copper ion concentrations: its antibacterial efficiency is lower than the other films but is accompanied by a much lower copper ion release.
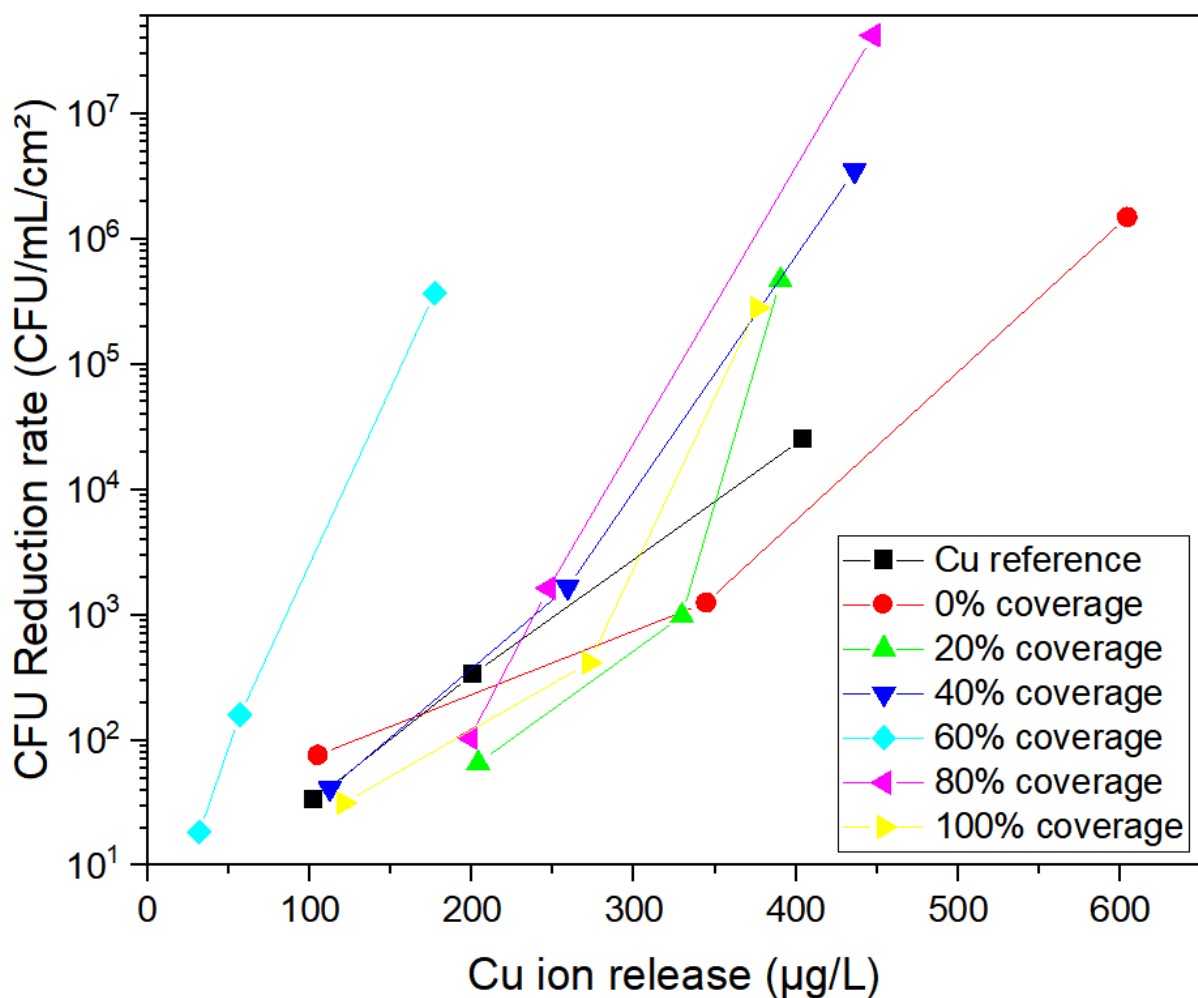
Fig. 4.10: E. Coli CFU reduction rate depending on the Cu ion concentration in the droplet. The vertical scale is logarithmic.

In the light of these data can the bactericidal efficiency of our surfaces be assessed. The first observation here is that, except for the 60 % coverage sample, all our samples show a better antibacterial efficiency than the copper reference at killing bacteria no matter the exposure time. As expected, this increase in antibacterial efficiency goes along with an overall increase in copper ion release rate, as more copper ions means a higher killing potential, the films often showing a higher copper ion release. This higher copper release, while not correlated with the surface area, could originate from the fact that the copper on our thin films was sputtered and not cast as the copper coupon.

Surprisingly, the 60 % coverage sample gains in efficiency between 60 and 120 minutes. It has previously been shown that the killing of bacteria is strongly attenuated when the bacteria are not able to adhere to the surface [133], but also that it was not accompanied by a decrease in copper ion release. But for this sample a strong decrease of copper ion release is indeed observed, as compared to our other samples. Thus, another hypothesis is that this copper coating has been corroded into Cu_2O with time, explaining its poorer antibacterial efficiency and copper ion release [134]. A XRD analysis was performed on the Cu-coated films, and the presence of copper oxide was not detected in any film; either the thickness of this oxide layer is thin, or there is no copper oxide in this film. The fact that only the 60 % coverage film would be oxidized can be understood through stresses in the film. For films with a low surface coverage, the matrix is amorphous and shows a compressive stress, not allowing the nanocolumns from isolated crystalline cones to relax substantially. When the surface coverage exceeds 50 %, percolation of the crystalline cones is attained and the nanocolumns can expand at the expanse of the amorphous regions, thus forming voids in the copper coating after deposition and possibly making oxidation easier. When the surface coverage increases further, the nanocolumns are not able to expand because they are blocked by other nanocolumns from an adjacent cone.

As a contact between the bacterial cell and the surface is necessary for the copper ions to effectively kill the bacterium, hence when increasing the surface coverage up to 60 %, the large flat amorphous surfaces become rarer and bacteria now have to adhere on the crystalline cones; this is harder for them and could lead to a reduced adhesion. When increasing the surface coverage up to 80 %, more surface is covered by the cones and bacterial adhesion on adjacent cones could be easier. We can expect that as bacterial adhesion is linked with bacterial death, the 80 % coverage sample shows a higher antibacterial efficiency than the 60 % sample. It has to be noted that there could be a difference in bacterial cell adhesion between copper and copper oxide [135]. In addition with this adhesion difference could also come a difference in mechanical deformation of the bacterial cells. Indeed, the height difference between the cones and the flat amorphous matrix is different for each film, as seen in Fig. 4.4. When using the maxima of each height distribution, the height difference between amorphous and crystalline surfaces varies between 0 nm for the reference and the 0 % and 100 % coverage films, up to ~300 nm for the 40 % coverage sample. This height difference could well induce mechanical deformation in the cell.

For this study, the most promising surfaces here are the 0 %, 40 % and 80 % coverage films. For each of the 3 studied exposure times, they showed great antibacterial efficiency as compared to the other samples. Concurrently, the 20 % sample showed higher efficiency than most samples for lower times, but this efficiency slowed down as time increased; the same trend is observed for its copper ion release.

The same wet plating test has been carried on the same samples against B. Subtilis, representative on the Gram-positive bacteria in this study, with a bacteria testing solution counting $5.43.10^8$ CFU. The results of this study for a 120 min exposure time are shown in Fig. 4.11. Unfortunately, the CFU count on the LB agar plates after incubation for 30 min and 60 min exposure times was nearly always 0, indicating that the droplet extracted from the

surface has been too diluted before plating. This resulted in a too small number of bacteria in the final plated solution, making it impossible to conclude on the precise number of bacteria that survived the test. The only result from this is that the CFU count in all droplets is less than 10^7 after 30 min and less than 10^5 after 60 min. While no quantitative result could be obtained, we can still observe that the killing of B. Subtilis on our surfaces is faster than the killing of E. Coli. This result was reported in the literature, where a delay for E. Coli killing was observed while the killing and lipid peroxidation of B. Subtilis began immediately; these authors hypothesized that the outer membrane of E. Coli could serve as a potential barrier to the reactive oxygen species, thus delaying membrane lipid peroxidation and cell death [136].

As can be seen in Fig. 4.11, the 20 % and 40 % coverage samples show a significantly better antibacterial efficiency than the other samples against B. Subtilis. This difference presumably does not come from a difference of bacterial cell attachment on the surfaces, due to the difference in order of magnitude between the adhesion and killing phenomena.
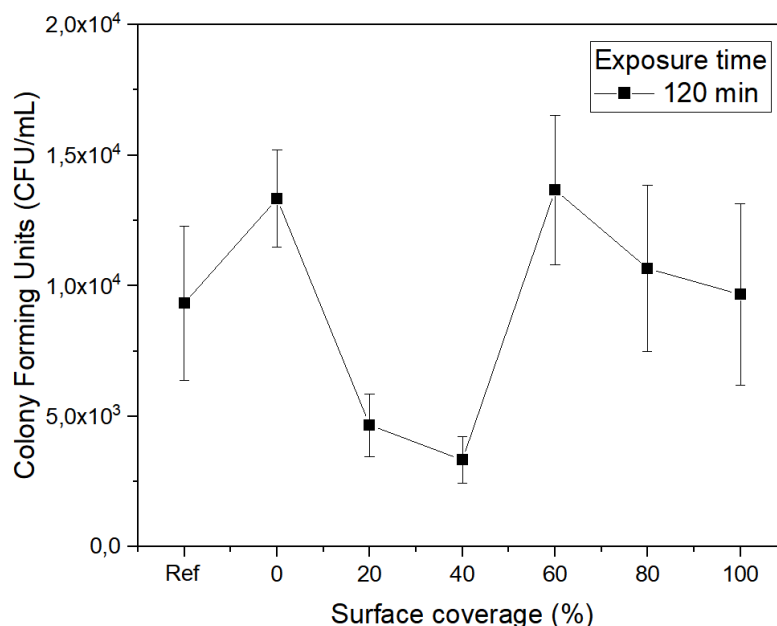
Fig. 4.11: Results of the wet plating test with B. Subtilis for the Cu-coated Zr-V thin films, along with the Cu reference for a 120 min exposure time. The initial CFU count in the bacteria testing solution was 5.43×10^8.

In the end, there is no such thing as the perfect Cu-coated Zr-V thin films that would show a higher antibacterial efficiency than all the other samples for each exposure time and each studied bacterium. Still, the 20 % and 40 % coverage samples efficiency is always better than the mean of all our samples. Thus, these two are the most promising for the one-step bottom-up elaboration of polyvalent antibacterial surfaces.

4.5 Chapter conclusions

Amongst all the Zr-based systems that exhibit the competitive growth between amorphous and crystalline phases, Zr-V has been chosen for its potentially higher developed surface area and tetrahedrons on top of the crystalline cones that could mechanically rupture bacterial cells. To render these films bactericidal, a 67 nm-thick copper coating has been sputtered on top of the Zr-V thin films, while making sure that the peculiar topography of the Zr-V thin films remained intact. In this study, with two flat copper and stainless steel references, 12 different Zr-V thin films have been tested, from a totally amorphous surface up to a surface fully covered by crystalline cones. The wet plating test consisted in the counting of the remaining CFU after exposure of the bacteria to the surfaces. Here, a Gram-negative and a Gram-positive bacteria have been used, which respectively were E. Coli and B. Subtilis. Against E. Coli, all our Cu-coated thin films exhibit a better antibacterial efficiency than the copper reference, which was accompanied by an increase in copper ion release during the test. The only exception is the 60 % coverage sample, which poor antibacterial efficiency may be explained by its copper layer that oxidized into Cu_2O with time. Against B. Subtilis, only the 20 % and 40 % coverage thin films showed a better antibacterial efficiency than the other samples after 120 min. We showed that a higher developed surface area is not directly linked with better bactericidal properties. While the hypothesis of the mechanical rupture of the

bacterial cells is still not ruled out, it is more likely that the CFU reduction on the Zr-V samples is due to the irreversible bacterial attachment on the surfaces. To confirm this, quantitative surface adhesion test must be carried on these surfaces, as well as bacterial viability tests for longer exposure times with staining to differentiate adhered and dead bacteria on the surface.

Chapter 5

Link between evolution of film internal stress during growth and the microstructure of dual-phase Zr-based thin films

ABSTRACT: In this chapter, the close link between the internal stress during dual-phase Zr-based films growth and the film microstructure is analyzed. This study uses in-situ stress measurements during film growth, and the results are put up against previous ex-situ results for dual-phase Zr-based thin films. We try to explain the differences observed between in-situ and ex-situ stress measurements and consider depositing films at a lower working pressure to gain insights on crystallization, and report thin films with a novel microstructure. Then, we gauge the plausibility of the hypotheses for the crystalline phase nucleation.

Contents

5.1 Introduction

The amorphous-nanocrystalline competitive growth has already been reported to occur for thin films in various systems such as Si-H [27], Zr-Mo [14], Zr-W [13], Zr-Cr and Zr-V [137], TiO_2 [30], $BaTiO_3$ [42], Ti-Al [41] and Al-N [40]. However, the nucleation mechanism of the crystalline nucleus that leads to cone formation yet remains to be understood. For Si-H, authors have proposed that the internal compressive stress in the film leads to Si-Si bonds breaking, and eventually to nucleus formation [32]. In the Zr-W and Zr-Mo systems, Borroto et al. reported that, for Zr-W and Zr-Mo thin films deposited at 2 Pa, the residual stress after thin film deposition was guided by the crystalline volume fraction in the film during competitive growth [15], indicating that nucleation and intrinsic stress are closely related.

However, these stress measurements were ex-situ, i.e. conducted after the deposition of the films. The concerns are that after deposition, the stress state of the thin film can change for various reasons, resulting in biased residual stress measurements. In this chapter, we want to pursue this approach of linking the stress in the thin films with the crystallization in dual-phase thin films, but with in-situ stress measurements, overcoming the aforementioned issues. For this purpose, in-situ stress was monitored for Zr-Mo thin films to compare these results with the reported ex-situ results and verify their hypotheses, and for Zr-V thin films to extend the

knowledge on the nucleation in these systems. Additionally, this study will also monitor the stress evolution during growth of thin films deposited at a lower working pressure.

In this study, two different deposition chambers have been used for the thin films deposition. The first one is the same used to synthesize the thin films of the previous chapters with a target-substrate distance of 9 cm, while the other one differs in that the distance between the targets and the substrate is 18 cm. For this study, the pressure-distance (P*d) product was kept the same for the depositions regardless of the deposition chamber. For example, a thin film synthesized at 2 Pa working pressure in the first chamber and a thin film synthesized at 1 Pa in the second chamber both have the same P*d product of 18 Pa.cm.

5.2 Differences and similarities between films synthesized at 2 Pa and 0.5 Pa

The first step in this study is to replicate the previous study that measured the residual stress of dual-phase Zr-based thin films, except here the measurements will be conducted in-situ, i.e. during thin films growth. For this purpose, Zr-Mo thin films have been synthesized at a P*d product of 18 Pa.cm, and the in-situ stress measurements are shown in Fig. 5.1 (a). As can be seen on the X-ray diffractograms in Fig. 5.1 (c), the thin films are amorphous at 50.5 at.% Mo, dual-phase between 55.0 and 59.8 at.% Mo, and crystalline at 64.8 at.% Mo. Owing to its lower thickness, the 59.8 at.% Mo thin film has a lower crystalline volume fraction than the other dual-phase or crystalline thin films, and thus a lower (110) bcc Mo peak intensity. At this point, it is interesting to notice that these results differ greatly from reported ex-situ stress measurements in Zr-Mo thin films, as can be seen in Fig. 5.1 (b), where these are shown. It has been reported that the stress evolution could be divided in 3 phases: (1) with the growth of the amorphous phase, a compressive stress builds up in the film, then (2) the crystalline phase

growth induces a volume contraction and tensile stress component in the film and (3) the coalescence of the crystalline cones results in a compressive stress buildup.
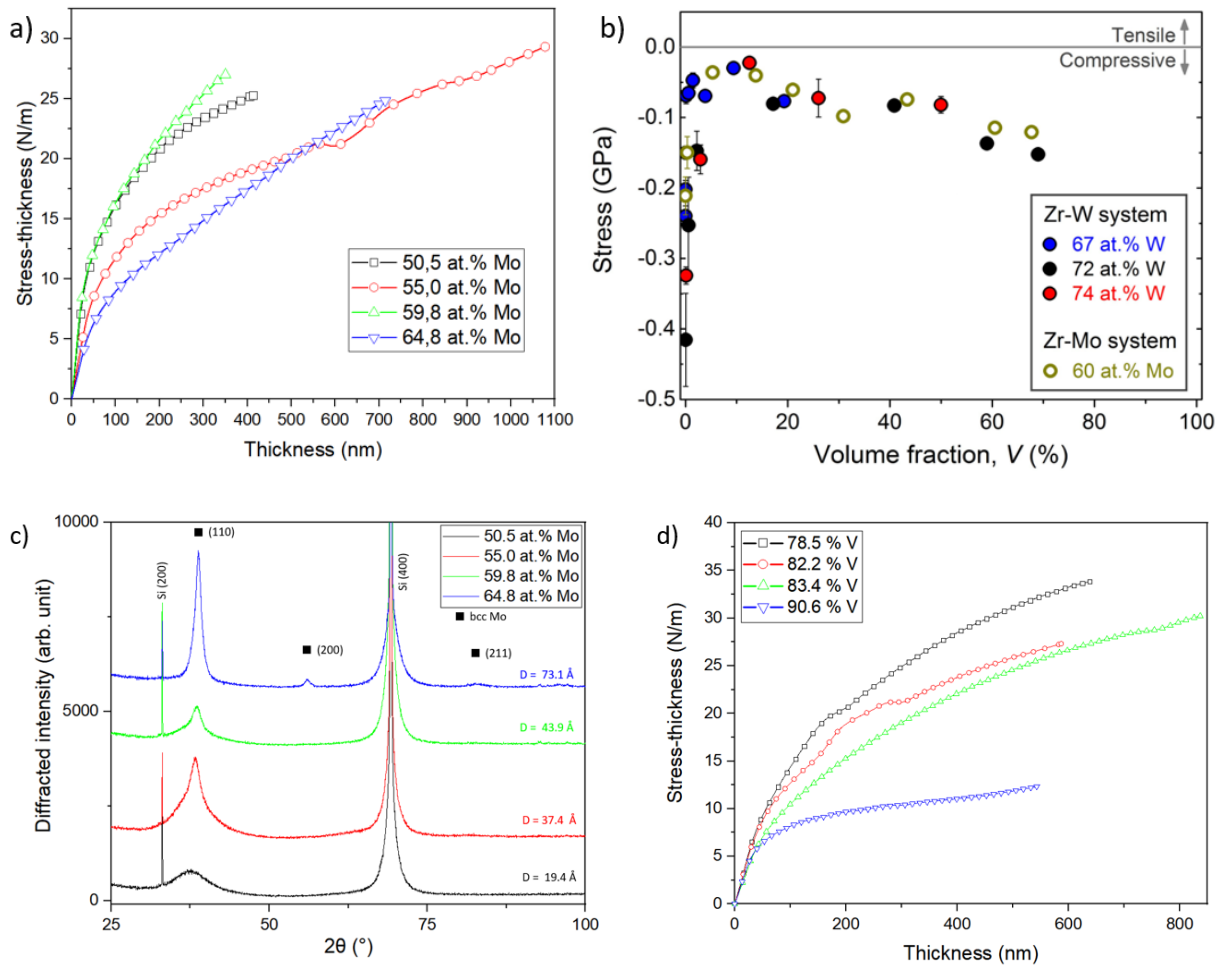
Fig. 5.1: In-situ stress evolution for Zr-Mo thin films during growth at a P*d product of 18 Pa.cm (a), ex-situ stress evolution after thin film deposition reported for Zr-Mo and Zr-W thin films grown at a P*d product of 18 Pa.cm (b), from Ref. [14], x-ray diffractograms of the Zr-Mo thin films (c) along with their crystallite size D calculated with the (110) bcc Mo peak, and in-situ stress evolution for Zr-V thin films during growth with a P*d product of 18 Pa.cm (d).

In our in-situ stress measurements, the growth of the amorphous phase is not associated with a compressive stress buildup, as a tensile stress is observed in the beginning of the thin film growth. The incremental stress in our thin films is never compressive. The same results

have been obtained for amorphous, dual-phase and crystalline Zr-V thin films grown at a P*d product of 18 Pa.cm, as can be seen in Fig. 5.1 (d).

From the difference between these results and the previously reported residual stress measurements, it appears that the amorphous-crystalline phase transition does not leave a mark on the stress during growth, but only after deposition. During growth, the stress buildup associated with the phase transition might be obstructed by another phenomenon. The hypothesis here is that the void between the columns loosen the interactions between them during growth. After the deposition, when the film is subjected to air, voids fill with oxides and the film adsorbs moisture, filling the voids and pulling the columns from each other, thereby creating compressive stress [138]. This correlates with the fact that there seems to be matter instead of voids in for instance a Zr-Cr thin film, as can be seen in Fig. 5.2 (a).

Thus, great differences exist between stress measurements during and after thin film growth. Fig. 5.2 (b) shows the evolution of the stress in an Al thin film during and after growth. As can be seen, even for in-situ conditions, the value of the average stress in the film differs greatly after the deposition, and in this case it was only due to stress relaxation, without the contributions of oxidation and moisture adsorption. Fig. 5.2 (c) represents the stress in the film at different thicknesses. An arrow pointing towards the film is compressive, while one pointing outwards is tensile. The represented stresses come from the curvature evolution during film growth as shown in Fig. 5.2 (d), where a tensile stress at low thicknesses is progressively replaced by a compressive stress, as represented in Fig. 5.2 (d). The incremental stress corresponds to the effect of adding matter to the surface, and is proportional to the slope of the stress-thickness curve at the considered thickness, while the average stress in the film is proportional to the slope of the line from the origin to the curve at the considered thickness. After deposition, the stress in the film relaxes, as can be seen in Fig. 5.2 (e).
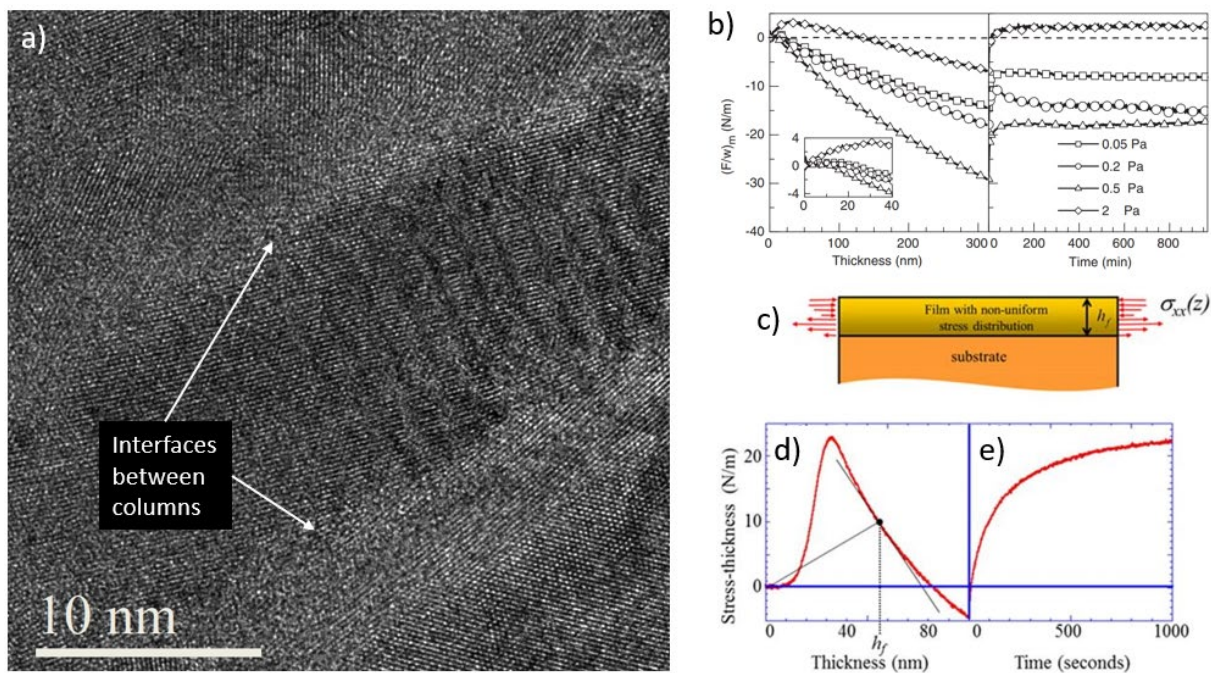
Fig. 5.2: TEM image of a Zr-Cr thin film with matter instead of voids between the columns (a), evolution of stress in an Al thin film during and after deposition (b), from Ref. [139], schematic representation of the incremental stress in a thin film during growth (c), stress evolution during the growth of an Ag thin film (d), and stress evolution after deposition has ended (e). From Ref. [140].

In the light of this data, two conclusions can be drawn. First, if we want to understand the link between the internal stress during growth and the microstructure of the film, the measurement has to be conducted in-situ. Second, the thin films should be denser to avoid the obstruction of detection of the phase transition by the voids between amorphous columns. One way to overcome these obstacles is to monitor the stress during growth of a thin film grown at a lower working pressure. As a result, the target atoms that are ejected with the same average energy would experience less collisions with the background gas and have more kinetic energy when impinging the growing film and promote adatom mobility. This would lead the film to be denser and potentially allow us to see a stress change associated with a phase transition.

Thus, Zr-V thin films have been deposited at a lower working pressure, resulting in a P*d product of 4.5 Pa.cm. In Fig. 5.3 are shown surface and cross-section SEM micrographs of Zr-V thin films grown at a P*d product of 18 and 4.5 Pa.cm, respectively. Apart from the increased film density, the microstructures obtained in these two films are different. The first one is the one we are now used to, amorphous columns and crystalline cones. On the other hand, the second one resembles a pearlite structure on the surface, with columns elongated transversal to the film surface; these columns are elongated in a specific direction in each "grain", with "grain boundaries" between them. As can be seen on the tilted SEM micrograph in Fig. 5.3 (c), elongated columns are observed from around 200 nm above the interface with the substrate surface up to the film surface.

Interestingly, Borroto et al. reported that lowering the P*d product for dual-phase Zr-Mo thin films resulted in a denser amorphous matrix and a difference in geometrical shape of the crystalline regions, as their surface was flat (see **Chapter 1**). In the case of Zr-V thin films, the obtained thin films show a totally novel morphology. At this point, it is difficult to even recognize a competitive growth when only seeing the SEM micrographs; further characterizations have to be conducted.
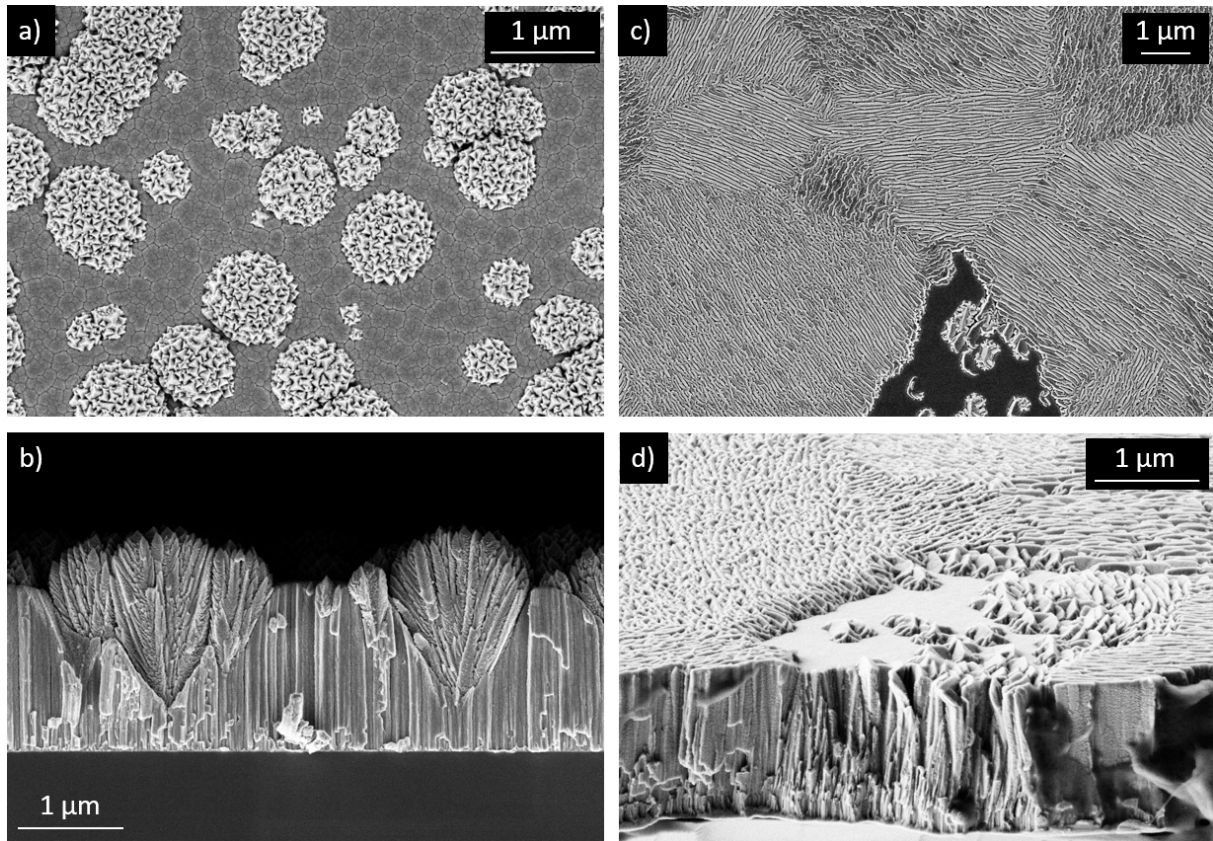
Fig. 5.3: SEM surface and cross-section of a Zr-V thin film synthesized at a P*d product of 18 Pa.cm (86 at.% V) (a, b) SEM surface and tilted cross-section of a Zr-V thin film synthesized at a P*d product of 4.5 Pa.cm (87.5 at.% V) (c, d).

5.3 In situ stress monitoring of amorphous, crystalline and dual-phase Zr-V thin films

To understand what happens during the growth of the thin films deposited at a lower pressure, in-situ stress monitoring of Zr-V thin films with different chemical compositions has been conducted and the results are shown in Fig. 5.4 (a). For the two films grown at 80.0 and 83.3 at.% V, the stress starts out compressive and a tensile component is found to build up between 400 and 600 nm, and could originate from void formation in the film [141]. As can be seen in Fig. 5.4 (b), these two films are totally amorphous. For the 91.1 at.% V film, the stress

130

starts out tensile with a high incremental stress (~1 GPa), and the film is totally crystalline as confirmed by its x-ray diffractogram. For the 87.1 at.% V, a compressive stress builds up at the beginning of deposition, then at ~180 nm the slope changes along with the development of a tensile stress component in the film. The incremental stress up to 180 nm is similar to what is observed for amorphous Zr-V thin films, while after 400 nm it resembles that of the crystalline thin film. This stress development could originate from an amorphous to crystalline phase transition during growth and is similar to what was reported by Borroto et al. for ex-situ measurements of Zr-W and Zr-Mo thin films deposited at a higher pressure.
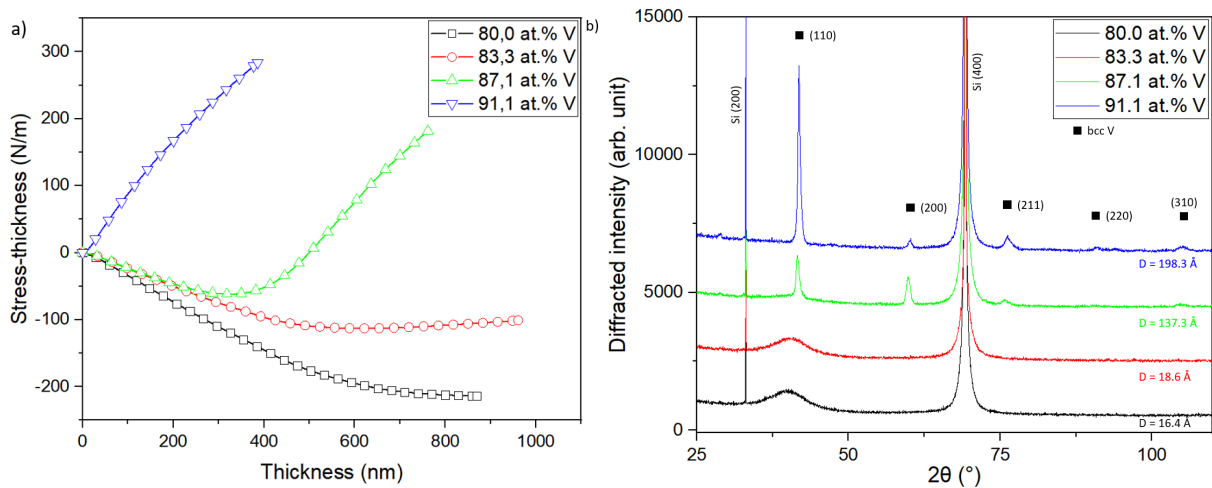
Fig. 5.4: In-situ stress measurements in amorphous, crystalline and dual-phase Zr-V thin films grown with a P*d product of 4.5 Pa.cm (a) and their x-ray diffractograms (b).

In Fig. 5.5 are shown the surface and cross-section of the 83.3, 87.1 and 91.1 at.% V thin films which are respectively amorphous, dual-phase and crystalline. As can be observed, the amorphous phase resembles a thin film metallic glass (TFMG) with its associated rupture profile. The crystalline film seems columnar with randomly oriented elongated grains on the surface. As for the dual phase film, it starts out amorphous and after a critical thickness is reached, a structure similar to the crystalline one emerges and seems to expend laterally. This

is coherent with the x-ray diffractograms that show a transition from amorphous to crystalline structures when increasing the V content in the films.
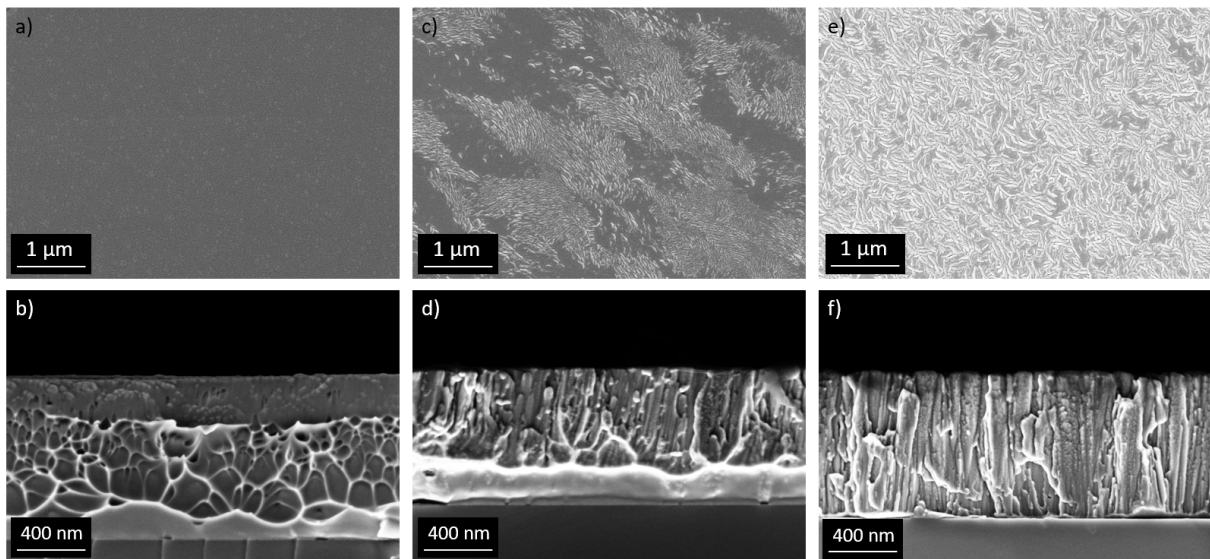
Fig. 5.5: SEM surface and cross-section micrographs of (a, b) 83.3 at.% V, (c, d) 87.1 at.% V and (e, f) 91.1 at.% V Zr-V thin films grown at a P*d product of 4.5 Pa.cm. The films are respectively amorphous, dual-phase and crystalline.

Nonetheless, while usually the x-ray diffractograms of dual-phase amorphous-crystalline thin films show a mixture of amorphous and crystalline signals, in this case the 87.1 at.% V film only shows a crystalline signal, contrasting with the information extracted from the stress monitoring suggesting amorphous and crystalline phase formation. This lack of mixed signal could be the result of change in film microstructure during deposition, which pushed us to replicate this thin film with different thicknesses to monitor the crystallinity and microstructure change with thickness. The x-ray diffractograms of these films are shown in Fig. 5.6 along with the crystallite size calculated with the (110) bcc V peak. From these results, the crystallization of the thin film occurs between 300 and 400 nm. The higher crystallite size for the most V-rich film as observed in Fig. 5.4 (b) could come from the fact that the

incorporation of Zr into bcc V is energetically unfavorable, as shown by the low solubility of Zr in V in thermodynamically stable equilibrium conditions [142]. Thus, increasing the Zr content increases the nucleation energy barrier explaining the crystallization occurring at higher thicknesses for increased Zr content observed in Fig. 5.4 (a). The surprising result however is that this crystallization is accompanied by the disappearance of the amorphous signal, suggesting the crystallization of the amorphous phase already deposited. Such crystallization during growth has not been reported for these dual-phase thin films, as has this morphology never been observed, to the best of our knowledge. Both these crystallization of the amorphous layer and morphology need to be further explored.
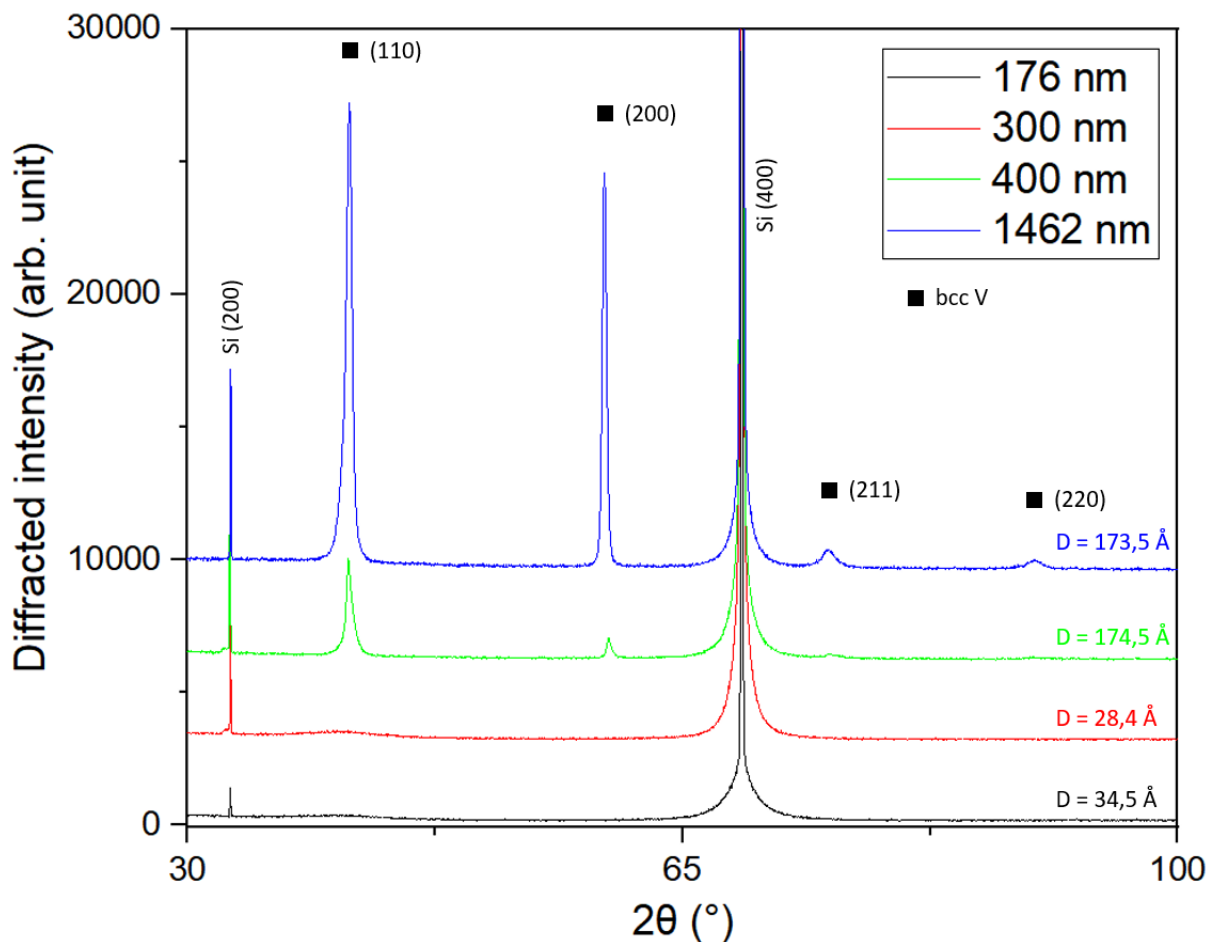
Fig. 5.6: X-ray diffractograms of Zr-V thin films grown at a P*d product of 4.5 Pa.cm, with a 87 at.% V chemical composition at different thicknesses. On top of each diffractogram is written the crystallite size D calculated with the (110) bcc V peak.

To test the hypothesis of in-situ amorphous phase crystallization during growth, TEM as well as EBSD-TEM analyses have been performed. The lamella has been extracted from the film shown in Fig. 5.3 (c, d), and a TEM image of this lamella is shown in Fig. 5.7 (a). The zone on the left comes from a zone with elongated columns on the surface, while the zone on the right comes from a zone with a flat surface that appeared dark on the surface SEM micrograph shown in Fig. 5.3 (c). As can be seen on the TEM image in Fig. 5.7 (a), there is a change in morphology at around 200 nm, with a dense layer below 200 nm thickness that marks the bottom of the elongated columns. The orientation cartography performed on the same zone of the film is shown in Fig. 5.7 (b), where it is combined with the confidence index. The confidence index indicates the confidence of the software in the calculated orientation: the brighter the zone, the more confident it is. This figure shows the existence of a dense layer below 200 nm and, above 200 nm depending on the lateral position, either the cross section view of the aforementioned elongated columns or a dense layer of coarser morphology than the bottom one. All regions appear crystallized. The "grains" constituted by the elongated columns are polycrystalline, neighboring columns can have different in-plane crystallographic orientations. The bottom of the bundle of elongated columns show a preferential orientation which is the same as the one in the bottom layer, and at ~400 nm thickness the orientation in the columns changes from preferential to random. The film does not have the same crystallographic orientation depending the considered lateral location, below the elongated columns or below the flat region of the surface. Despite an interface can be distinguished around 200 nm between the bottom and top layers of the dense zones that are flat on the surface, they have the same orientation through their whole thickness with some degrees of disorientation in some places. Based on these observations, it is difficult to describe the sequence of crystallization steps and it might well be that initially amorphous regions have crystallized during processing by FIB.
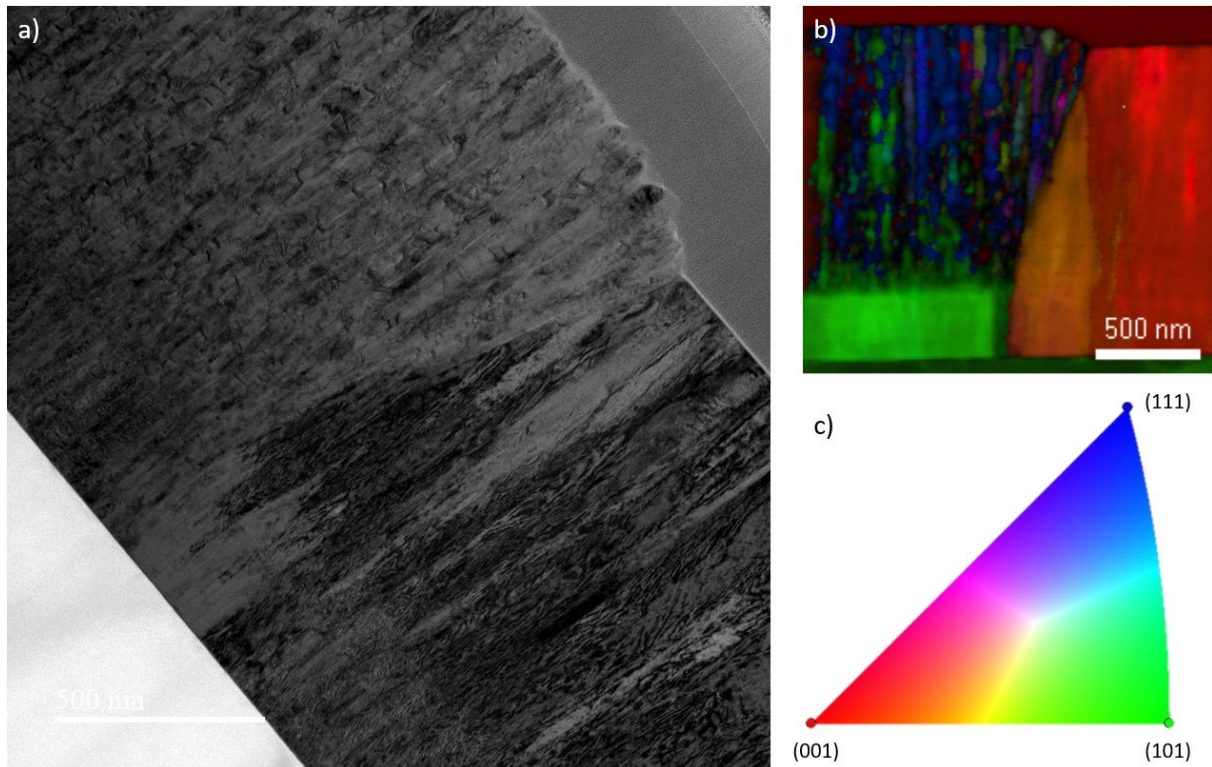
Fig. 5.7: TEM image (a), combination of the confidence index and orientation cartography (b) of a 1462 nm-thick Zr-V thin film synthesized at a P*d product of 4.5 Pa.cm, and colored orientation triangle to represent the orientation of grains (c). The confidence index expresses the confidence of the software in the computed orientation, the brighter the more confident it is.

The aim being the deciphering of the amorphous-crystalline phase transition, TEM analysis has also been conducted on the 176 nm-thick film, and a TEM image and its associated electron diffraction pattern are shown in Fig. 5.8 (a, b). Surprisingly, the whole film seems to be crystalline, as suggested by the lattice fringes on the TEM image and confirmed by electron diffraction. As a reminder, the x-ray diffractogram of this film showed its amorphousness. While the cutting times during the lamella preparation were the shortest possible to avoid heating, it is possible that this induced the crystallization of the amorphous film. As can be seen on the electron diffraction, the (110) bcc V direction is the most intense, which is an easy growth

direction. Unfortunately, this renders us unable to capitalize on the TEM analyses to assess the crystallinity of the low thickness zones.
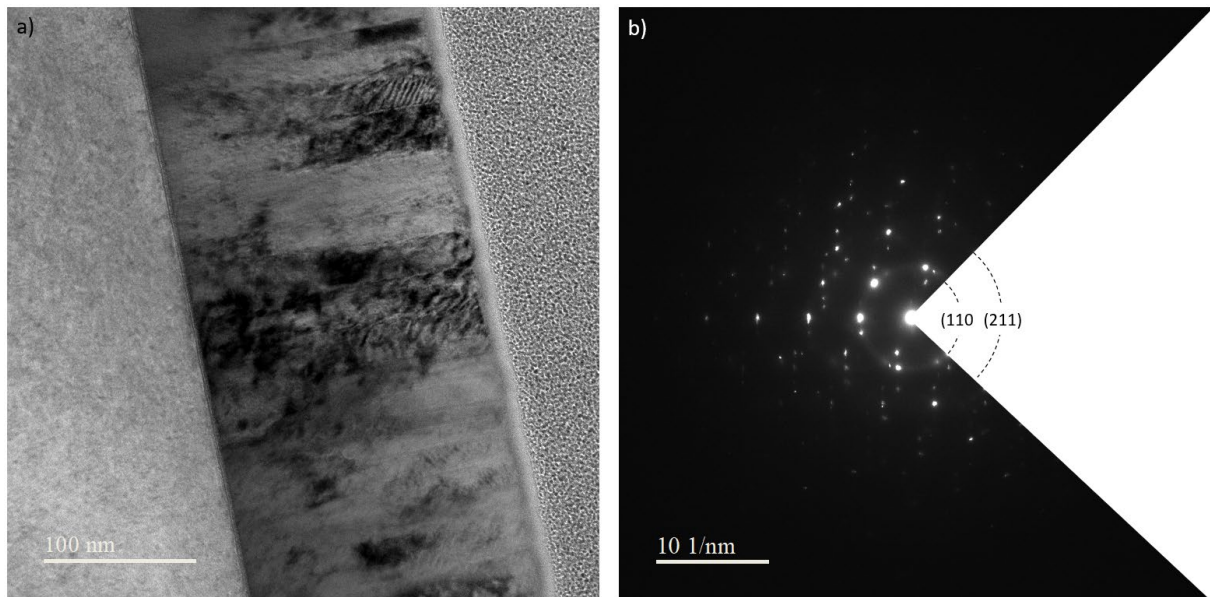
Fig. 5.8: TEM image (a) and electron diffraction (b) of a FIB-crystallized 176 nm-thick Zr-V thin film synthesized at a P*d product of 4.5 Pa.cm.

From these observations, we propose the following film growth model, that is depicted in Fig. 5.9 (d), and supported by the surface SEM micrographs shown in Fig. 5.9 (a-c). In the early growth stages, the film grows amorphous, and the first traces of crystalline nanocolumns were observed at 172 nm as observed in Fig. 5.9 (a). The nanocolumns are already elongated in a direction and form a small bundle that is constituted of a small number of nanocolumns. As the thickness increases, the compressive stress increases leading to more mechanical energy available that can be used for crystalline columns to grow alongside their neighbors in the same direction.

The reason for the emergence of new columns alongside existing columns is still not understood, but a parallel can be made with the pearlite growth in steels. During pearlite growth,

the growth of a Fe3C lamella creates chemically-favorable conditions for a ferrite lamella to grow in the same direction, resulting in a structure similar to what is observed in Fig. 5.9 (c). However, in the case of Zr-V thin films, with the high compressive stress in the films, we believe that the driving force for new columns growth is mechanical rather than chemical, but the result is the same: in the same grain, elongated columns grow in the same direction as their neighbors. Their lateral growth is only stopped when they encounter another grain, as can be seen in Fig. 5.9 (c) where there is a clear grain boundary between the grains.

As seen on the orientation cartography shown in Fig. 5.7 (b), each column can have a different orientation, as depicted in Fig. 5.9 (d). When the grains encounter, the amorphous layer beneath crystallizes with the predominant orientation among the bottom of the columns. Thus, different predominant orientations between adjacent grains can lead to different orientations in the crystallized zone, as shown the rightmost panel in Fig. 5.9 (d) where the crystallized amorphous layer on the left shows a different orientation (in pink) due to a different predominant orientation in the columns. For the dense zone that is flat on the surface, we believe that its crystallization occurs during the FIB processing.
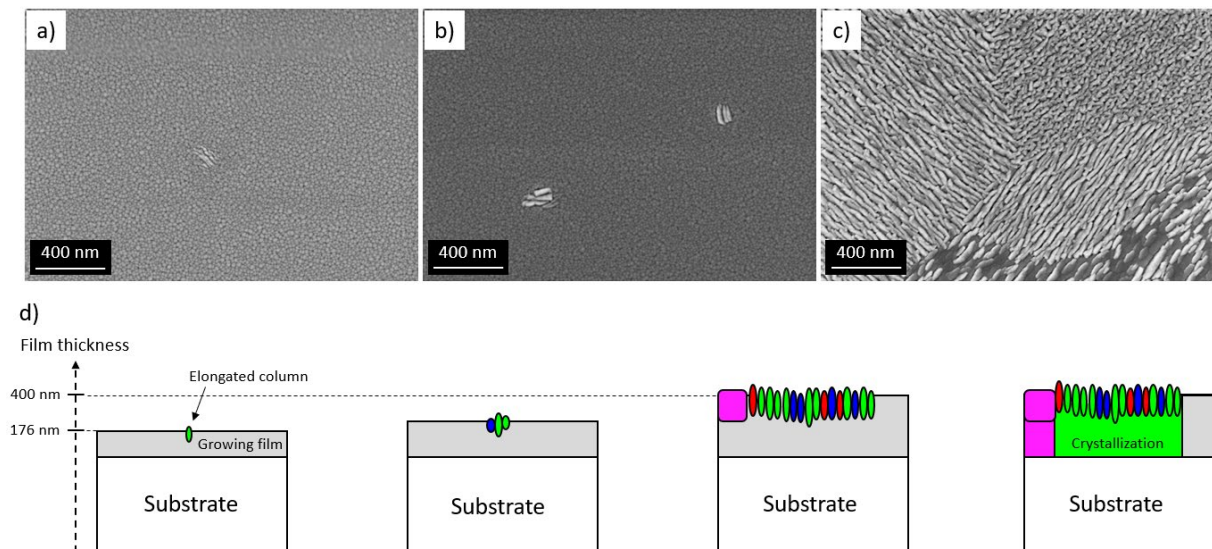
Fig. 5.9: SEM surface micrographs of Zr-V thin films grown at a P*d product of 4.5 Pa.cm and thicknesses 176 nm (a), 282 nm (b) and 400 nm (c), and model of the microstructure evolution with thickness (d). Each color corresponds to a crystallographic orientation, and grey corresponds to the amorphous phase.

To sum up, both the Zr-V thin films deposited at P*d products of 18 and 4.5 Pa.cm start out amorphous according to XRD analysis, and when a critical thickness is reached, nucleation of the crystalline phase occurs. At a higher pressure, the amorphous matrix is columnar and the crystalline regions are conical with a spherical cap on their surface, while at a lower pressure the amorphous phase is denser and the crystalline phase grows as elongated columns in the same direction, separated by grain boundaries. Interestingly, at a lower pressure we observe a crystallization of the amorphous part of the film, which was not reported for other Zr-based films. This crystallization could either be the result of latent heat of crystallization released during the phase transition at higher thicknesses giving enough energy for the amorphous layer to crystallize and explaining its large grains, or be the result of the FIB processing that crystallized the amorphous layer before TEM analysis. The stress evolution during growth seems comparable for the two pressures when stress is measured ex-situ for high pressure

conditions, and the phenomenon only exists in a given chemical composition range, even if this range differs when the pressure varies. With these observations, we believe that the mechanisms governing the amorphous-crystalline phase transition are comparable when the pressure changes, and understanding what happens during growth at lower pressure could help us gain precious insight transposable to higher pressure.

5.4 Possible origins of the crystallization in these films

Nucleation theory tells us that for nucleation to occur, an energy barrier has to be overcome. These thin films are no exception, and this energy barrier can be lowered or overcome by different mechanisms.

The nucleation rate N can be expressed in the form of an Arrhenius rate equation:

$$N = Ae^{-\frac{Q_n}{RT}} \tag{5.1}$$

With A the pre-exponential factor, Q_n the activation energy for nucleation or nucleation energy barrier. As noted in the previous chapters, it is observed in the case of our thin films that there is a critical thickness needing to be reached for nucleation to occur. This indicates that there is a time-dependent phenomenon that makes Q_n become of the order of RT, thus rendering nucleation possible. From this, two methods can achieve this result: (1) bringing enough energy to overcome the nucleation energy barrier, or (2) lowering the nucleation energy barrier.

Three main paths are considered for this to happen: thermally, chemically or mechanically. In this part, we will assess the plausibility of each of these contributions to be the origin for the crystallization in our thin films during growth.

5.4.1 Temperature-induced crystallization

The most widespread method to crystallize an amorphous thin film is by annealing after deposition. The high temperature allows overcoming the nucleation barrier, followed by a crystallization of the thin film. In our case, the temperature of the substrate is 28 °C when the film reaches 400 nm. The lower the temperature, the less likely it is that the crystallization is temperature-induced. Otherwise, when the surface crystallization occurs (between 272 and 400 nm), the latent heat released by the crystallization could be enough for the amorphous part of the film to crystallize thoroughly. Moreover, detecting a sudden increase in substrate temperature around these thicknesses could be a great hint that the amorphous sublayer crystallizes during growth. Such small variations in substrate temperature during deposition go against the temperature-induced crystallization. This renders the hypothesis of temperature-induced crystallization of these films unlikely.

It has to be noted that while the substrate temperature is monitored during deposition and used to obtain these conclusions, the film temperature and above all the film surface temperature are not measurable, and could be much higher than the aforementioned 28 °C when crystallization occurs. The maximum substrate temperature is reached at the end of the deposition of the 1462 nm thin film and is 37 °C.

5.4.2 Composition-induced crystallization

The thin films being deposited at a chemical composition between the amorphous and crystalline compositions, a change in chemical composition could well cause crystallization of the crystalline phase during growth. It has been shown for Zr-W thin films that increasing the W content in the films (i.e. getting closer to the crystalline composition) favors Zr(W) crystalline phase nucleation, going from grain-boundary nucleation to random nucleation.

Moreover, the critical thickness for nucleation lowers, and crystalline nuclei density increases [13]. This ease to nucleate when increasing the W content means that the nucleation energy barrier decreases, favoring nucleation.

If a local segregation during growth inducing a change in the chemical composition is the origin of nucleation in our thin films, this should be observable via EDS in TEM given the high spatial resolution of this technique. The results of the EDS in TEM analyses are shown in Fig. 5.10 (a-e). As can be seen in Fig. 5.10 (a, b) , for a P*d product of 18 Pa.cm with for instance a Zr-Cr thin film, the composition regarding Zr and Cr is not significantly different for the amorphous and crystalline phases. For thin films grown at a lower P*d product of 4.5 Pa.cm, take the example of a Zr-V thin film in Fig. 5.10 (c, d), again no significant difference in chemical composition is observed between the crystallized amorphous layer, the columns and the dense flat zone. Moreover, an EDS cartography was performed in the TEM and the results are shown in Fig. 5.10 (e). No segregation of any element is observed throughout the film, and no significant difference is found between the different microstructures. As explained, whether is it for a P*d product of 18 or 4.5 Pa.cm, the chemical composition seems to be homogeneous throughout the films, considering the incertitude inherent to the EDS technique. While an increase in the V content in the film eases the nucleation of the crystalline phase (i.e. lowers the nucleation energy barrier), no significant change in chemical composition is observed throughout the film, which discredits the local segregation hypothesis.
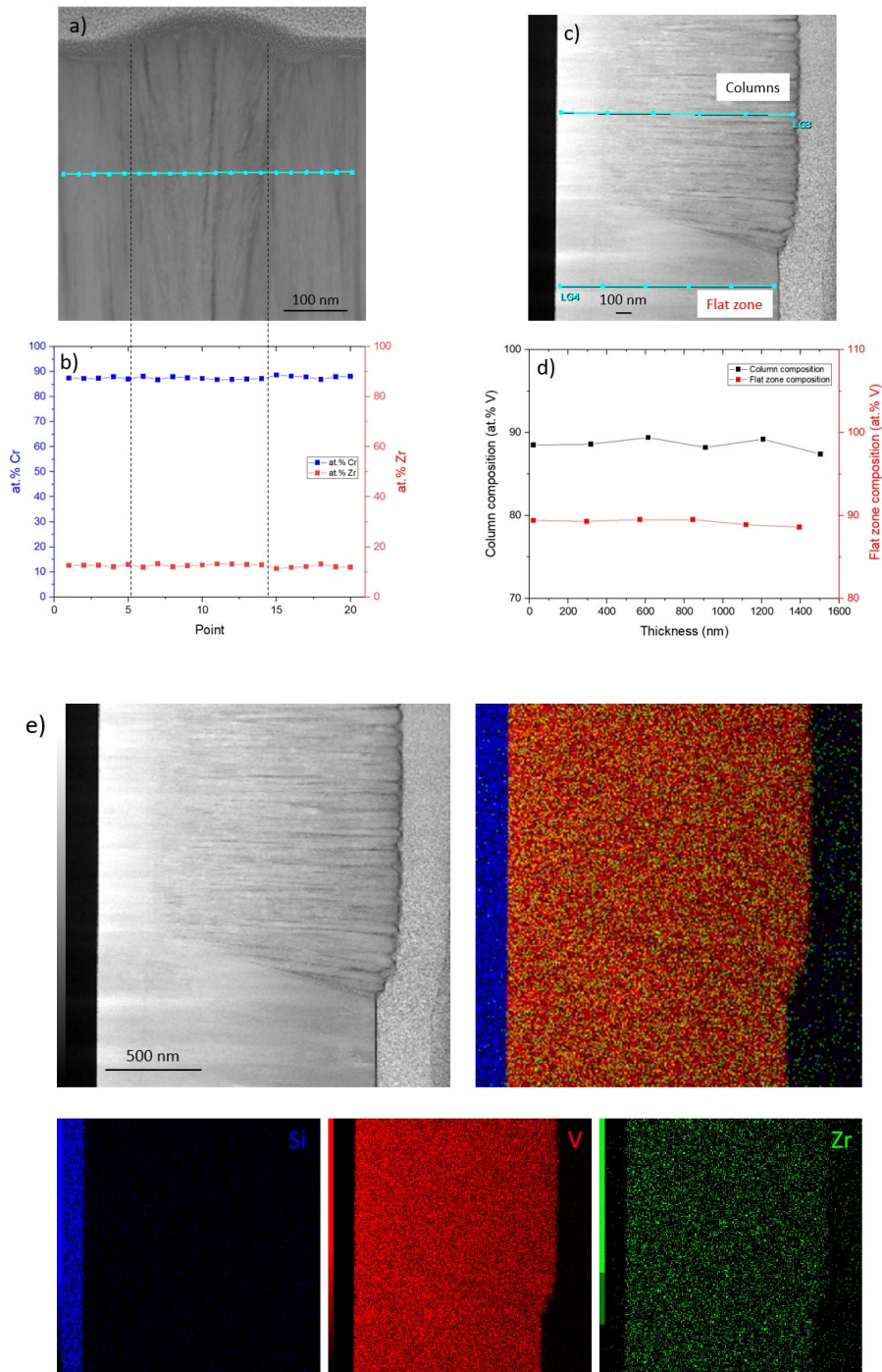
Fig. 5.10: Bright field TEM image of a dual-phase Zr-Cr thin film deposited at a P*d product of 18 Pa.cm (a) and the results of the EDS quantification on the cyan line (b). Bright field TEM image of a dual-phase Zr-V thin film deposited at a P*d product of 4.5 Pa.cm (c) and the results of the EDS quantifications on the cyan lines (d), and EDS cartography on the same Zr-V film showing Si, V and Zr signals (e). The symbols on the cyan lines in (a, c) are the locations where EDS measurements have been performed.

5.4.3 Stress-induced crystallization

The last crystallization path that will be covered is through mechanical energy. Indeed, an uneven stress distribution throughout the film causes local changes of the strain energy and effectively decreases the nucleation energy barrier [143,144]. Studies using molecular dynamics simulation have already reported that stress could induce crystallization for amorphous metals or thin films. Even at low temperatures that restrict the ordering of atoms, from 10 K to 300 K, it has been reported that nano-size Ni specimens could crystallize when a compressive stress is applied [145]. Deformation-induced crystallization of an AlFe metallic glass also has been found with simulation at 50 K [146]. In this study, the nucleated crystalline phase has the same chemical composition as the amorphous phase that it transitions from. Another study shown through simulation that stress enhances crystallization of Ni thin films, and that the crystallization serves as a deformation mechanism [147].

The same findings have also been reported experimentally, for instance in Ge-doped Sb thin films the application of a compressive stress of 70 MPa led to a 60-fold faster crystal growth rate perpendicular to the applied stress. They attributed the fact that crystallization is aided by a compressive stress to the higher density of the crystalline phase [148]. In-situ stress measurements in $Mo_{1-x}Si_x$ thin films (with $x \leq 20$ at.%) revealed the same stress behavior during growth as what is presented in this chapter [149]. In Fig. 5.11 (a) are shown the stress measurements during growth of their thin films with different chemical compositions. They observed the crystallization of their thin films during growth to occur after a critical thickness has been reached, and this thickness depends on the chemical composition of the film. This thickness delay can be observed on the stress-thickness curves, where increasing the Si content delays the crystallization thickness until it reaches a point where crystallization no longer occurs. They reported that the nucleation barrier increases with the Si content, the incorporation of Si

in bcc Mo lattice being energetically unfavorable. These stress-thickness curves resemble the ones obtained for our Zr-V films and reported in this chapter (see Fig. 5.4).
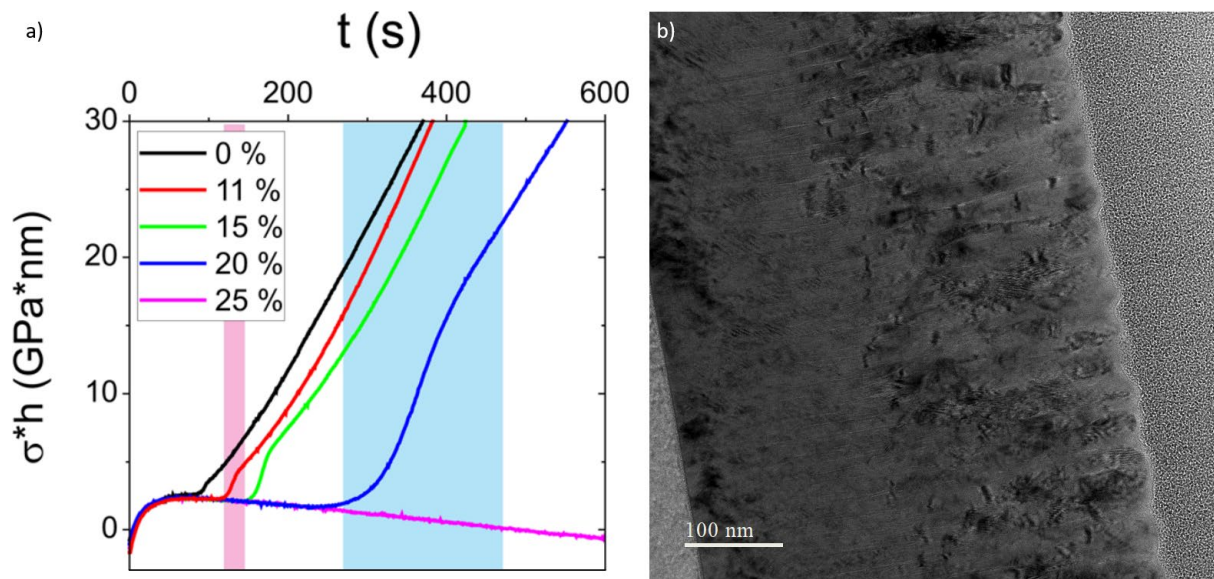
Fig. 5.11: In-situ stress measurements during $Mo_{1-x}Si_x$ thin films (a) with x written in the legend of the graph, from Ref. [149], and TEM image showing the thickness at which the microstructural change is observed for the 400 nm Zr-V thin film deposited at a P*d product of 4.5 Pa.cm (b).

In the case of our Zr-V thin films, the growth of an amorphous phase is associated with a constant compressive stress buildup in the films. On the other hand, the growth of the crystalline phase goes along a constant tensile stress buildup. For the thin film with an intermediate composition, a compressive stress is first observed, then a change in slope is observed at ~180 nm as a tensile component of the stress develops and at ~400 nm the final tensile slope is reached. Interestingly, as shown in Fig. 5.11 (b), a microstructural change is observed at 183 nm, which coincides with the stress-thickness slope change around 180 nm. Above this thickness, polycrystalline columns start growing on top of the denser amorphous layer, as was confirmed with the phase cartography in TEM. This suggests that the nucleation

of the crystallite phase begins when 180 nm thickness is reached. However, the absence of sudden change in internal stress above 300 nm suggests that the crystallization of the amorphous layer does not happen during growth, but rather due to the preparation of the lamella for TEM analyses.

At a low pressure the higher energy of the arriving atoms to the substrate results in a higher adatom surface diffusion, and the nucleation is followed by a lateral growth, and the following deposited layers contribute to the vertical growth of the crystalline grains, resulting in laterally large grains. At a higher pressure, the lower adatom surface diffusion does not allow this fast lateral crystal growth, and a crystalline nucleus grows as a cone surrounded by amorphous matter.

5.5 Chapter conclusions

Following a previous study on residual stress in dual-phase Zr-based thin films, we conducted in-situ stress measurements during growth of Zr-based thin films deposited at a P*d product of 18 and 4.5 Pa.cm, and compared the results with the reported ex-situ stress measurements. In-situ and ex-situ stress measurements differ greatly, and we explained that it was caused by relaxation, moisture adsorption and film oxidation after deposition. To overcome this difference, we sputtered Zr-V thin films at a lower pressure, which resulted in a change in crystalline regions morphology and the discovery of a novel film microstructure. The stress measurements during growth of these films show that the stress dynamics of amorphous and crystalline phase are different, and that a film with the right composition could begin to grow amorphous and undergo a phase transition to a crystalline phase with increasing thickness. A model is proposed to explain the growth of the elongated crystallites and the crystallization of the amorphous layer during growth. The amorphous samples were crystallized by FIB

processing, suggesting that this layer crystallizes easily. The TEM images show that the microstructure change is thickness-coherent with the stress change during growth. Finally, we delved into the possible nucleation pathways and showed that a close link exists between stress and crystallization in these dual-phase Zr-based thin films.

General conclusions

The aim of this thesis was to delve deeper into the investigation of the phenomenon of competitive growth between the amorphous and crystalline phases during sputter deposition of Zr-based thin films, and to show the potential of these thin films for antibacterial applications.

It has been shown that this competitive growth also occurs in Zr-Cr and Zr-V thin films. While for Zr-Cr the phenomenon is only observed in a narrow range of chemical composition (less than 5 at.% Cr), it was shown that the competitive growth could be observed for a wide range of deposition rates from 5 up to 63 nm/min, indicating its resilience against changes in deposition conditions. Is was also shown that changing the deposition rate results in a change of geometrical features in the crystalline cones, i.e. the number and diameter of nanocolumns in the cones, making the deposition rate an interesting lever to further control the growth of these films, along with the chemical composition and thickness. As for Zr-V, the chemical composition where the competitive growth can be observed is wider, around 6 at.% V. It was shown that the geometrical features of the crystalline cones depended both on the sputtered material and the deposition conditions, as changing these parameters induces variations in the nucleation kinetics of the nanocolumns as well as their lateral growth.

The thin films have been given bactericidal properties via the deposition of a thin Cu coating above their surface. Our thin films showed antibacterial efficiency against both E. Coli and B. Subtilis, which are respectively Gram-negative and Gram-positive bacteria. Against E. Coli, all our Cu-coated Zr-V thin films showed a higher efficiency than our Cu coupon reference after 120 min exposure. Against B. Subtilis only the thin films with a low surface coverage by the crystalline phase showed better results than both other films and the reference.

The close link between the evolution of the internal stress during growth and the film microstructure has been reported. It was shown that the thin films synthesized at 2 Pa do not follow the same stress evolution in-situ and ex-situ. When sputtering these films at a lower working pressure, a novel film structure is observed and the in-situ stress monitoring becomes more relevant. We showed that the stress dynamics of the amorphous and crystalline phases differ, and observed that the internal stress in the film changes along with the crystallization of the film. TEM images associated with stress change are coherent with the microstructural changes in the film, and presented the possible nucleation pathways for the crystalline phase during growth. We also proposed a model to explain the growth of the elongated crystallites and the crystallization of the amorphous layer during growth.

Perspectives

- While the bactericidal effect of the Cu-coated Zr-V thin films has been assessed, the question of the bacterial adhesion still remains. While the quantification of the antibacterial adhesion is a challenge, some techniques such as bacterial AFM exist. Solving this issue could help us gain insights on the dynamics during the antibacterial tests.

- Based on the similarities in terms of surface morphology between the crystalline regions in Zr-V thin films and the materials that have been reported to mechanically rupture bacterial cells by contact, our Zr-V thin films could also exhibit this interesting property. Thus, a bacterial viability test for a longer time period coupled with bacteria staining to differentiate dead and adhered bacteria could help us test this hypothesis.

- Even though our antibacterial thin films have been synthesized in a bottom-up approach with one main step being film deposition and one additional step being the Cu coating, one improvement can still be done. In fact, the synthesis of dual-phase Zr-Cu thin films could result in films with a great antibacterial efficiency in only one step. However, despite our efforts to synthesize such films and the wide range of deposition parameters explored (wide composition, temperature, P*d product ranges), the amorphous-crystalline competitive growth is still nowhere to be seen.

- When synthesizing Zr-V thin films at low working pressures, different peculiar film morphologies have been identified, as shown in Fig. P.1 (a-f). At this pressure, between the amorphous and crystalline compositions are found 3 different film morphologies. Between 85.5 and 86 at.% V the crystalline regions still seem to grow as cones with a different surface morphology as seen in Fig. P.1 (a, b). When the V content is increased in the range 87 – 88 at.% V, the morphology becomes the one studied in **Chapter 5** as shown in Fig. P.1 (c, d), but when increasing further the V content, the deposited films with 89 – 90 at.% V show a different morphology as shown in Fig. P.1 (e, f), where the flat zones

(that are circular at this composition) are surrounded by concentric elongated columns. These elongated columns bridge the flat zones together, the other zones consisting of circular columns. Delving into these multiple morphologies could give insights on the crystallization dynamics.
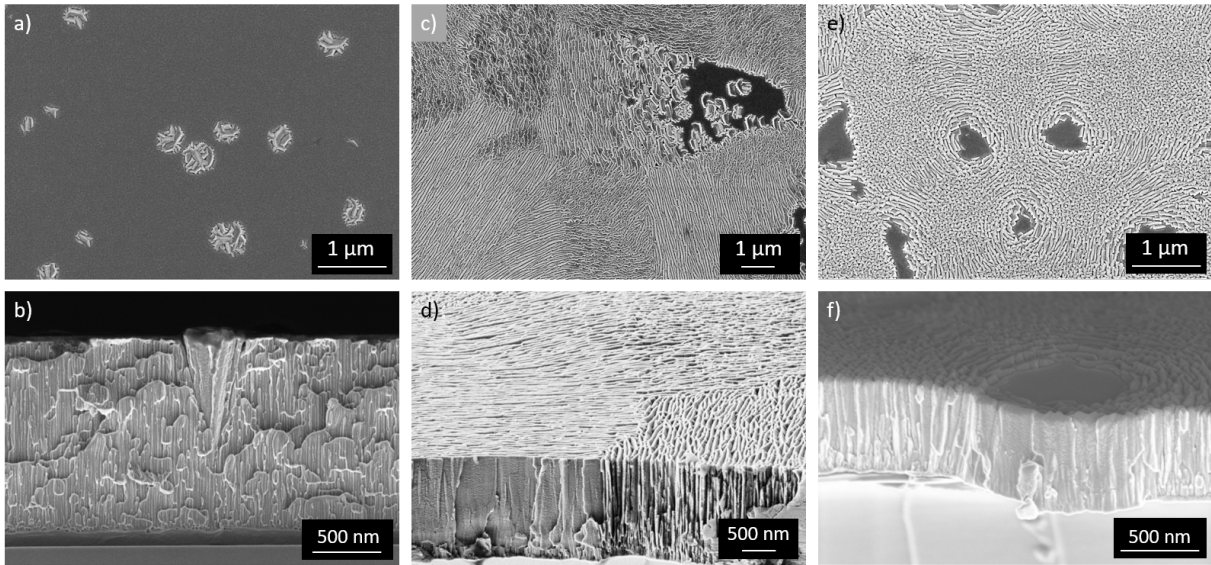
Fig. P.1: SEM surface and cross-section micrographs of Zr-V samples synthesized at a 0.5 Pa working pressures with chemical compositions 86.0 at.% V (a, b), 87.5 at.% V (c, d) and 90.1 at.% V (e, f). The cross-section micrographs (d) and (f) were acquired with a tilted substrate holder to view surface and cross-section together.

- Depending on the sputtered material and the deposition pressure, the nanocolumns in the crystalline regions can exhibit different microstructures, shown in Fig. P.2 (a-d). When the surface mobility is low, such as for the Zr-W, Zr-Cr and Zr-Mo systems at 2 Pa, nanocolumns constituting the cones have rounded tops as seen in Fig. P.2 (a). This is similar to what is expected from zone I a or I b in the structure zone model of Mahieu et al. [24]. When the surface mobility is higher such as for the Zr-V system at 2 Pa, nanocolumns constituting the cones are faceted and exhibit a preferential orientation, despite the fact that

they appear separated by voids, as seen in Fig. P.2 (b). This resembles the microstructure of zone T (zone II) in the structure zone model of Mahieu et al. (Thornton) [23,24]. When the nucleation barrier is very low, such as for the Zr-Mo system at 0.5 Pa, recrystallization of the cones may occur during growth triggered by the release of the latent heat and can lead to monocrystalline cones, as shown in Fig. P.1 (d). The latent heat has been calculated using ThermoCalc for each system at their crystallization temperature:

$$L_{Zr-Cr} = -0.5 kJ.mol^{-1} \qquad L_{Zr-V} = -16.5 kJ.mol^{-1}$$

$$L_{Zr-Mo} = -10.2 kJ.mol^{-1} \qquad L_{Zr-W} = -17.5 kJ.mol^{-1} \qquad (P.1)$$

The resulting microstructure of the crystalline region is close to that of zone II (zone III) in the structure zone model of Mahieu et al. (Thornton). For the Zr-V system at 0.5 Pa shown in Fig. P.2 (c), the resulting microstructure seems intermediate to Zr-V at 2 Pa and Zr-Mo at 0.5 Pa. In the end, the predominant parameter for the crystalline regions and columns shape would be the surface mobility, while for the cone angle it would be the nanocolumn nucleation density. To fully understand the parameters involved and how they affect the microstructure, further studies are needed, in particular regarding the wide variety of microstructures hosting elongated columns arranged in different ways, as illustrated in Fig. P.1 (e, f).
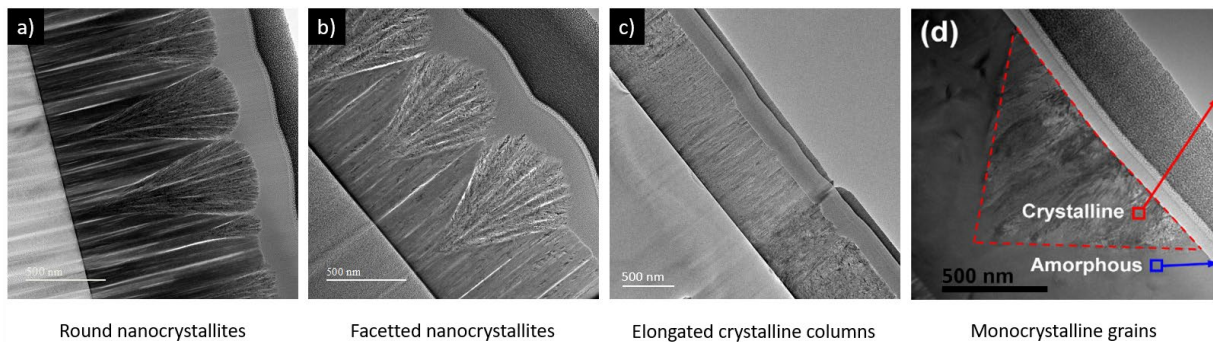
Fig. P.2: TEM images of a Zr-Cr (a), a Zr-V (b) thin films synthesized at 2 Pa, and TEM images of Zr-V (c) and Zr-Mo (d) thin films synthesized at 0.5 Pa. The morphology of the crystalline

phase changes depending on the sputtered material and the deposition pressure. (d) is adapted from Ref. [14]. Below the figures is written the shape of the nanocolumns in the crystalline regions.

Appendixes

Antibacterial properties: Effect of time on the copper coating

In **Chapter 4** was discussed the antibacterial efficiency of the Cu-coated Zr-V thin films. While these results were obtained in 2023, a preliminary study was conducted in 2021 on the 0 % to 80 % coverage films, about 1 month after thin films synthesis. The results of the wet plating test from this preliminary study are shown in Fig. A.1. While the results after 30 and 60 min exposure times are the same as presented in **Chapter 4**, this is not true after a 120 min exposure time. Here, the antibacterial efficiency increases quasi-linearly with the surface coverage by the crystalline phase. When comparing these results with those presented in **Chapter 4**, it can be seen that between 2021 and 2023, the antibacterial efficiency was reduced by a factor 5 for the 20 % and 60 % coverage films, while it has increased by a factor 2 to 10 for the other films. This increase in antibacterial efficiency for some films between the two sets of experiments should not come from oxidation alone, but other phenomena might take place here. The bacteria being held in the fridge for some time, it is possible that they were more likely to die or to be damaged upon contact with the copper surface during the first set of experiments. Also, if oxidation took place with different degrees on each sample, this could lead to different killing kinetics, and different adhesion dynamics on the films surface, both of which lead to a change in CFU reduction rate.
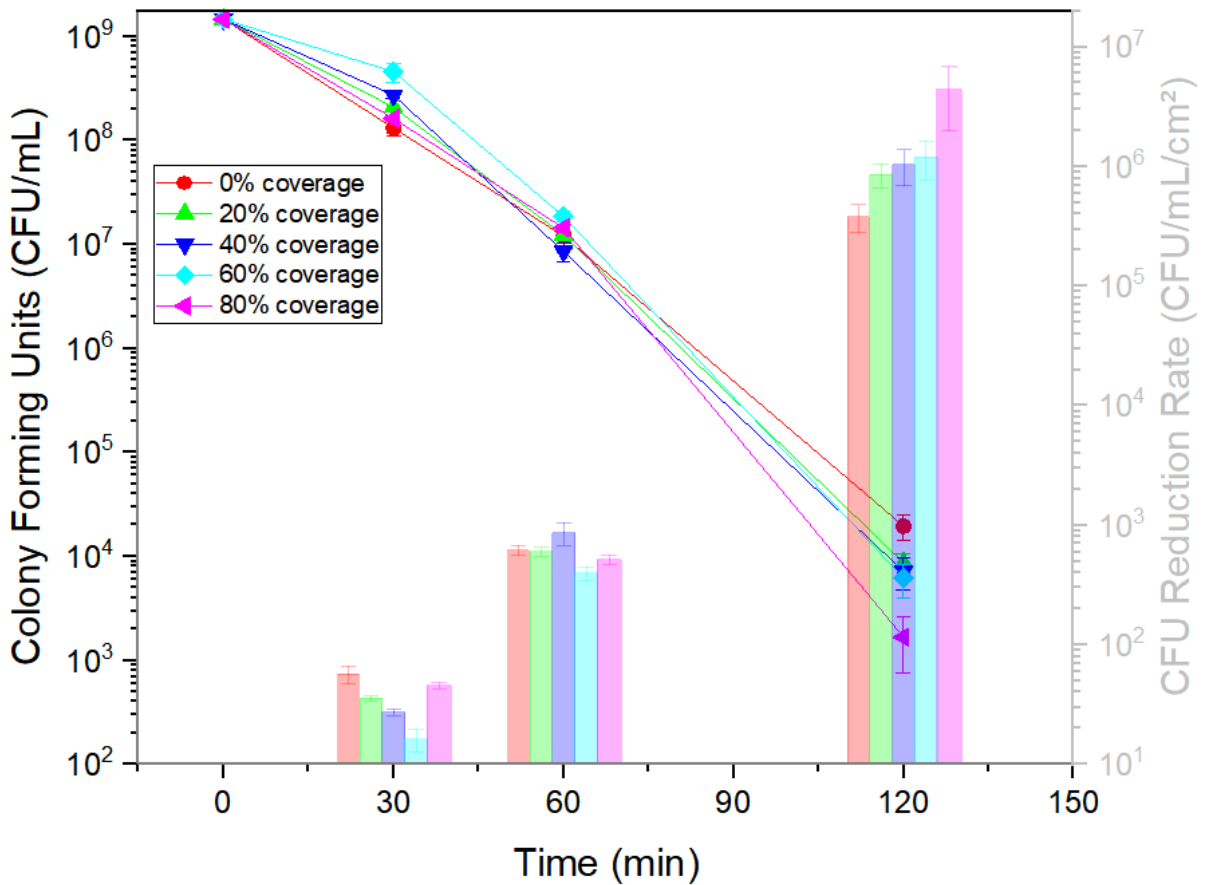
Fig. A.1: Results of the wet plating test with E. Coli for Cu-coated Zr-V thin films showing from 0 % to 80 % surface coverage by the crystalline phase, after 3 days of incubation. The vertical scale is logarithmic, the plotted lines show the number of bacteria that survived after exposure to the surface, while the columns show the bacterial reduction rate.

On the orientation of the different zones in the films synthesized at low pressure

In **Chapter 5** was proposed a model explaining the growth of the elongated crystalline columns over the amorphous matrix and subsequent crystallization of this amorphous layer underneath them. This model was partly based on the results from an orientation cartography on a Zr-V thin film. Here is presented an orientation cartography performed on a different zone of the film. The film can be seen in Fig. A.1 (a) with a flat zone on the left and some conical crystallites that nucleated during growth of the film, and another zone on the right with elongated columns. The difference with the image shown in **Chapter 5** is that here, instead of the columns being parallel to the point of view, they are now perpendicular. Again, we observe a single orientation in the whole flat surface, with some degrees of disorientation. For the column, the software seems more confident in the result given, and the brighter zones have the same orientation, leading us to believe that each column has a single orientation. Here, the crystallized zone below the column does not seem to have the same orientation as the column; this is expected to occur as explained by the growth model in **Chapter 5**.
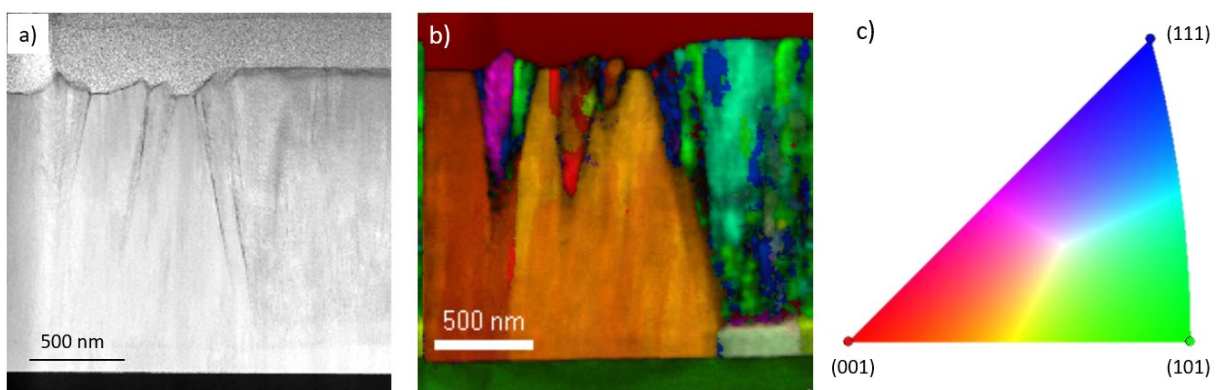
Fig. A.2: Bright-field TEM image (a) and combination of the confidence index and orientation cartography (b) of a 1462 nm-thick Zr-V thin film synthesized at a P*d product of 4.5 Pa.cm, and colored orientation triangle to represent the orientation of grains (c).

Bibliography

[1]   X. Yang, F. Wang, W. Wang, S. Liu, Y. Chen, H. Tang, Comparison of two-step surface treatment on surface roughness and corrosion resistance of TC4 alloy parts prepared by SLM and SEBM, J. Alloys Compd. 921 (2022) 165929. https://doi.org/10.1016/j.jallcom.2022.165929.

[2]   Y. Ma, L. Li, J. Qian, W. Qu, R. Luo, F. Wu, R. Chen, Materials and structure engineering by magnetron sputtering for advanced lithium batteries, Energy Storage Mater. 39 (2021) 203–224. https://doi.org/10.1016/j.ensm.2021.04.012.

[3]   A. Garcia-Giron, J.M. Romano, Y. Liang, B. Dashtbozorg, H. Dong, P. Penchev, S.S. Dimov, Combined surface hardening and laser patterning approach for functionalising stainless steel surfaces, Appl. Surf. Sci. 439 (2018) 516–524. https://doi.org/10.1016/j.apsusc.2018.01.012.

[4]   M. Tabish, M.U. Malik, M.A. Khan, G. Yasin, H.M. Asif, M.J. Anjum, W.Q. Khan, S. Ibraheem, T.A. Nguyen, Y. Slimani, M.T. Nazir, Construction of NiCo/graphene nanocomposite coating with bulges-like morphology for enhanced mechanical properties and corrosion resistance performance, J. Alloys Compd. 867 (2021) 159138. https://doi.org/10.1016/j.jallcom.2021.159138.

[5]   G. Purcek, H. Yanar, M. Demirtas, D. V. Shangina, N.R. Bochvar, S. V. Dobatkin, Microstructural, mechanical and tribological properties of ultrafine-grained Cu–Cr–Zr alloy processed by high pressure torsion, J. Alloys Compd. 816 (2020) 152675. https://doi.org/10.1016/j.jallcom.2019.152675.

[6]   J. Zhu, X. Cheng, L. Zhang, X. Hui, Y. Wu, H. Zheng, Z. Ren, Y. Zhao, W. Wang, S. Zhu, X. Wang, Microstructures, wear resistance and corrosion resistance of CoCrFeNi high entropy alloys coating on AZ91 Mg alloy prepared by cold spray, J. Alloys Compd. 925 (2022) 166698. https://doi.org/10.1016/j.jallcom.2022.166698.

[7]   D.W. Müller, S. Lößlein, E. Terriac, K. Brix, K. Siems, R. Moeller, R. Kautenburger, F. Mücklich, Increasing Antibacterial Efficiency of Cu Surfaces by targeted Surface Functionalization via Ultrashort Pulsed Direct Laser Interference Patterning, Adv. Mater. Interfaces. 8 (2021). https://doi.org/10.1002/admi.202001656.

[8]   H. Ji, M.C. Zhao, B. Xie, Y.C. Zhao, D. Yin, C. Gao, C. Shuai, A. Atrens, Corrosion and antibacterial performance of novel selective-laser-melted (SLMed) Ti-xCu biomedical alloys, J. Alloys Compd. 864 (2021) 158415. https://doi.org/10.1016/j.jallcom.2020.158415.

[9]   C.B. Yi, Y.X. Yuan, L. Zhang, Y.H. Jiang, Z.Y. He, Antibacterial Ti-35Nb-7Zr-xCu alloy with excellent mechanical properties generated with a spark plasma sintering method for biological applications, J. Alloys Compd. 879 (2021) 160473. https://doi.org/10.1016/j.jallcom.2021.160473.

[10]   J.H. Kim, E. Akiyama, H. Habazaki, A. Kawashima, K. Asami, K. Hashimoto, The corrosion behavior of sputter-deposited amorphous chromium-zirconium alloys in 6 M HCl solution, Corros. Sci. 34 (1993) 1817–1827. https://doi.org/10.1016/0010-938X(93)90019-D.

[11]   X.Y. Li, E. Akiyama, H. Habazaki, A. Kawashima, K. Asami, K. Hashimoto, The corrosion behavior of sputter-deposited amorphous Mo-Zr alloys in 12 M HCl, Corros. Sci. 41 (1999) 1849–1869. https://doi.org/10.1016/S0010-938X(99)00019-0.

[12]   D. Horwat, M. Dehmas, E. Aubry, J. Zollinger, S. Migot, J.F. Pierson, Properties of nanocrystalline and nanocomposite WxZr1-x thin films deposited by co-sputtering, Intermetallics. 17 (2009) 421–426. https://doi.org/10.1016/j.intermet.2008.11.020.

[13]   A. Borroto, A.C. García-Wong, S. Bruyère, S. Migot, D. Pilloud, J.F. Pierson, F. Mücklich, D. Horwat, Composition-driven transition from amorphous to crystalline films enables bottom-up design of functional surfaces, Appl. Surf. Sci. 538 (2021)

148133. https://doi.org/10.1016/j.apsusc.2020.148133.

[14] A. Borroto, S. Bruyère, S. Migot, J.F. Pierson, T. Gries, F. Mücklich, D. Horwat, Controlling surface morphology by nanocrystalline/amorphous competitive self-phase separation in thin films: Thickness-modulated reflectance and interference phenomena, Acta Mater. 181 (2019) 78–86. https://doi.org/10.1016/j.actamat.2019.09.036.

[15] A. Borroto, S. Bruyère, S. Migot, J.F. Pierson, F. Mücklich, D. Horwat, Growth kinetics and origin of residual stress of two-phase crystalline-amorphous nanostructured films, J. Appl. Phys. 129 (2021). https://doi.org/10.1063/5.0044029.

[16] G. Schelcher, Le transfert de films : vers une intégration hétérogène des micro et nanosystèmes, Thesis. (2015).

[17] M. Aiempanakit, P. Larsson, K. Sarakinos, Hysteresis and process stability in reactive high power impulse magnetron sputtering of metal oxides, Thin Solid Films. 519 (2011) 7779–7784. https://doi.org/10.1016/j.tsf.2011.06.021.

[18] C. Garcia-Rosales, J. Laszlo, Threshold energy for sputtering and its dependence on angle of incidence, Nucl. Inst. Methods Phys. Res. B. (1993). https://doi.org/10.1016/0168-583X(93)95913-P.

[19] J. Bohdansky, A universal relation for the sputtering yield of monatomic solids at normal ion incidence, Nucl. Inst. Methods Phys. Res. B. (1984). https://doi.org/https://doi.org/10.1016/0168-583X(84)90271-4.

[20] H.C. Vasconcelos, T. Eleuterio, M.G. Meirelles, S. Sério, TiO2 Nanocoatings on Natural Fibers by DC Reactive Magnetron Sputtering, IntechOpen. (2023). https://doi.org/DOI: 10.5772/intechopen.110673.

[21] P.J. Kelly, R.D. Arnell, Magnetron sputtering : a review of recent developments and applications, Vacuum. 56 (2000) 159–172. https://doi.org/https://doi.org/10.1016/S0042-207X(99)00189-X.

[22] M.B. A., Study of the structure and properties of thick vacuum condensates of nickel, Titanium, Tungsten, Aluminium Oxide and Zirconium Dioxide, Phys. Met. Met. 28 (1969) 83–90. https://cir.nii.ac.jp/crid/1571698601163070336.bib?lang=ja (accessed June 21, 2023).

[23] J.A. Thornton, Influence of Apparatus Geometry and Deposition Conditions on the Structure and Topography of Thick Sputtered Coatings., J Vac Sci Technol. 11 (1974) 666–670. https://doi.org/10.1116/1.1312732.

[24] S. Mahieu, P. Ghekiere, D. Depla, R. De Gryse, Biaxial alignment in sputter deposited thin films, Thin Solid Films. 515 (2006) 1229–1249. https://doi.org/10.1016/j.tsf.2006.06.027.

[25] A. Anders, A structure zone diagram including plasma-based deposition and ion etching, Thin Solid Films. 518 (2010) 4087–4090. https://doi.org/10.1016/j.tsf.2009.10.145.

[26] J. Koh, Y. Lee, H. Fujiwara, C.R. Wronski, R.W. Collins, J. Koh, Y. Lee, H. Fujiwara, C.R. Wronski, R.W. Collins, Optimization of hydrogenated amorphous silicon $p-i-n$ solar cells with two-step i layers guided by real-time spectroscopic ellipsometry, Appl. Phys. Lett. 1526 (2006) 6–9. https://doi.org/10.1063/1.122194.

[27] R.W. Collins, A.S. Ferlauto, G.M. Ferreira, C. Chen, J. Koh, R.J. Koval, Y. Lee, J.M. Pearce, C.R. Wronski, Evolution of microstructure and phase in amorphous , protocrystalline , and microcrystalline silicon studied by real time spectroscopic ellipsometry, Sol. Energy Mater. Sol. Cells. 78 (2003) 143–180. https://doi.org/10.1016/S0927-0248(02)00436-1.

[28] C.W. Teplin, C. Jiang, P. Stradins, H.M. Branz, C.W. Teplin, C. Jiang, P. Stradins, H.M. Branz, Cone kinetics model for two-phase film silicon deposition Cone kinetics model for two-phase film silicon deposition, Appl. Phys. Lett. 093114 (2013) 2006–

2009. https://doi.org/10.1063/1.2891087.

[29]   L.K. Gautam, Spectroscopic Ellipsometry Studies of Thin Film Si:H Materials in
       Photovoltaic Applications from Infrared to Ultraviolet, Thesis. (2016).

[30]   R. Gago, M. Vinnichenko, A. Redondo-Cubero, Z. Czigány, L. Vázquez, Surface
       morphology of heterogeneous nanocrystalline rutile/amorphous anatase TiO2 films
       grown by reactive pulsed magnetron sputtering, Plasma Process. Polym. 7 (2010) 813–
       823. https://doi.org/10.1002/ppap.200900182.

[31]   K. Nakada, J. Irikawa, S. Miyajima, M. Konagai, Silicon heterojunction solar cells with
       high surface passivation quality realized using amorphous silicon oxide films with
       epitaxial phase, Jpn. J. Appl. Phys. 052303 (2015).
       https://doi.org/http://dx.doi.org/10.7567/JJAP.54.052303.

[32]   H. Fujiwara, M. Kondo, A. Matsuda, Stress-Induced Nucleation of Microcrystalline
       Silicon from Amorphous Phase, Jpn. J. Appl. Phys. 2821 (2002).
       https://doi.org/10.1143/JJAP.41.2821.

[33]   H. Fujiwara, Y. Nasuno, M. Kondo, A. Matsuda, Low-Temperature Formation of
       Polycrystalline Silicon and Its Device Application, Solid State Phenom. 93 (2003) 99–
       108. https://doi.org/10.4028/www.scientific.net/SSP.93.99.

[34]   H. Fujiwara, M. Kondo, A. Matsuda, Nucleation mechanism of microcrystalline silicon
       from the amorphous phase, J. Non. Cryst. Solids. 338–340 (2004) 97–101.
       https://doi.org/10.1016/j.jnoncrysol.2004.02.029.

[35]   A. Matsuda, Amorphous and Microcrystalline Silicon, Springer Handb. Electron.
       Photonic Mater. (2017) 573–587. https://doi.org/10.1007/978-3-319-48933-9.

[36]   A. Matsuda, Formation kinetics and control of microcrystallite in μc-Si:H from glow
       discharge plasma, J. Non. Cryst. Solids. 60 (1983) 767–774.
       https://doi.org/https://doi.org/10.1016/0022-3093(83)90284-3.

[37] A. Matsuda, Growth mechanism of microcrystalline silicon obtained from reactive plasmas, Thin Solid Films. 337 (1999) 4–9. https://doi.org/https://doi.org/10.1016/S0040-6090(98)01165-1.

[38] P. Zeman, S. Haviar, M. Červená, Self-formation of dual glassy-crystalline structure in magnetron sputtered W–Zr films, Vacuum. 187 (2021). https://doi.org/10.1016/j.vacuum.2021.110099.

[39] L.R. Shaginyan, Y.J. Kim, J.G. Han, N. V Britun, J. Musil, I. V Belousov, Novel model for film growth based on surface temperature developing during magnetron sputtering, Surf. Coat. Technol. 202 (2007) 486–493. https://doi.org/10.1016/j.surfcoat.2007.06.016.

[40] V. Brien, P. Miska, B. Bolle, P. Pigeat, Columnar growth of ALN by r.f. magnetron sputtering: Role of the {1 0 Γ 3} planes, J. Cryst. Growth. 307 (2007) 245–252. https://doi.org/10.1016/j.jcrysgro.2007.06.013.

[41] V. Kolkovsky, J.U. Schmidt, S. Döring, Electrical and structural properties of direct current magnetron sputtered amorphous TiAl thin films, Thin Solid Films. 669 (2019) 169–173. https://doi.org/10.1016/j.tsf.2018.10.033.

[42] M.J. Burch, Microstructural Evolution and Domain Structures of Flux-grown Ferroelectric Thin Films, Thesis. (2016).

[43] Y. Zhang, S. Li, R. Gan, T. Zhou, D. Xu, H. Li, Impacts of Gut Bacteria on Human Health and Diseases, Int. J. Mol. Sci. (2015) 7493–7519. https://doi.org/10.3390/ijms16047493.

[44] S.M. Jandhyala, R. Talukdar, C. Subramanyam, H. Vuyyuru, M. Sasikala, Role of the normal gut microbiota, World J. Gastroenterol. 21 (2015) 8787–8803. https://doi.org/10.3748/wjg.v21.i29.8787.

[45] K.A. Glatter, P. Finkelman, History of the Plague: An Ancient Pandemic for the Age of

COVID-19, Am. J. Med. 134 (2021) 176–181.

https://doi.org/10.1016/j.amjmed.2020.08.019.

[46] S. Watts, A mini review on technique of milk pasteurization, J. Pharmacogn.

Phytochem. 5 (2016) 99–101.

[47] P. Singh, I. Potlia, S. Malhotra, Hand Sanitizer an Alternative to Hand Washing — A

Review of Literature, J. Adv. Oral Res. (2020).

https://doi.org/10.1177/2320206820939403.

[48] M.I. Hutchings, A.W. Truman, B. Wilkinson, Antibiotics : past , present and future,

Curr. Opin. Microbiol. 51 (2020) 72–80. https://doi.org/10.1016/j.mib.2019.10.008.

[49] M. Frieri, K. Kumar, A. Boutin, Antibiotic resistance, J. Infect. Public Health. 10

(2017) 369–378. https://doi.org/10.1016/j.jiph.2016.08.007.

[50] J.L. Martínez, F. Baquero, Emergence and spread of antibiotic resistance : setting a

parameter space, Ups. J. Med. Sci. (2014) 68–77.

https://doi.org/10.3109/03009734.2014.901444.

[51] A.J. Alanis, Resistance to Antibiotics : Are We in the Post-Antibiotic Era ?, Arch. Med.

Res. 36 (2005) 697–705. https://doi.org/10.1016/j.arcmed.2005.06.009.

[52] L.F. Camarillo-guerrero, A. Almeida, G. Rangel-pineros, R.D. Finn, T.D. Lawley,

Massive expansion of human gut bacteriophage diversity ll ll Massive expansion of

human gut bacteriophage diversity, Cell. 184 (2021) 1098-1109.e9.

https://doi.org/10.1016/j.cell.2021.01.029.

[53] S.J. Labrie, J.E. Samson, S. Moineau, Bacteriophage resistance mechanisms, Nat. Rev.

Microbiol. 8 (2010) 317–327. https://doi.org/10.1038/nrmicro2315.

[54] A. V Letarov, History of Early Bacteriophage Research and Emergence of Key

Concepts in Virology, Biochem. 85 (2020) 1093–1112.

https://doi.org/10.1134/S0006297920090096.

[55]   S. Hesse, S. Adhya, Phage therapy in the twenty-first century: Facing the decline of the antibiotic era; is it finally time for the age of the phage?, Annu. Rev. Microbiol. 73 (2019) 155–174. https://doi.org/10.1146/annurev-micro-090817-062535.

[56]   H.W. Smith, M.B. Huggins, Successful Treatment of Experimental Escherichia coli Infections in Mice Using Phage: its General Superiority over Antibiotics, J. Gen. Microbiol. 128 (1982) 307–318. https://doi.org/10.1099/00221287-128-2-307.

[57]   R. Międzybrodzki, J. Borysowski, B. Weber-Dąbrowska, W. Fortuna, S. Letkiewicz, K. Szufnarowski, Z. Pawełczyk, P. Rogóż, M. Kłak, E. Wojtasik, A. Górski, Clinical Aspects of Phage Therapy, in: Adv. Virus Res., 2012: pp. 73–121. https://doi.org/10.1016/B978-0-12-394438-2.00003-7.

[58]   R.R. Bragg, C.E. Boucher, W.A. Van Der Westhuizen, J. Lee, E. Coetsee, C. Theron, L. Meyburgh, The Potential Use of Bacteriophage Therapy as a Treatment Option in a Post-antibiotic Era, Elsevier Inc., 2016. https://doi.org/10.1016/B978-0-12-803642-6.00015-0.

[59]   R.W. Hendrix, M.C.M. Smith, R.N. Burns, M.E. Ford, G.F. Hatfull, Evolutionary relationships among diverse bacteriophages and prophages: All the world's a phage, Proc. Natl. Acad. Sci. U. S. A. 96 (1999) 2192–2197. https://doi.org/10.1073/pnas.96.5.2192.

[60]   J.R. Meyer, A.A. Agrawal, R.T. Quick, D.T. Dobias, D. Schneider, R.E. Lenski, Parallel changes in host resistance to viral infection during 45,000 generations of relaxed selection, Evolution (N. Y). 64 (2010) 3024–3034. https://doi.org/10.1111/j.1558-5646.2010.01049.x.

[61]   X. Zhang, L. Wang, E. Levänen, Superhydrophobic surfaces for the reduction of bacterial adhesion, RSC Adv. 3 (2013) 12003. https://doi.org/10.1039/c3ra40497h.

[62]   P. Praus, Z. Rybková, Antibacterial and antifungal activities of silver , copper and zinc

montmorillonites, Appl. Clay Sci. 53 (2011) 642–645.

https://doi.org/10.1016/j.clay.2011.05.016.

[63] B. Dmitriev, F. Toukach, S. Ehlers, Towards a comprehensive view of the bacterial cell wall, Trends Microbiol. 13 (2005) 569–574. https://doi.org/10.1016/j.tim.2005.10.001.

[64] X. Zhou, W.J. Liao, J.M. Liao, P. Liao, H. Lu, Ribosomal proteins: Functions beyond the ribosome, J. Mol. Cell Biol. 7 (2015) 92–104. https://doi.org/10.1093/jmcb/mjv014.

[65] L. Molina-García, F. Gasset-Rosa, M. Moreno-Del Álamo, M.E. Fernández-Tresguerres, S. Moreno-Díaz De La Espina, R. Lurz, R. Giraldo, Functional amyloids as inhibitors of plasmid DNA replication, Sci. Rep. 6 (2016) 1–8. https://doi.org/10.1038/srep25425.

[66] C. Smillie, M.P. Garcilla, M.V. Francia, E.P.C. Rocha, F. De Cruz, Mobility of Plasmids, Microbiol. Mol. Biol. Rev. 74 (2010) 434–452. https://doi.org/10.1128/MMBR.00020-10.

[67] T.J. Silhavy, D. Kahne, S. Walker, The Bacterial Cell Envelope, Cold Spring Harb. Perspect. Biol. 2 (2010) a000414–a000414. https://doi.org/10.1101/cshperspect.a000414.

[68] J. Van Heijenoort, Formation of the glycan chains in the synthesis of bacterial peptidoglycan, Glycobiology. 11 (2001) 25–36. https://doi.org/10.1093/glycob/11.3.25r.

[69] F.C. Neuhaus, J. Baddiley, A Continuum of Anionic Charge : Structures and Functions of D -Alanyl-Teichoic Acids in Gram-Positive Bacteria, Microbiol. Mol. Biol. Rev. 67 (2003) 686–723. https://doi.org/10.1128/MMBR.67.4.686.

[70] S.L. Bardy, S.Y.M. Ng, K.F. Jarrell, Prokaryotic motility structures, Microbiology. 149 (2003) 295–304. https://doi.org/10.1099/mic.0.25948-0.

[71] I. Connell, W. Agace, P. Klemm, M. Schembri, S. Mărild, C. Svanborg, Type 1

fimbrial expression enhances Escherichia coli virulence for the urinary tract., Proc. Natl. Acad. Sci. 93 (1996) 9827–9832. https://doi.org/10.1073/pnas.93.18.9827.

[72] M. Jamal, W. Ahmad, S. Andleeb, F. Jalil, M. Imran, M. Asif, T. Hussain, M. Ali, M. Rafiq, M. Atif, Bacterial biofilm and associated infections, J. Chinese Med. Assoc. 81 (2018) 7–11. https://doi.org/10.1016/j.jcma.2017.07.012.

[73] C.H. Tan, K.W.K. Lee, M. Burmølle, S. Kjelleberg, S.A. Rice, All together now: experimental multispecies biofilm model systems, Environ. Microbiol. 19 (2017) 42–53. https://doi.org/10.1111/1462-2920.13594.

[74] M. Otto, Staphylococcal Infections: Mechanisms of Biofilm Maturation and Detachment as Critical Determinants of Pathogenicity, Annu. Rev. Med. 64 (2013) 175–188. https://doi.org/10.1146/annurev-med-042711-140023.

[75] M.J. Ashby, J.E. Neale, S.J. Knott, I.A. Critchley, Effect of antibiotics on non-growing planktonic cells and biofilms of escherichia coli, J. Antimicrob. Chemother. 33 (1994) 443–452. https://doi.org/10.1093/jac/33.3.443.

[76] H. Ceri, M.E. Olson, C. Stremick, R.R. Read, D. Morck, A. Buret, The Calgary Biofilm Device: New technology for rapid determination of antibiotic susceptibilities of bacterial biofilms, J. Clin. Microbiol. 37 (1999) 1771–1776. https://doi.org/10.1128/jcm.37.6.1771-1776.1999.

[77] I. Keren, D. Shah, A. Spoering, N. Kaldalu, K. Lewis, Specialized persister cells and the mechanism of multidrug tolerance in Escherichia coli, J. Bacteriol. 186 (2004) 8172–8180. https://doi.org/10.1128/JB.186.24.8172-8180.2004.

[78] R.M. Donlan, J.W. Costerton, Biofilms: Survival Mechanisms of Clinically Relevant Microorganisms, Clin. Microbiol. Rev. 15 (2002) 167–193. https://doi.org/10.1128/CMR.15.2.167-193.2002.

[79] N.P. Boks, H.J. Busscher, H.C. van der Mei, W. Norde, Bond-Strengthening in

Staphylococcal Adhesion to Hydrophilic and Hydrophobic Surfaces Using Atomic Force Microscopy, Langmuir. 24 (2008) 12990–12994. https://doi.org/10.1021/la801824c.

[80] N.P. Boks, H.J. Kaper, W. Norde, H.J. Busscher, H.C. van der Mei, Residence time dependent desorption of Staphylococcus epidermidis from hydrophobic and hydrophilic substrata, Colloids Surfaces B Biointerfaces. 67 (2008) 276–278. https://doi.org/10.1016/j.colsurfb.2008.08.021.

[81] L.D. Renner, D.B. Weibel, Physicochemical regulation of biofilm formation, MRS Bull. 36 (2011) 347–355. https://doi.org/10.1557/mrs.2011.65.

[82] I. Banerjee, R.C. Pangule, R.S. Kane, Antifouling Coatings: Recent Developments in the Design of Surfaces That Prevent Fouling by Proteins, Bacteria, and Marine Organisms, Adv. Mater. 23 (2011) 690–718. https://doi.org/10.1002/adma.201001215.

[83] S. Wu, S. Altenried, A. Zogg, F. Zuber, K. Maniura-Weber, Q. Ren, Role of the Surface Nanoscale Roughness of Stainless Steel on Bacterial Adhesion and Microcolony Formation, ACS Omega. 3 (2018) 6456–6464. https://doi.org/10.1021/acsomega.8b00769.

[84] R. Van Houdt, C.W. Michiels, Role of bacterial cell surface structures in Escherichia coli biofilm formation, Res. Microbiol. 156 (2005) 626–633. https://doi.org/10.1016/j.resmic.2005.02.005.

[85] K.J. Spears, A.J. Roe, D.L. Gally, A comparison of enteropathogenic and enterohaemorrhagic Escherichia coli pathogenesis, FEMS Microbiol. Lett. 255 (2006) 187–202. https://doi.org/10.1111/j.1574-6968.2006.00119.x.

[86] Y. Chao, T. Zhang, Probing Roles of Lipopolysaccharide, Type 1 Fimbria, and Colanic Acid in the Attachment of Escherichia coli Strains on Inert Surfaces, Langmuir. 27 (2011) 11545–11553. https://doi.org/10.1021/la202534p.

[87] K.C. MARSHALL, R. STOUT, R. MITCHELL, Mechanism of the Initial Events in the Sorption of Marine Bacteria to Surfaces, J. Gen. Microbiol. 68 (1971) 337–348. https://doi.org/10.1099/00221287-68-3-337.

[88] H.H. Tuson, D.B. Weibel, Bacteria–surface interactions, Soft Matter. 9 (2013) 4368. https://doi.org/10.1039/c3sm27705d.

[89] C.E. Santo, D. Quaranta, G. Grass, Antimicrobial metallic copper surfaces kill Staphylococcus haemolyticus via membrane damage, Microbiologyopen. 1 (2012) 46–52. https://doi.org/10.1002/mbo3.2.

[90] G. Grass, C. Rensing, M. Solioz, Metallic Copper as an Antimicrobial Surface, Appl. Environ. Microbiol. 77 (2011) 1541–1547. https://doi.org/10.1128/AEM.02766-10.

[91] V. Champagne, K. Sundberg, D. Helfritch, Kinetically Deposited Copper Antimicrobial Surfaces, Coatings. 9 (2019) 257. https://doi.org/10.3390/coatings9040257.

[92] L. Naiming, G. Junwen, H. Ruiqiang, Z. Jiaojuan, T. Bin, Double glow plasma surface alloying antibacterial silver coating on pure titanium, Surf. Rev. Lett. 21 (2014) 1450032. https://doi.org/10.1142/S0218625X14500322.

[93] V.M. Villapún, C.C. Lukose, M. Birkett, L.G. Dover, S. González, Tuning the antimicrobial behaviour of Cu85Zr15 thin films in "wet" and "dry" conditions through structural modifications, Surf. Coatings Technol. 350 (2018) 334–345. https://doi.org/10.1016/j.surfcoat.2018.06.094.

[94] M. Souli, A. Antoniadou, I. Katsarolis, I. Mavrou, E. Paramythiotou, E. Papadomichelakis, M. Drogari-Apiranthitou, T. Panagea, H. Giamarellou, G. Petrikkos, A. Armaganidis, Reduction of Environmental Contamination With Multidrug-Resistant Bacteria by Copper-Alloy Coating of Surfaces in a Highly Endemic Setting, Infect. Control Hosp. Epidemiol. 38 (2017) 765–771. https://doi.org/10.1017/ice.2017.52.

[95]   Y. Sun, V. Tran, D. Zhang, W. Bin Wang, S. Yang, Technology and Antimicrobial

        Properties of Cu/TiB₂ Composite Coating on 304 Steel Surface Prepared by Laser

        Cladding, Mater. Sci. Forum. 944 (2019) 473–479.

        https://doi.org/10.4028/www.scientific.net/MSF.944.473.

[96]   A.M. Kumar, A. Khan, R. Suleiman, M. Qamar, S. Saravanan, H. Dafalla, Bifunctional

        CuO/TiO2 nanocomposite as nanofiller for improved corrosion resistance and

        antibacterial protection, Prog. Org. Coatings. 114 (2018) 9–18.

        https://doi.org/10.1016/j.porgcoat.2017.09.013.

[97]   N. Krishnarao, R. Gupta, P.C. Ramamurthy, G. Madras, Influence of copper oxide

        grown on various conducting substrates towards improved performance for

        photoelectrocatalytic bacterial inactivation, Mol. Catal. 451 (2018) 161–169.

        https://doi.org/10.1016/j.mcat.2017.12.030.

[98]   G.A. Norambuena, R. Patel, M. Karau, C.C. Wyles, P.J. Jannetto, K.E. Bennet, A.D.

        Hanssen, R.J. Sierra, Antibacterial and Biocompatible Titanium-Copper Oxide Coating

        May Be a Potential Strategy to Reduce Periprosthetic Infection: An In Vitro Study,

        Clin. Orthop. Relat. Res. 475 (2017) 722–732. https://doi.org/10.1007/s11999-016-

        4713-7.

[99]   A. Mahmoodi, S. Solaymani, M. Amini, N.B. Nezafat, M. Ghoranneviss, Structural,

        Morphological and Antibacterial Characterization of CuO Nanowires, Silicon. 10

        (2018) 1427–1431. https://doi.org/10.1007/s12633-017-9621-2.

[100]   M.M.M.M. Mirhosseini, Z. Nazari, A. Kazempour, Antibacterial and photocatalytic

        activity of CuO nanostructure films with different morphology, J. Mater. Sci. Mater.

        Electron. 27 (2016) 8131–8137. https://doi.org/10.1007/s10854-016-4815-8.

[101]   R. Hong, T.Y. Kang, C.A. Michels, N. Gadura, Membrane Lipid Peroxidation in

        Copper Alloy-Mediated Contact Killing of Escherichia coli, Appl. Environ. Microbiol.

78 (2012) 1776–1784. https://doi.org/10.1128/AEM.07068-11.

[102] C.E. Santo, E.W. Lam, C.G. Elowsky, D. Quaranta, D.W. Domaille, C.J. Chang, G. Grass, Bacterial Killing by Dry Metallic Copper Surfaces, Appl. Environ. Microbiol. 77 (2011) 794–802. https://doi.org/10.1128/AEM.01599-10.

[103] J.R. Morones, J.L. Elechiguerra, A. Camacho, K. Holt, J.B. Kouri, J.T. Ramírez, M.J. Yacaman, The bactericidal effect of silver nanoparticles, Nanotechnology. 16 (2005) 2346–2353. https://doi.org/10.1088/0957-4484/16/10/059.

[104] A.N. Pham, G. Xing, C.J. Miller, T.D. Waite, Fenton-like copper redox chemistry revisited : Hydrogen peroxide and superoxide mediation of copper-catalyzed oxidant production, J. Catal. 301 (2013) 54–64. https://doi.org/10.1016/j.jcat.2013.01.025.

[105] C. Yang, L. Jiang, H. Zhang, L.A. Shimoda, R.J. DeBerardinis, G.L. Semenza, Analysis of Hypoxia-Induced Metabolic Reprogramming, in: Concept. Backgr. Bioenerg. Asp. Oncometabolism, 1st ed., Elsevier Inc., 2014: pp. 425–455. https://doi.org/10.1016/B978-0-12-416618-9.00022-4.

[106] P.D. Ray, B. Huang, Y. Tsuji, Reactive oxygen species (ROS) homeostasis and redox regulation in cellular signaling, Cell. Signal. 24 (2012) 981–990. https://doi.org/10.1016/j.cellsig.2012.01.008.

[107] B.M. Prabhu, S.F. Ali, R.C. Murdock, S.M. Hussain, M. Srivatsan, Copper nanoparticles exert size and concentration dependent toxicity on somatosensory neurons of rat, Nanotoxicology. 4 (2010) 150–160. https://doi.org/10.3109/17435390903337693.

[108] J.-C. Kim, I. Lee, J. Ko, S. Park, J.-O. Lim, I.-S. Shin, C. Moon, S.-H. Kim, J.-D. Her, Comparative toxicity and biodistribution of copper nanoparticles and cupric ions in rats, Int. J. Nanomedicine. 11 (2016) 2883. https://doi.org/10.2147/IJN.S106346.

[109] I. Salah, I.P. Parkin, E. Allan, Copper as an antimicrobial agent: recent advances, RSC

Adv. 11 (2021) 18179–18186. https://doi.org/10.1039/D1RA02149D.

[110] N.R. Sudarshan, D.G. Hoover, D. Knorr, Antibacterial action of chitosan, Food Biotechnol. 6 (1992) 257–272. https://doi.org/10.1080/08905439209549838.

[111] F. Costa, I.F. Carvalho, R.C. Montelaro, P. Gomes, M.C.L. Martins, Covalent immobilization of antimicrobial peptides (AMPs) onto biomaterial surfaces, Acta Biomater. 7 (2011) 1431–1440. https://doi.org/10.1016/j.actbio.2010.11.005.

[112] E.P. Ivanova, J. Hasan, H.K. Webb, V.K. Truong, G.S. Watson, J.A. Watson, V.A. Baulin, S. Pogodin, J.Y. Wang, M.J. Tobin, C. Löbbe, R.J. Crawford, Natural Bactericidal Surfaces: Mechanical Rupture of Pseudomonas aeruginosa Cells by Cicada Wings, Small. 8 (2012) 2489–2494. https://doi.org/10.1002/smll.201200528.

[113] T. Shimada, T. Yasui, A. Yonese, T. Yanagida, N. Kaji, M. Kanai, K. Nagashima, T. Kawai, Y. Baba, Mechanical Rupture-Based Antibacterial and Cell-Compatible ZnO/SiO2 Nanowire Structures Formed by Bottom-Up Approaches, Micromachines. 11 (2020) 610. https://doi.org/10.3390/mi11060610.

[114] J.I. Langford, A.J.C. Wilson, Scherrer after sixty years: A survey and some new results in the determination of crystallite size, J. Appl. Crystallogr. 11 (1978) 102–113. https://doi.org/10.1107/s0021889878012844.

[115] E. Robine, L. Boulangé-Petermann, D. Derangère, Assessing bactericidal properties of materials: the case of metallic surfaces in contact with air, J. Microbiol. Methods. 49 (2002) 225–234. https://doi.org/10.1016/S0167-7012(01)00371-2.

[116] N. Ciacotich, R. Ud, J.J. Sloth, P. Møller, L. Gram, An electroplated copper – silver alloy as antibacterial coating on stainless steel, Surf. Coat. Technol. 345 (2018) 96–104. https://doi.org/10.1016/j.surfcoat.2018.04.007.

[117] G. Wu, R. Liang, M. Ge, G. Sun, Y. Zhang, G. Xing, Surface Passivation Using 2D Perovskites toward Efficient and Stable Perovskite Solar Cells, Adv. Mater. 34 (2022).

https://doi.org/10.1002/adma.202105635.

[118] Y.L. Deng, J.W. Lee, B.S. Lou, J.G. Duh, J.P. Chu, J.S.C. Jang, The fabrication and property evaluation of Zr-Ti-B-Si thin film metallic glass materials, Surf. Coatings Technol. 259 (2014) 115–122. https://doi.org/10.1016/j.surfcoat.2014.03.026.

[119] H. Jia, F. Liu, Z. An, W. Li, G. Wang, J.P. Chu, J.S.C. Jang, Y. Gao, P.K. Liaw, Thin-film metallic glasses for substrate fatigue-property improvements, Thin Solid Films. 561 (2014) 2–27. https://doi.org/10.1016/j.tsf.2013.12.024.

[120] F.X. Liu, F.Q. Yang, Y.F. Gao, W.H. Jiang, Y.F. Guan, P.D. Rack, O. Sergic, P.K. Liaw, Micro-scratch study of a magnetron-sputtered Zr-based metallic-glass film, Surf. Coatings Technol. 203 (2009) 3480–3484.

https://doi.org/10.1016/j.surfcoat.2009.05.017.

[121] M. Rahm, R. Hoffmann, N.W. Ashcroft, Atomic and Ionic Radii of Elements 1–96, Chem. - A Eur. J. 22 (2016) 14625–14632. https://doi.org/10.1002/chem.201602949.

[122] S. Guha, J.D. Cohen, E. Schiff, P. Stradins, P.C. Taylor, J. Yang, Industry – academia partnership helps drive commercialization of new thin- film silicon technology, Photovolt. Int. 13 (2011) 134–140.

[123] W. Ravisy, Croissance et propriétés photocatalytiques de couches minces de TiO2 et W-TiO2 déposées par PECVD sur polymère, Thesis. (2021).

[124] L.R. Shaginyan, N. V. Britun, J.G. Han, V.R. Shaginyan, Anomalously high surface temperature induced by condensation of atoms, JETP Lett. 83 (2006) 113–117. https://doi.org/10.1134/S0021364006030076.

[125] A. Michels, S.R. De Groot, The influence of pressure on the boiling points of metals, Physica. 16 (1910) 249–252. https://doi.org/10.1016/0031-8914(50)90022-X.

[126] A.B. Hamouda, R. Sathiyanarayanan, A. Pimpinelli, T.L. Einstein, Role of codeposited impurities during growth. I. Explaining distinctive experimental morphology on Cu(0 0

1), Phys. Rev. B - Condens. Matter Mater. Phys. 83 (2011) 1–8.
https://doi.org/10.1103/PhysRevB.83.035423.

[127] L. Li, N. Mendis, H. Trigui, J.D. Oliver, S.P. Faucher, The importance of the viable but
non-culturable state in human bacterial pathogens, Front. Microbiol. 5 (2014) 1–1.
https://doi.org/10.3389/fmicb.2014.00258.

[128] M. Alam, M. Sultana, G. Balakrish Nair, A.K. Siddique, N.A. Hasan, R. Bradley Sack,
D.A. Sack, K.U. Ahmed, A. Sadique, H. Watanabe, C.J. Grim, A. Huq, R.R. Colwell,
Viable but nonculturable Vibrio cholerae O1 in biofilms in the aquatic environment
and their role in cholera transmission, Proc. Natl. Acad. Sci. U. S. A. 104 (2007)
17801–17806. https://doi.org/10.1073/pnas.0705599104.

[129] D.B. Kearns, R. Losick, Swarming motility in undomesticated Bacillus subtilis, Mol.
Microbiol. 49 (2003) 581–590. https://doi.org/10.1046/j.1365-2958.2003.03584.x.

[130] T. Nishihara, E. Freese, Motility of Bacillus subtilis during growth and sporulation., J.
Bacteriol. 123 (1975) 366–371. https://doi.org/10.1128/jb.123.1.366-371.1975.

[131] S. Mukherjee, D.B. Kearns, The structure and regulation of flagella in bacillus subtilis,
Annu. Rev. Genet. 48 (2014) 319–340. https://doi.org/10.1146/annurev-genet-120213-
092406.

[132] H.M. Stich, A field guide to bacteria swarming motility, Bee World. 3 (1921) 76–77.
https://doi.org/10.1080/0005772x.1921.11095141.

[133] S. Mathews, M. Hans, F. Mücklich, M. Solioz, Contact killing of bacteria on copper is
suppressed if bacterial-metal contact is prevented and is induced on iron by copper
ions, Appl. Environ. Microbiol. 79 (2013) 2605–2611.
https://doi.org/10.1128/AEM.03608-12.

[134] J. Luo, C. Hein, J.-F. Pierson, F. Mücklich, Early-stage corrosion, ion release, and the
antibacterial effect of copper and cuprous oxide in physiological buffers: Phosphate-

buffered saline vs Na-4-(2-hydroxyethyl)-1-piperazineethanesulfonic acid, Biointerphases. 14 (2019). https://doi.org/10.1063/1.5123039.

[135] B. Li, B.E. Logan, Bacterial adhesion to glass and metal-oxide surfaces, Colloids Surfaces B Biointerfaces. 36 (2004) 81–90. https://doi.org/10.1016/j.colsurfb.2004.05.006.

[136] K. San, J. Long, C.A. Michels, N. Gadura, Antimicrobial copper alloy surfaces are effective against vegetative but not sporulated cells of gram-positive Bacillus subtilis, Microbiologyopen. 4 (2015) 753–763. https://doi.org/10.1002/mbo3.276.

[137] Q. Liebgott, A. Borroto, S. Bruyère, F. Mücklich, D. Horwat, Deposition rate controls nucleation and growth during amorphous/nanocrystalline competition in sputtered Zr-Cr thin films, J. Alloys Compd. 936 (2023) 168258. https://doi.org/10.1016/j.jallcom.2022.168258.

[138] Y. Pauleau, Generation and evolution of residual stresses in physical vapour-deposited thin films, Vacuum. 61 (2001) 175–181. https://doi.org/10.1016/S0042-207X(00)00475-9.

[139] M. Pletea, R. Koch, H. Wendrock, R. Kaltofen, O.G. Schmidt, In situ stress evolution during and after sputter deposition of Al thin films, J. Phys. Condens. Matter. 21 (2009) 225008. https://doi.org/10.1088/0953-8984/21/22/225008.

[140] G. Abadias, E. Chason, J. Keckes, M. Sebastiani, G.B. Thompson, E. Barthel, G.L. Doll, C.E. Murray, C.H. Stoessel, L. Martinu, Review Article: Stress in thin films and coatings: Current status, challenges, and prospects, J. Vac. Sci. Technol. A Vacuum, Surfaces, Film. 36 (2018). https://doi.org/10.1116/1.5011790.

[141] L.E. Koutsokeras, G. Abadias, Intrinsic stress in ZrN thin films: Evaluation of grain boundary contribution from in situ wafer curvature and ex situ x-ray diffraction techniques, J. Appl. Phys. 111 (2012) 093509. https://doi.org/10.1063/1.4710530.

[142] J. Štrof, J. Pavlů, U.D. Wdowik, J. Buršík, M. Šob, J. Vřešťál, Laves phases in the V-Zr system below room temperature: Stability analysis using ab initio results and phase diagram, Calphad Comput. Coupling Phase Diagrams Thermochem. 44 (2014) 62–69. https://doi.org/10.1016/j.calphad.2013.08.003.

[143] E. Vasco, C. Polop, Intrinsic Compressive Stress in Polycrystalline Films is Localized at Edges of the Grain Boundaries, Phys. Rev. Lett. 119 (2017) 1–5. https://doi.org/10.1103/PhysRevLett.119.256102.

[144] E. Vasco, E.G. Michel, C. Polop, Disclosing the origin of the postcoalescence compressive stress in polycrystalline films by nanoscale stress mapping, Phys. Rev. B. 98 (2018) 1–12. https://doi.org/10.1103/PhysRevB.98.195428.

[145] K.V. Reddy, M. Meraj, S. Pal, Molecular dynamics simulation based investigation of strain induced crystallization of nickel metallic glass, Mater. Chem. Phys. 237 (2019) 121831. https://doi.org/10.1016/j.matchemphys.2019.121831.

[146] Y. Mao, J. Li, Y.C. Lo, X. Qian, E. Ma, Stress-driven crystallization via shear-diffusion transformations in a metallic glass at very low temperatures, Phys. Rev. B - Condens. Matter Mater. Phys. 91 (2015) 1–8. https://doi.org/10.1103/PhysRevB.91.214103.

[147] B.J. Lee, C.S. Lee, J.C. Lee, Stress induced crystallization of amorphous materials and mechanical properties of nanocrystalline materials: A molecular dynamics simulation study, Acta Mater. 51 (2003) 6233–6240. https://doi.org/10.1016/S1359-6454(03)00446-4.

[148] G. Eising, A. Pauza, B.J. Kooi, Stress-Induced Crystallization of Ge-Doped Sb Phase-Change Thin Films, Cryst. Growth Des. 13 (2013) 220–225. https://doi.org/10.1021/cg3013848.

[149] B. Krause, G. Abadias, A. Michel, P. Wochner, S. Ibrahimkutty, T. Baumbach, Direct

Observation of the Thickness-Induced Crystallization and Stress Build-Up during Sputter-Deposition of Nanoscale Silicide Films, ACS Appl. Mater. Interfaces. 8 (2016) 34888–34895. https://doi.org/10.1021/acsami.6b12413.